LLNL-JRNL-2004640

Lawrence Livermore National Laboratory

Solution and Active Site Speciation Drive Selectivity for Electrocatalytic Reactive Carbon Capture in Diethanolamine over Ni-N-C Catalysts

D Ross, A Alexandrova, C Hahn, Y Han, H Jeong, J Ynzunza, R Lavroff, A Banerjee, A Prajapati, C Morales-Guio, J Velazquez

January 2026

Journal of the American Chemical Society

Disclaimer

This document was prepared as an account of work sponsored by an agency of the United States government. Neither the United States government nor Lawrence Livermore National Security, LLC, nor any of their employees makes any warranty, expressed or implied, or assumes any legal liability or responsibility for the accuracy, completeness, or usefulness of any information, apparatus, product, or process disclosed, or represents that its use would not infringe privately owned rights. Reference herein to any specific commercial product, process, or service by trade name, trademark, manufacturer, or otherwise does not necessarily constitute or imply its endorsement, recommendation, or favoring by the United States government or Lawrence Livermore National Security, LLC. The views and opinions of authors expressed herein do not necessarily state or reflect those of the United States government or Lawrence Livermore National Security, LLC, and shall not be used for advertising or product endorsement purposes.

This work performed under the auspices of the U.S. Department of Energy by Lawrence Livermore National Laboratory under Contract DE-AC52-07NA27344.

Solution and Active Site Speciation Drive Selectivity for Electrocatalytic Reactive Carbon Capture in Diethanolamine over Ni-N-C Catalysts

R. Dominic Ross,[1,2,‡] Yulan Han,[3,‡] Hui-Yun Jeong,[1,2] Jenna M. Ynzunza,[4] Robert H. Lavroff,[3] Avishek Banerjee,[5] Aditya Prajapati,[1,2] Carlos G. Morales-Guio,[5] Jesús M. Velázquez,[4] Anastassia N. Alexandrova,[3] Christopher Hahn[1,2*]*

[1]Materials Science Division, Lawrence Livermore National Laboratory, Livermore, CA 94550, USA

[2]Laboratory for Energy Applications for the Future (LEAF), Lawrence Livermore National Laboratory, Livermore, CA 94550, USA

[3]Department of Chemistry and Biochemistry, University of California, Los Angeles, Los Angeles, CA 90095, USA

[4]Department of Chemistry, University of California, Davis, Davis, CA 95616, USA

[5]Department of Chemical and Biomolecular Engineering, University of California, Los Angeles, Los Angeles, CA 90095, USA

[‡]These authors contributed equally.

[*]Corresponding author emails: alexandrova@g.ucla.edu, hahn31@llnl.gov

Abstract

Direct conversion of captured forms of carbon, or reactive carbon capture (RCC), presents an opportunity to reduce the energy intensity and cost of direct CO_2 utilization from dilute sources. While amine-based sorbents effectively capture CO_2, their use for RCC presents numerous challenges with typical pure metal catalysts used for electrochemical CO_2 reduction (CO_2R). Here, using both theory and experiments, we find that Ni-N-C single atom catalysts are effective for RCC conversion to CO using a diethanolamine sorbent, in contrast to pure metal catalysts. Computational analysis reveals that RCC can proceed directly through direct reduction of the sorbent-CO_2 adduct or indirectly by C-N bond breaking facilitating CO_2 adsorption and subsequent reduction. We find that the latter mechanism is most prevalent at low overpotentials where we experimentally observe RCC selectivity. We also find experimentally that the rate of CO production for RCC with Ni-N-C catalysts can exceed pure bicarbonate solutions at intermediate sorbent concentration (0.1-0.5 M DEA) under dilute (10-25%) streams of CO_2 at low overpotentials. The coordination environment of Ni sites and the solution speciation influence their RCC activity, with changes in protonation to coordinating N/C atoms resulting in changing the RCC mechanism and consequent activity. *In situ* X-ray absorption spectroscopy and computational analysis reveal restructuring under RCC conditions due to hydrogen co-adsorption with DEA that limits the stability of Ni-N-C catalysts. This work highlights the importance of carefully controlling the catalyst and solution environment to achieve active and stable RCC electrocatalysis.

Introduction

Processes powered by renewable electricity to capture and convert carbon dioxide (CO_2) from the atmosphere are urgently needed to mitigate the impacts of climate change. Benchmark sorbents for carbon capture are typically amines such as monoethanolamine (MEA) or diethanolamine (DEA), on account of their high affinity for CO_2.[1] The capture of CO_2 by amines generates CO_2-amine adducts (i.e. carbamates). For each negatively charged carbamate, an equivalent amount of the protonated amine is generated (**Scheme 1**). The highly thermodynamically stable carbamate also results in an energy-intensive regeneration step needed to achieve CO_2-lean amine and pure CO_2 from the capture solution.[2,3] Reactive carbon capture (RCC) integrates capture and conversion by directly reacting CO_2 in the capture media, subverting the need for successive capture, sorbent regeneration, and CO_2 conversion.[4–6] This process presents the opportunity to reduce the cost and energy intensity of achieving carbon-neutral industrial processes[6–8] by continuously valorizing CO_2 from industrial point sources (i.e. flue gas) such as cement production[9] and power generation.[10] The concentrations of CO_2 present in these streams are typically too dilute for efficient electrocatalytic conversion directly,[11] and often contain contaminants that poison typical catalysts for direct CO_2 electroreduction.[12]

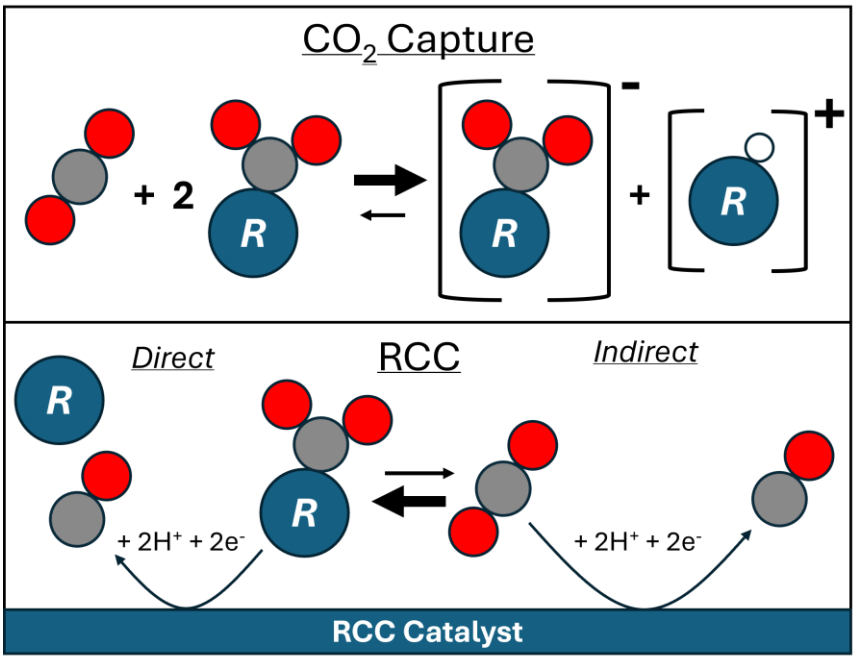

Scheme 1. CO_2 capture process with amines (top, *R* = primary or secondary amine) and reactive carbon capture (RCC, bottom). RCC can proceed through the direct mechanism (left) where the CO_2-amine adduct (carbamate) binds to the catalyst surface and is reduced, or an indirect mechanism (right) where CO_2 adsorbates are produced which can subsequently be reduced. Gray = carbon, red = oxygen, white = hydrogen.

Pure metals that are typically exemplar electrochemical CO_2 reduction (CO_2R) catalysts exhibit negligible selectivity for RCC in amines, especially in the absence of an additional incoming CO_2 source.[13–19] The primary causes are the promotion of HER by protonated amines,[13,15,16] the capture of free CO_2 near the interface by lean amines,[16] the difficulty in directly reducing thermodynamically stable carbamates,[14] and the corrosion of metal surfaces.[15,20] To achieve effective RCC with amines, some strategies to suppress HER by changing the catalyst microenvironment have been explored, such as the use of cationic (ammonium-based) surfactants,[17] larger alkali metal cations,[18,21,22] non-aqueous solvents,[23,24]

molecular catalysts (in non-aqueous solvents),[25] and sterically hindered amines.[24,26,27] However, no single approach has achieved both high rates of reaction and high selectivity for carbon based products using amines as a sorbent.

Metal-nitrogen doped carbon (M-N-C) single atom catalysts (SACs) have been utilized widely in CO_2 reduction, achieving nearly >90% selectivity for CO at high current density.[28–31] This is largely due to effective suppression of HER by weakened H* adsorption on coordinated metal centers. Similarly, Ni-N-C SACs have been demonstrated to have some selectivity towards carbon-based products under RCC conditions.[27,32–34] More broadly, SACs also have different active site structures (i.e. NiN_xC_{4-x}) depending on the exact synthesis conditions.[35,36] The significant variability in active site ensembles complicates the analysis of these catalysts for RCC. While these catalysts are stable for CO_2R, their stability under RCC conditions remains largely unknown. There are some examples of achieving relatively high conversion rates over Ni-N-C catalysts with amine based sorbents, although higher rates of conversion to CO with moderate selectivity typically require the use of proton exchange membrane (PEM) with a CO_2 diffusion layer of a bipolar membrane (BPM) to liberate and directly react free CO_2 from the capture solution.[32,34] More recently, the use of diamines that can form zwitterionic carbamates at high CO_2 concentrations has been demonstrated as a route to direct reduction of amine-captured CO_2.[27] The direct reduction route of these amines was demonstrated by computation and the ability to obtain high rates of CO production in an anion exchange membrane (AEM) based electrolyzer. These works suggest promise for improving carbon utilization by using selective RCC systems, particularly where carbamates can be directly reduced, which warrants further exploration of the underlying active species under different operating conditions in order to ensure long term operation. Performance of amine-based RCC systems is highly variable

depending on the partial pressure of CO_2 in the capture solution.[19] RCC is often demonstrated under CO_2 saturated conditions, which evaluates resiliency to operating in amines, but overlooks evaluating the prevalence of the RCC pathway, in which carbamates can be adsorbed to the catalyst surface and subsequently converted to carbon-based products (**Scheme 1**), as opposed to reducing free CO_2 in the presence of amines. Understanding the surface intermediates formed from amine-based RCC on Ni-N-C catalysts in terms of both energetics (i.e. activity and selectivity) as well as their impact on structural evolution (i.e. stability) will be crucial to further development of these systems. Additionally, dynamic speciation of the electrolyte due to applied current/voltage and different CO_2 partial pressures will also impact these mechanistic pathways, demanding an in depth understanding of how the catalyst structure and performance change under different operating conditions.

In this study, we demonstrate that Ni-N-C catalysts can partially suppress HER in diethanolamine (DEA), producing orders of magnitude higher CO selectivity than observed over pure metal catalysts and enhancing the rate for direct conversion of dilute streams of CO_2. Using theory, we evaluate different RCC pathways, and find that they are heavily influenced by the initial defect structure of the Ni-N-C catalyst and the applied potential. Importantly, applied potential influences the protonation environment on coordinating carbons around Ni sites, influencing the viability of RCC and the stability of Ni sites. By varying the CO_2 and DEA concentrations during experimental testing and using vapor-liquid equilibrium (VLE) modeling, we find further evidence that while free CO_2 (i.e. CO_2 not chemisorbed to an amine when it is reduced) can contribute to CO production over Ni-N-C catalysts, there is a rate enhancement driven by RCC. This observation is congruent with theory suggesting RCC should be preferred to conventional CO_2R and HER across a broad potential range. Through theoretical simulations

and *in situ* experimental X-ray absorption spectroscopy measurements, we also find that evolving Ni site speciation during RCC plays a role in deactivation of the catalyst at highly negative potentials, providing previously unexplored insights into the role of catalyst dynamics during RCC in amines.

Results and Discussion

Evaluating Dependence of RCC Pathways on Ni-N-C Coordination

To model reaction pathways of RCC on Ni-N-C catalysts, we focused on four-coordinated Ni sites — representing the most stable configuration — and examined a series of NiN_xC_{4-x} environments (x = 0, 1, 2, 3, 4) (**Figures 1a, 1b** and **S1**), allowing for a systematic evaluation of how the local atomic environment influences catalytic behavior. To evaluate the relative importance of each of these sites, we used experimental Ni K-edge extended X-ray absorption fine structure (EXAFS) measurements to obtain an ensemble coordination number of a representative Ni-N-C catalyst (**Figure 1c, Table S1 and Table S2**). Probing the Ni K-edge EXAFS allows for obtaining an average number of nearest neighbors around Ni sites, with some sensitivity to the identity of the nearest neighbors based on different scattering. We found that the average coordination was $NiN_{3.3}C_{0.7}$, suggesting prevalent NiN_3C_1 and NiN_4 sites. Thus, we focus much of our detailed analysis on these two types of sites. Nonetheless, we still examined all possible sites theoretically, as minority sites can sometimes dominate catalytic activity. To consider the influence of proton transfer from amines to the catalyst, we assessed the thermodynamic stability of NiN_xC_{4-x} catalyst surfaces under varying hydrogen coverages at reducing potential (pH = pKa(DEA) = 8.9). Our analysis reveals that hydrogen preferentially adsorbs on adjacent carbon sites rather than nitrogen sites (**Figure 1d** and **S2**), with the NiN_4 configuration having preference towards an

unhydrogenated surface. As the potential becomes more negative, hydrogen coverage increases, and at sufficiently reducing conditions, the number of adsorbed hydrogen atoms approaches that of the surrounding C atoms.

To understand the likelihood of RCC proceeding on NiN_xC_{4-x} to begin with, we also evaluated its thermodynamic viability against typical CO_2R and HER. We broadly define RCC as any adsorption of the carbamate to the catalyst surface, regardless of whether reduction is completed while the carbamate C-N bond is intact. Near the electrode surface, where the HER rapidly consumes protons and creates a locally alkaline environment, CO_2 liberation becomes further suppressed since protonation - a prerequisite for decomposition - is disfavored. Nonetheless, when amine solutions are saturated with CO_2 there will be free CO_2 in equilibrium with DEA/carbamate and bicarbonate. While carbamates and bicarbonate nominally have similar expected thermodynamic direct reduction potentials,[13] there is a lack of evidence in the literature for direct bicarbonate reduction. Instead, researchers have leveraged pH swing release of CO_2 from bicarbonate for efficient conversion through interfacial acidification.[37,38] As the present studies are under neutral to alkaline conditions, we consider the thermodynamic competition between the following reactions and not direct bicarbonate reduction:

RCC: $Na^+(DEA\text{-}CO_2^-) + 3\ (DEA\text{-}H^+ + ClO_4^-) + 2\ e^- \rightarrow CO + H_2O + 4\ DEA + NaClO_4 + 2ClO_4^-$ (eq. 1)

CO_2R: $CO_2 + 2e^- + 2\ (DEA\text{-}H^+ + ClO_4^-) \rightarrow CO + H_2O + 2ClO_4^- + 2\ DEA$ (eq. 2)

HER: $2\ (DEA\text{-}H^+ + ClO_4^-) + 2e^- \rightarrow 2DEA + H_2 + 2\ ClO_4^-$ (eq. 3)

We found that the calculated equilibrium potentials (**Figure S3**) followed the order HER (-0.53 V) < RCC (-0.78 V) < CO_2R (-1.11 V). This trend demonstrates that RCC is thermodynamically preferred to CO_2R. In other words, proceeding through a mechanism of reducing CO_2 facilitated by carbamate adsorption is thermodynamically preferable. However, HER facilitated by preferential adsorption of $DEAH^+$ is competitive with RCC, consistent with past observations of low RCC selectivity. Going forward, we focused primarily on RCC and HER for theoretical consideration of the mechanistic pathways on the $NiN_{4-x}C_x$.

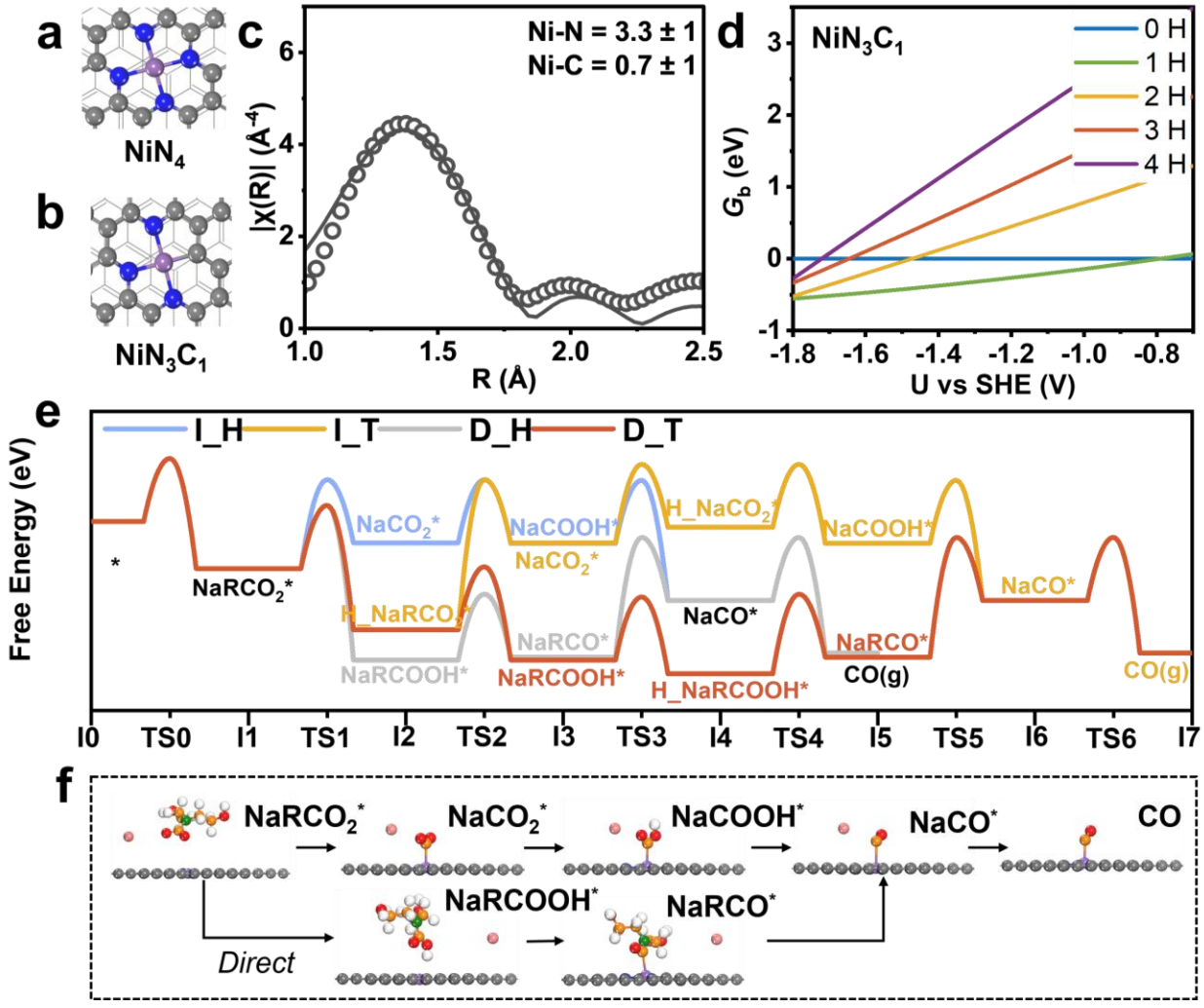

Figure 1. Optimized structures of a) NiN_4 and b) NiN_3C_1 obtained that are likely to make up the majority of Ni-N-C sites. Color code of atoms: Ni (purple), N (blue), C (gray), and H (white). c) Extended X-ray absorption fine structure (EXAFS) data (circles) and fitting (line) of as-synthesized Ni-N-C powder. d) Thermodynamic stability of NiN_3C_1 sites under varying hydrogen coverages. e) Reaction energy diagram on NiN_3C_1 at 0 H coverage and an applied potential of –1.2 V, illustrating four reaction pathways: I_H – Indirect CO_2 reduction with protons from the solvent (Heyrovsky-type); I_T – Indirect CO_2 reduction with a surface-adsorbed proton (Tafel-type); D_H – Direct CO_2 reduction with protons from the solvent (Heyrovsky-type); D_T – Direct CO_2 reduction with surface-adsorbed H (Tafel-type). In all cases, R denotes the DEA (diethanolamine) group in the captured intermediate $NaRCO_2$. Atom color code: Ni (purple), Na (pink), N of the catalyst (blue), N of DEA (green), C of the catalyst (gray), C of DEA (orange), and H (white). f) Corresponding structures for key intermediates along the RCC pathway with indirect pathway shown on top and the direct pathway shown on the bottom.

To understand the influence of the adsorbed hydrogen, we then investigated RCC reaction pathways on various Ni–N–C catalysts under different hydrogen coverages (**Figure 1e**) as a means of identifying the most likely mechanistic steps of RCC on Ni-N-C catalysts The RCC mechanism can be classified into two main categories based on the sequence of C–N bond cleavage. The first category involves early C–N bond breaking immediately following $NaRCO_2$ adsorption, transitioning from RCO_2 to CO_2, corresponding to *indirect CO_2 reduction*, where DEA serves as a shuttle of CO_2 to the electrode. Note that the electrolyte cation, Na^+, is included in the model, based on its electrostatic coordination to the negatively charged adduct; it assists the transport to the cathode. The second category involves later C–N bond breaking, occurring from RCO to CO corresponding to *direct RCC*, where CO_2 being reduced while on the adduct. These pathways are

illustrated in **Scheme 1**. We also considered the origin of hydrogen involved in the hydrogenation steps. In a Heyrovsky-type mechanism, protons are donated directly from the solvent ($DEAH^+$), whereas in a Tafel-type mechanism, hydrogen is pre-adsorbed on the catalyst surface prior to the reaction. These two hydrogenation mechanisms, combined with the two C–N cleavage sequences, result in a total of four possible reaction pathways (**Figure 1e and 1f**). This classification provides a framework for rationalizing how the bond-breaking sequence and the hydrogen source diversify the RCC mechanism. To estimate reaction barriers, we employ the *energy span model*,[39] where reactivity is approximated by the largest energy difference between a transition state and an intermediate along the pathway — a process referred to as the rate-determining process (RDP).[13] The calculated energy spans across different reaction pathways, catalysts, and hydrogen coverages are summarized in **Figure S2.**

By incorporating the Boltzmann distribution of hydrogen coverages and the corresponding energy span values, we determined the probability distribution of different reaction pathways for catalysts with each speciation (**Figures 2a**, **2b** and **S4**). Our analysis reveals that as the potential becomes more negative, surfaces with higher hydrogen coverages contribute more prominently to the overall reaction for active sites that have direct carbon coordination (**Figure 2b and S4)**. Furthermore, the dominant reaction pathway shifts from *I_H* to *D_H* (i.e. *indirect RCC* to *direct RCC* with protons coming from the $DEAH^+$), while *D_T* (*direct RCC* with a pre-adsorbed proton) also contributes to reaction at intermediate potentials.

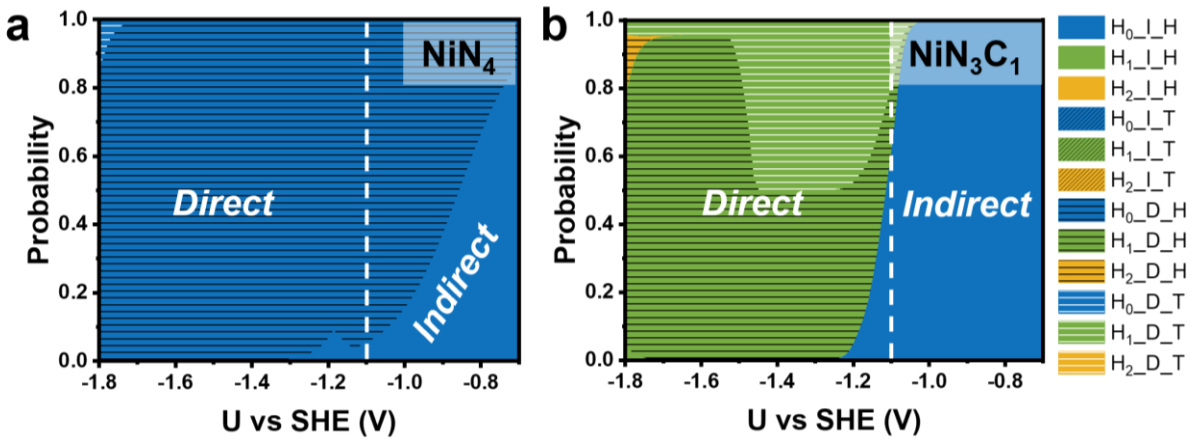

Figure 2. Probability distribution of different RCC pathways on a) NiN_4 and b) NiN_3C_1 with varying hydrogen coverages, highlighting their relative contributions to the reaction rate. H_n_I_H represents the I_H pathway on a surface with n adsorbed hydrogen atoms.

To rationalize the potential-dependent activity trends and locate the bottleneck of each reaction pathway, we further analyzed RDP for each pathway under different applied potentials (**Figure S5**). At lower overpotentials (-1.0 V), the I_H exhibits superior performance, with the rate-determining process primarily involving two key transitions: I1TS2 (RCO_2* → COOH*) and I1TS1 (RCO_2* → CO_2*). However, as the potential becomes more negative (-1.2 V), the energy span for I_H generally increases, shifting the rate-determining process predominantly to I1TS1. This shift occurs because the applied potential preferentially stabilizes RCO_2 rather than CO_2. Simultaneously, D_H becomes more favorable, with its RDP transitioning from I2TS3 (RCOOH* → CO*) and I3TS3 (RCO* → CO*) to I2TS2 (RCOOH* → RCO*), as the applied potential significantly enhances the binding energy of CO. Additionally, D_T demonstrates improved performance under more negative potentials, when it shares the same RDP as D_H. These findings provide a basis for tuning key steps to improve catalytic performance.

Next, we calculated the weighted energy spans for $NiNxC_{4-x}$ under different applied potentials (**Figure 3a**). A lower weighted energy span corresponds to higher catalytic activity. Our results indicate that the activity follows the trend: $NiN_1C_3 \approx NiN_2C_2 > NiN_3C_1$, while NiN_4 and NiC_4 exhibit poor activity. As the potential decreases, the overall RCC activity increases, though the change in NiN_1C_3 remains relatively minor.

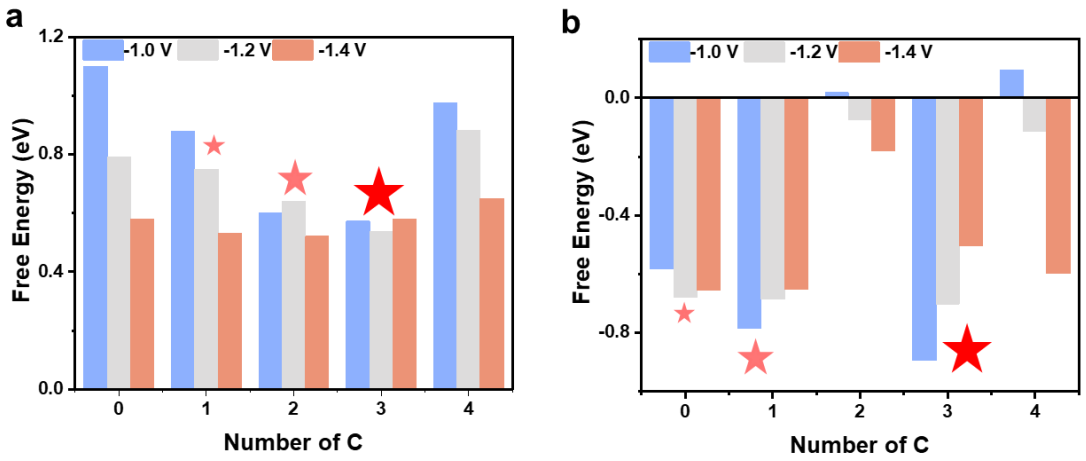

Figure 3. a) Calculated weighted energetic spans for RCC and b) the difference in weighted energetic spans between RCC and HER on NiN_xC_{4-x} under varying applied voltages. The red stars highlight key data points indicating significant trends in the variations in energetic span.

To assess the viability of RCC in competition with HER, we calculated the energy span of HER on NiN_xC_{4-x} catalysts under varying hydrogen coverages and applied potentials **(Figure S6)**, followed by evaluation of the corresponding weighted energy spans (**Figure S7**). The difference between the weighted energy spans of RCC and HER was then used as a descriptor to quantify selectivity (**Figure 3b**). A more negative value indicates higher RCC selectivity. Our analysis reveals that NiN_2C_2 and NiC_4 exhibit poor selectivity, while the trend among the other catalysts follows $NiN_1C_3 > NiN_3C_1 > NiN_4$. Notably, out of these three most selective sites, selectivity

decreases as the potential becomes more negative except for in the case of NiN_4. Considering that the Ni–N–C sites are likely to have a nitrogen coordination number close to 4,[40] we expect NiN_1C_3 to be a minority compared to NiN_3C_1, and yet could hypothetically dominate the RCC activity.

Experimental RCC Selectivity Dependence on Potential

To test our predictions about the behavior of Ni-N-C under RCC conditions, we first synthesized Ni-N-C according to a previously established procedure[28] with slight modifications, using a silica template to obtain a porous Ni-N-C catalyst (see Experimental Procedures for details). To evaluate the viability of RCC on Ni-SACs against previous examples of pure metals, we utilized a sealed rotating disk electrode (RDE) cell, as described elsewhere,[15,41] to benchmark against pure metal catalysts measured in the same configuration. Initially, to prove successful synthesis of a catalyst producing a high ratio of CO/H_2 from CO_2 electroreduction, we conducted a CO_2R benchmark on the Ni-N-C on glassy carbon in 1 M $NaHCO_3$ (**Figure 4a**). As expected, there is a high selectivity for CO compared to H_2, with Faradaic efficiency (FE) at -12 mA cm^{-2} exceeding 80%.

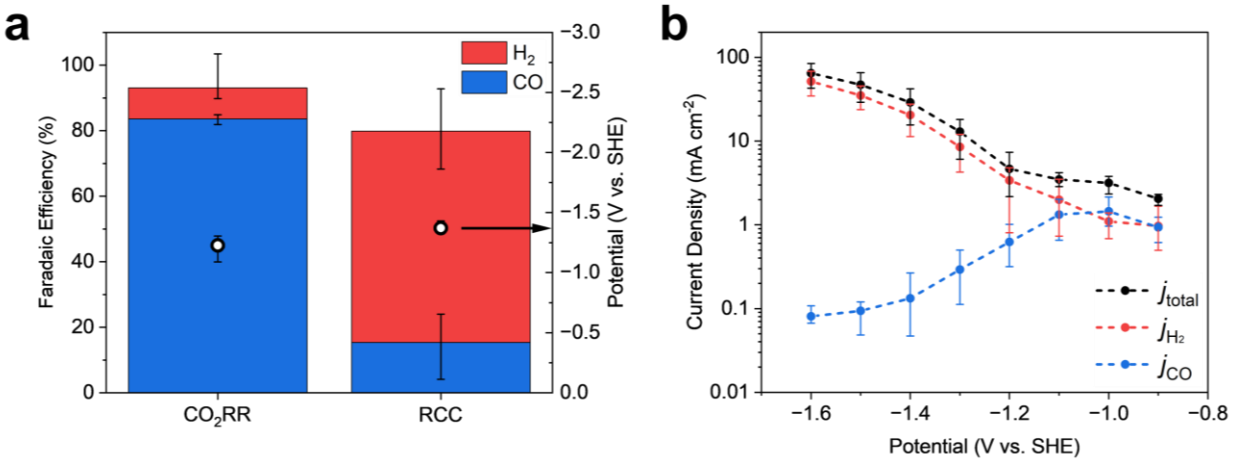

Figure 4. Kinetics of RCC with Ni-N-C catalyst measured in a sealed rotating disk electrode (RDE) cell under rotation at 800 rpm – error bars represent the minimum and maximum values over three parallel tests. a) Comparison of Faradaic efficiency (bars, left axis) and operating potential (dots, right axis) under constant current for conventional CO_2R (flowing CO_2 into 1 M $NaHCO_3$ solution) and RCC (flowing Ar into 0.5 M DEA/0.5 M $NaClO_4$ solution that was pre-purged with CO_2), and b) potential dependence of CO selectivity for RCC on Ni-N-C catalyst under RCC conditions (flowing Ar into 0.5 M DEA/0.5 M $NaClO_4$ solution that was pre-purged with CO_2).

For a general evaluation of whether there would be detectable CO from RCC, we then measured the same dropcasted RDE in a solution of 0.5 M DEA and 0.5 M $NaClO_4$ that was pre-saturated with CO_2. During the measurement, the solution was purged with Ar. We observed an average of 15% FE for CO under these conditions (**Figure 4a**). Each parallel test represents an average over three samplings in a one-hour test in which the CO FE would decrease over the course of the measurement to as low as 1%. However, the observation of CO under RCC conditions at -12 mA cm^{-2} was promising, as metal cylinders of Cu, Sn, Au, and Ag measured at an identical current density in the same cell showed <0.02% FE.[15]

After the initial demonstration of RCC on the Ni-N-C catalyst, we sought to understand how the performance varied across different applied potentials to correlate with our analysis of the mechanisms and energetics. We measured the activity and selectivity dependence of the Ni-N-C catalyst on the RDE while stepping from -0.9 V vs. SHE to -1.6 V vs. SHE (**Figure 4b and S8**). Low overpotentials (-0.9 V, -1 V, -1.1 V vs. SHE) had moderate CO selectivity, with nearly 1:1 CO:H_2. At -1.2 V vs. SHE there is a noticeable drop in CO selectivity and increase in H_2 selectivity (**Figure 4b and S8**). As the potential becomes more and more negative past -1.2 V vs. SHE, the

total current density continuously increases and HER becomes dominant. At a potential of -1.6 V vs. SHE, the CO FE decreases to <1%. The observation of peak selectivity between -0.9 and -1.1 V vs. SHE is consistent with a similar measurement of 1 M DEA, which had peak selectivity for CO between approximately -0.96 V and -1.16 V vs. SHE (assuming pH = 8 for 1 M DEA).[32] However, a slightly lower overall FE_{CO} was observed, warranting further investigation into the experimental factors that contribute to differences in RCC selectivity for a given catalyst.

The shift in selectivity correlates with the increasing difference in the weighted energy spans of RCC and HER on NiN_3C_1 sites (**Figure 3b**), indicating a growing preference for HER. This also implies a large contribution of NiN_3C_1 sites to RCC activity, as opposed to NiN_4 sites. Prevalent NiN_3C_1 would also explain the higher RCC activity at low overpotentials, since NiN_4 is predicted to be less active at low overpotentials (**Figure 3a**). Thus, we would expect a significant onset of the direct mechanism being the primary mechanism on NiN_3C_1 around -1.1 V vs. SHE, near the peak of the observed CO selectivity. Instead, we observe very little RCC at potentials more negative than -1.1 V vs. SHE. We assume that there are mass transport limitations that promote HER in favor of RCC, although this does not rule out the possibility of the small amount of RCC being through the direct mechanism. The deviation from the results of our energy span calculations at larger overpotentials led us to further explore the speciation of the microenvironment that could present these unforeseen limitations at the electrode surface.

We then conducted vapor-liquid equilibrium (VLE) modeling (**Figure S9**) to better understand the nature of the evolving bulk solution speciation that results in dynamic RCC performance. The VLE models indicate that as CO_2 loading of the amine decreases, the availability of free CO_2 rapidly decreases away from the saturation point. Carbamates increase as CO_2 decreases at lower loadings, but eventually peak and decrease in favor of DEA (without bound

CO_2) at very low CO_2 loading. At every nominal DEA concentration, the most concentrated species is $DEAH^+$, closely followed by bicarbonate. Given that $DEAH^+$ and bicarbonate also have similar acidity (with pK_a values of 8.9 and 10.3, respectively) these are both likely proton donors for RCC and HER, with $DEAH^+$ most strongly promoting HER. While bicarbonate may serve as a proton donor or indirect source of carbamate/free CO_2, we do not expect it to be feasible to directly convert. Instead, at more positive potentials, the moderate CO selectivity likely arises through thermodynamic preference for indirect RCC over HER in addition to a moderate availability of carbamates and free/unbound CO_2 at the interface – with each being roughly similar concentrations in solution. At more negative potentials, higher current density will also drive a locally alkaline pH that will limit both free CO_2 and carbamates at the interface. As these species become diffusion limited at the interface with increasing current density, there is still an excess of $DEAH^+$, so HER is promoted. Thus, RCC on Ni-N-C catalysts is limited to lower potentials by a combination of the intrinsic thermodynamics of RCC along with kinetic limitations imposed by the sorbent.

Experimental evidence also shows that in sequential or long-term testing, the partial pressures of CO_2 in the headspace also vary when purging with inert gas (**Figure S10**). Assuming CO_2R is also in competition with RCC at some potentials, this also leads to ambiguity of the intrinsic behavior of Ni-N-C catalysts under RCC conditions. The slightly more positive potential for RCC at the same current density (**Figure 4a**) is likely also accounted for by the decreasing CO_2 partial pressure causing an accompanying pH increase, which is indicative of CO_2 loading decreasing over time (**Figure S10**). The presence of dissolved (free) CO_2 may compete with the indirect RCC (with surface bound CO_2 adsorbates) and makes assignment of the CO selective potential region ambiguous (**Scheme 2**). Variability in dissolved CO_2 may also account for the wider variability of RCC measurements compared to CO_2R. This motivates further systematic

study with control over the concentration of the sorbent and the partial pressure of free CO_2 to decouple these contributions.

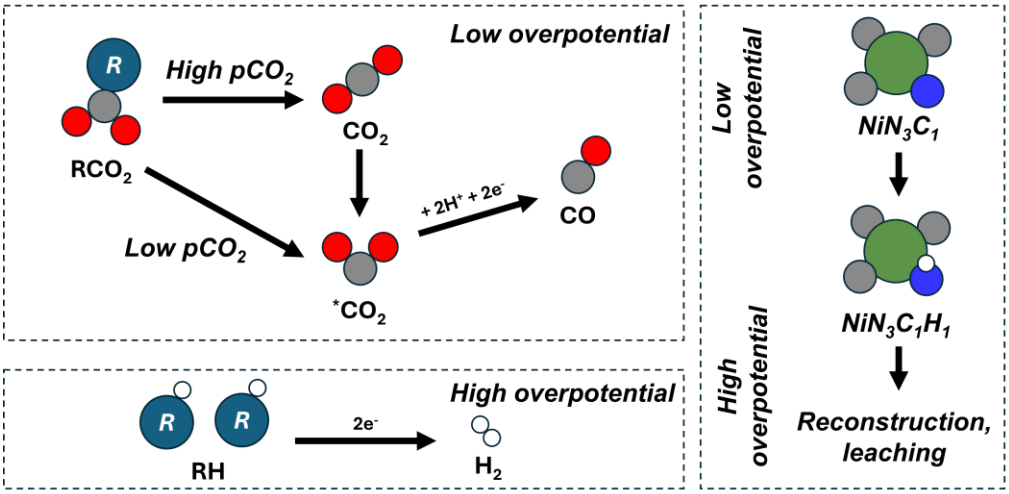

Scheme 2. Proposed competing mechanisms at low overpotential (top left), the HER mechanism at high overpotential (bottom left) and the primary speciation of the Ni site evolving as overpotential increases (right). Gray = carbon, red = oxygen, white = hydrogen, green = nickel, blue = nitrogen.

RCC Selectivity Dependence on Sorbent and CO_2 Concentration

To better understand the kinetic limitations on RCC as a result of solution speciation, we then utilized a two-compartment flow cell as a platform to evaluate the ideal conditions for RCC operation with Ni-SACs. The flow cell allowed high flux of captured CO_2 to the reactive interface, and use of an electrolyte reservoir separate from the cell allowed for quick swapping of electrolyte solutions that were pre-purged with CO_2. In order to understand the role of free CO_2, we varied partial pressures of CO_2 during the electrochemical tests (after fully saturating the solutions with CO_2 beforehand) . We conducted typical RCC measurements under pure Ar gas and pure CO_2 gas, as well as mixed 10% and 25% CO_2 gas streams that are relevant to CO_2 point

sources such as flue gas. With each of these partial pressures of CO_2, we measured different concentrations of DEA. We maintained a 1:1 concentration of $NaClO_4$:DEA for all solutions, as Na^+ plays a role in stabilizing surface intermediates and transporting reactants, which may be particularly important for the adsorption of carbamate. To interpret these results, we also used in-line pH monitoring (**Figure S11**) and the VLE models (**Figure S9**) to understand the evolving speciation under varied partial pressures of CO_2. We conducted each test at a constant potential of -1.1 V versus the standard hydrogen electrode (SHE). We used the SHE scale, rather than the reversible hydrogen electrode (RHE) scale due to the gradual increase in pH of tests under dilute CO_2 streams which leads to difficulty in setting a truly constant RHE potential.

For each CO_2 stream, increasing the concentration of DEA from 0.1 M to 0.5 M led to a higher j_{CO} (**Figure 5a**). The partial current density for HER increased with increasing sorbent concentration (**Figure 5b**) due to higher concentrations of the corresponding $DEAH^+$ (**Figure S9**) as sorbent concentration was increased from 0.1 M to 1 M DEA. We also studied the effect of CO_2 partial pressure in the incoming gas stream, using different mixtures of Ar and CO_2. Each increase in CO_2 partial pressure led to an increase in j_{CO} at 0.1 M and 0.5 M concentrations of DEA (**Figure 5c**). HER activity, on the other hand, was relatively flat with 0.1 M $NaHCO_3$, 0.1 M DEA and 1 M DEA across different CO_2 partial pressures (**Figure 5d**). The HER activity does not strongly depend on the CO_2 partial pressure, likely since it does not significantly perturb the concentrations of relevant HER proton donors (HCO_3^- and $DEAH^+$) in these systems as evidenced by the VLE models (**Figure S9)**.

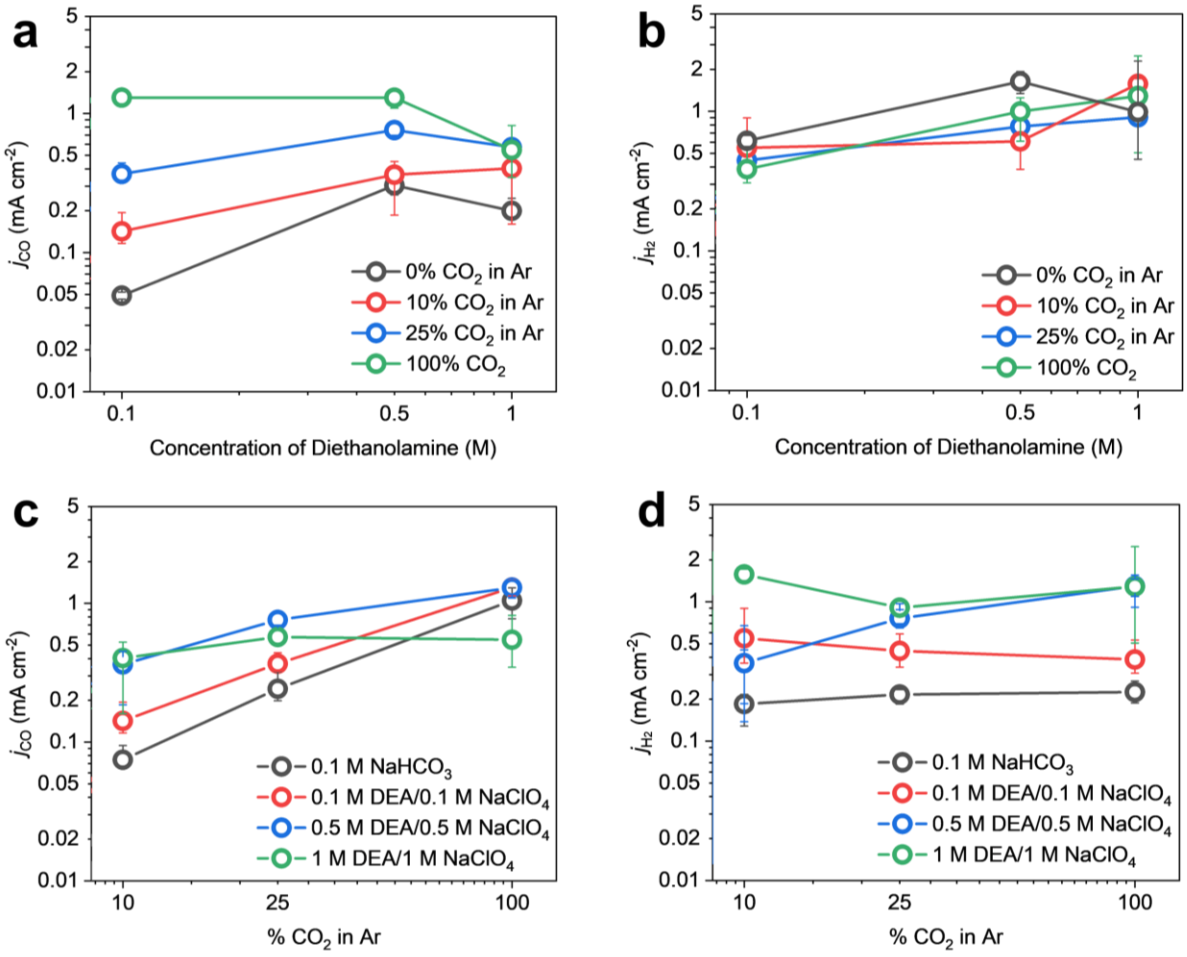

Figure 5. Evaluation of partial current density of CO at a constant potential of -1.1 V vs. SHE using Ni-N-C catalyst deposited on carbon paper and measured in a flow cell, varying a) j_{CO} and b) j_{H2} while varying concentration of the diethanolamine sorbent (with 1:1 concentration of $NaClO_4$) and c) j_{CO} and d) j_{H2} while varying partial pressure of the incoming CO_2 stream. Positive and negative error bars represent the maximum and minimum value, respectively, from at least two parallel tests.

While there are relatively small differences in starting pH (~7) between 0.5 M DEA and 1 M DEA (**Figures S11**), both indicate approximately 1:1 amine:CO_2 loading evidenced from the VLE modeling (**Figure S9**). At the saturation point, there is an increase in the amount of CO_2 in

equilibrium with the capture solution. This explains the exponential activity increase between 0.1 M and 0.5 M DEA under 0% CO_2, since despite their increase in pH over time they also begin at the CO_2 saturation point. With increased CO_2 partial pressure, there is a commensurate increase in j_{CO}. When the concentration of DEA is increased to 1 M, there are either diminishing returns or decreases in j_{CO} (**Figure 5a)**. With 100% CO_2, there is also a noticeable drop in j_{CO} between 0.5 M and 1 M DEA (**Figure 5c**). With 1 M DEA, there is very little free DEA compared to CO_2 and carbamate, which are roughly equal concentrations (**Figure S9f**). With 0.1 M DEA and 0.5 M DEA, the free DEA concentration is approximately equal to (or greater than) the carbamate and free CO_2 near the saturation point. The lack of available DEA may impede turnover of CO_2 to carbamate and subsequent adsorption and conversion of carbamates. This situation is different from previous observations of free DEA at the interface impeding CO selectivity on Ag catalysts, due to Ag catalysts primarily reducing free CO_2, rather than carbamates at mild overpotentials.[14,16] Assuming CO_2 is a less likely adsorbate than carbamate, changes in the rate of CO production at different CO_2 partial pressures then imply that the CO_2 mainly serves to maintain favorable concentrations of DEA, carbamates, and free CO_2 in solution to efficiently deliver carbamates to the interface. Increasing the amount of DEA (at low concentration, 0.1 M to 0.5 M DEA) is consistent with increasing activity due to higher carbamate concentration, suggesting RCC is prevalent, as predicted (**Figure 3**). At higher amine concentration (1 M DEA), the decrease in free DEA concentration relative to carbamates resulting in a decrease in activity suggests that Ni-N-C catalysts exhibit different behavior from metal catalysts that do not directly reduce carbamates. The FEs of Ni-N-C catalysts measured at -1.1 V vs. SHE under varied CO_2 partial pressures and DEA concentrations are summarized in **Figure S12**. Under Ar purging we observed increasing FE with DEA concentration, up to 20% with 1 M DEA. This is a clear

improvement over RCC on pure metals. Ag catalysts have been the most studied for HER, and under inert gas purging typically have FEs <10%,[14,15] especially without the use of larger cations.[18] Additionally, the use of 25 CO_2 can improve the FE of Ni-N-C catalysts up to 45%, whereas Ag catalysts have been observed to be less selective even under concentrated CO_2 streams.[16]

Notably, the results under Ar saturation have CO_2 concentrations that are less than 10% CO_2 in the headspace that generally decrease throughout each measurement and have consequent changes in j_{CO}/CO FE. These changes correlate with the drop in headspace CO_2 except for in the case of the 0.1 M $NaHCO_3$ electrolyte (**Figure S13**). $NaHCO_3$ has the lowest headspace CO_2 concentration (<1%) at the start of the test, and although there is a gradual decrease in headspace CO_2, the apparent CO FE does not decrease. We also note that 0.1 M $NaHCO_3$ consistently had lower activity than DEA containing solutions under dilute streams of CO_2 (**Figure S12**). This is despite 0.1 M DEA only having slightly <0.1 M bicarbonate under CO_2 saturated conditions. The pronounced effect on j_{CO}/CO FE, especially under Ar-purged conditions, suggests that the minority DEA/carbamate species play a much more pronounced role in the observed RCC activity, as expected. This is likely a consequence of slow ambient CO_2 release and the intrinsic kinetic difficulty of reducing bicarbonate directly.

While most tests were approximately one hour, we also conducted several longer tests with 1 M DEA to confirm consistency due to unaccounted charge (i.e. <100% total FE). We found that CO FE stayed consistent at ~40% under CO_2-saturation (**Figure S14a**) due to consistent speciation, as evidenced by the unchanged pH (7.3) and consistent gas environment. Under Ar saturation, the CO FE slowly dropped due to a gradual decrease in headspace CO_2 (5% to 3%) and increase in pH (7.3 to 7.8). For both cases, the H_2 FE increased gradually over the

course of two hours, with the total FE being ~60% upon the first GC injection and nearly 90% for the last several injections (**Figure S14b**). While the trends for j_{CO} track the CO FEs (**Figure S14c**), j_{H2} is relatively consistent in both cases (**Figure S14d**). This leads us to believe that unaccounted charge mainly results from charging currents, which may be difficult to dissipate due to the combined porosity of the Ni-N-C catalyst and carbon paper substrate. The full results of the three >2 hour tests are shown in **Figure S15**.

In Situ Investigation of Ni-N-C Active Site Structures Under Operating Conditions

Although the changing concentrations of species near the interface drive decreases in CO selectivity at higher potentials/current densities, we also sought to understand the importance of catalyst active site evolution during RCC and the extent to which it led to decreases in selectivity. When going to potentials higher than -1.1 V vs. SHE, large drops in CO selectivity were consistently observed (**Figure 6a**). After applying potentials where predominantly HER was observed, the selectivity could not be recovered by sweeping the potential back to potentials where the catalyst was previously CO selective. This suggests that there may be irreversible changes to the catalyst structure. To probe the structure around Ni sites (i.e. coordination within the carbon framework and adsorbates) as it evolved during immersion in DEA and under applied potential, we used *in situ* X-ray absorption spectroscopy (XAS). The *in situ* XAS cell mimicked the flow cell setup used for benchmarking, with an additional beveled opening in the backing plate near the cathode to allow incident X-rays through to the catalyst film (**Figure S16**).

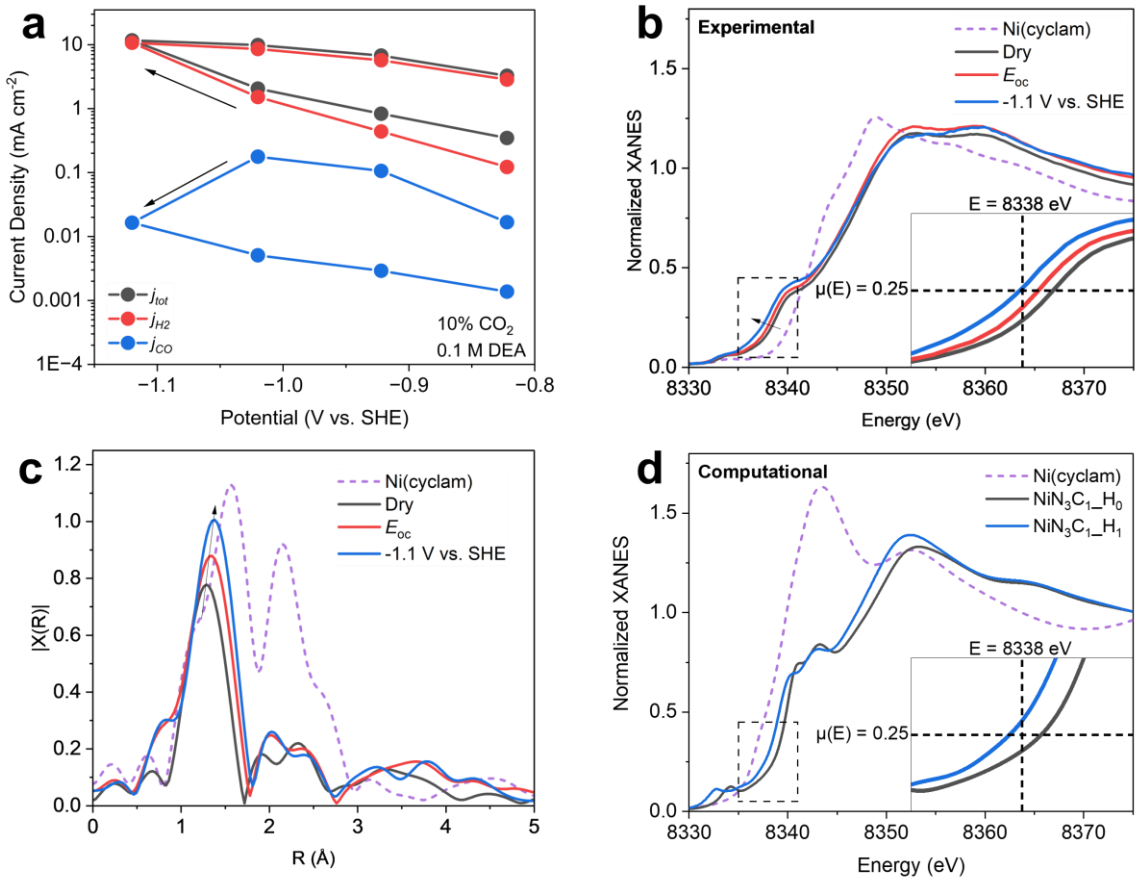

Figure 6. Evidence of the Ni-N-C catalyst restructuring assessment under RCC conditions. a) Constant potential measurements of Ni-N-C under RCC conditions (0.1 M DEA/0.1 M $NaClO_4$ with 10% CO_2 supply). b) Ni K-edge XANES of a dry Ni-N-C on carbon paper electrode compared to an electrode immersed at open circuit (E_{oc}) in CO_2-purged 1 M DEA/1 M $NaClO_4$ and an electrode in the same solution at -1.1 V vs. SHE, with c) corresponding k^2-weighted EXAFS spectra, and d) simulated XANES spectra of NiN_3C_1 with (NiN_3C_1_H_1) and without (NiN_3C_1_H_0) adsorbed hydrogen on the coordinating carbon, with the simulated spectrum of four-fold coordinated Ni-N complex Ni(cyclam) shown for comparison.

The X-ray near edge structure (XANES) spectra shows a shift of the absorption edge of the Ni-N-C samples to lower energy upon immersion of the electrode into a CO_2-saturated 1 M DEA solution, and a subsequent shift to even lower energy under an applied potential of -1.1 V vs. SHE (**Figure 6b**). Notably, some previous studies of conventional CO_2R on Ni-N-C catalysts observe similar shifts in the absorption edge under CO_2R conditions,[42–45] although typically CO_2 adsorption under open circuit conditions shows a positive shift in the adsorption edge. We hypothesize that under working conditions where indirect RCC is dominant, the primary adsorbate's CO_2) interactions with the catalyst will be similar to conventional CO_2R, while under open circuit conditions interactions with the sorbent may be more prevalent. The extended X-ray absorption fine structure (EXAFS) of the Ni-N-C catalysts under the same conditions indicates a slight bond lengthening and increase in coordination in the first shell coordination of N/C around Ni (**Figure 6c**). Since the bond lengths and scattering factors of nitrogen and carbon atoms will be similar, this could indicate restructuring of the N/C coordination around the Ni or adsorption of the sorbent/CO_2. This observation also contrasts some other EXAFS measurements of Ni-N-C catalysts measured *in situ* for CO_2R,[42,44,45] which warrants further investigation to clarify whether these observations represent restructuring around the Ni within the graphitic carbon plane, or out of plane with the sorbent.

To better understand the coordination structure based on the experimental results, we simulated the XANES spectra for likely coordination structures of the Ni-N-C. We simulated the XANES spectra of NiN_3C_1 (**Figure 6d**) and NiN_1C_3 (**Figure S17**) under both dry conditions and working conditions at -1.2 V, where the active surface is characterized by the adsorption of a single hydrogen atom for NiN_3C_1. Our experimental results showed that under working conditions, the absorption edge shifts towards lower energy compared to the dry state, indicating a partially lower

Ni oxidation state (**Figure 6b**). For the simulation of NiN_3C_1, we observed a similar absorption edge shift (~0.8 eV) to lower energy upon adsorption of a hydrogen on the coordinating carbon (**Figure 6d**). A similar trend is observed in NiN_1C_3 (**Figure S18**). The similarity in the absorption edge shift near μ(E) = 0.25 between the experimental and simulated results suggest that protonation (at least partially) drives changes to the local structure of the catalyst active sites and further supports the prevalence of NiN_3C_1 sites in the as-synthesized catalyst. More complex features in the XANES, as well as the changes at open circuit, are likely explained by the effects of the primary adsorbates (*vide supra*). These results suggest that protonation changes the local structure of the Ni-N-C active sites under working conditions and thus, protonation at the active site is consequential for RCC activity.

To further investigate the impacts of protonation on NiN_xC_{4-x} catalysts and identify possible origins of restructuring, we used theoretical calculations to probe the nature of the restructuring under initial formation of the NiN_xC_{4-x} sites and under working RCC conditions. To assess the thermodynamic stability of SACs, we calculated the relative formation energy of NiN_xC_{4-x}, as shown in **Figure 7a**. The results indicate that formation energy increases markedly with decreasing nitrogen coordination, suggesting that structures with higher nitrogen coordination are more thermodynamically stable, consistent with experimental observations of prevalent Ni-N_4 and Ni-N_3C_1 sites.

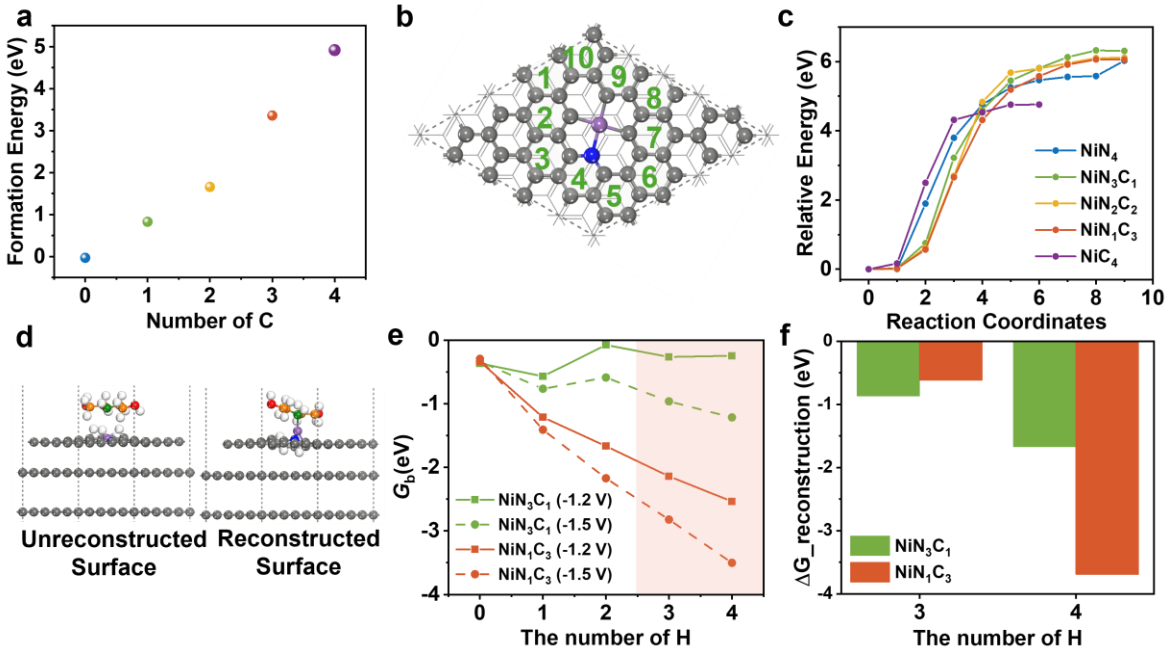

Figure 7. a) Formation energies of NiN_xC_{4-x} structures. b) Ten potential Ni transfer sites. c) Energy profile along the reaction pathway for Ni diffusion from original site to an adjacent hollow site. d) Side view of the optimized DEA adsorption on NiN_1C_3_H_3, comparing the unreconstructed and reconstructed structures. e) Gibbs free energy for co-adsorption of DEA and H on NiN_xC_{4-x} surfaces under different applied potentials. The binding energy was computed as $G_b = G_{total(NiN_xC_{4-x} + DEA + H)} - G_{NiN_xC_{4-x}} - G_{DEA} - G_H$, representing the overall stability of the DEA + H co-adsorbed states. f) Energy difference between the unreconstructed and reconstructed surfaces at -1.5 V.

To further assess dynamic stability of NiN_xC_{4-x} catalysts, we analyzed the diffusion barrier of Ni atoms migrating from their original sites to adjacent hollow sites. We designed ten possible migration paths (**Figure 7b**) and identified the most thermodynamically stable final structures by comparing the relative energies between the initial and final states. These structures were then used to determine the Ni diffusion barrier. Our calculations reveal that, at least without the assistance

of ligands from solution, such as the amine, the aggregation of dispersed Ni single atoms is unlikely to occur, as the diffusion barrier exceeds 4 eV for all catalysts. While ligand assistance likely will bring the barrier down, we can use these results to assess the relative stabilities of NiN_xC_{4-x} sites. NiC_4 appears to be less stable compared to other catalysts (**Figure 7c**), but this structure is an insignificant fraction (*vide supra*). This likely rules out Ni plating as a source of the shift of the XANES absorption edge to the left.

Under operating conditions, metal sites may undergo chemical corrosion due to interactions with DEA that leads to Ni leaching. We examined two adsorption configurations of DEA: (1) Physisorption, where DEA interacts weakly with the surface, and (2) Chemisorption, where DEA forms a chemical bond with Ni, potentially leading to metal leaching (**Figure 6d**). To probe the driving force for surface restructuring, we evaluated the binding energies of DEA and H on NiN_3C_1 and NiN_1C_3 under different applied potentials. The red region in **Figure 7e** marks the potential range where the reconstructed surface becomes more stable. Our results show that as the potential becomes more negative, the increasing hydrogen coverage leads to more negative binding energies of DEA, suggesting a higher tendency for surface reconstruction and leaching. Comparing NiN_1C_3 and NiN_3C_1, we find that NiN_3C_1 is more resistant to Ni leaching, as indicated by its less negative binding energy and smaller energy difference between the reconstructed and unreconstructed surfaces (**Figure 7f**). This trend suggests that, as the number of carbon atoms increases, the tendency for Ni leaching also increases, highlighting the importance of nitrogen coordination in stabilizing single-atom Ni sites. This is consistent with observations of deactivation at more negative potentials (**Figure 6a**) and Ni leaching into solution under more negative potentials and over extended periods of time, as evidenced by inductively coupled plasma mass spectrometry (ICP-MS) of the electrolyte after electrolysis (**Figure S18**). These structural changes

likely decrease the number of active sites, therefore deactivating the catalyst. The HER activity at high overpotentials likely then at least partially originates from HER on the graphitic carbon support. We have also summarized the expected changes to the primary Ni-N-C site speciation in **Scheme 2.**

Considering catalytic activity, selectivity, and stability, we propose that NiN_3C_1 sites represent the dominant contribution to RCC performance. Therefore, to further verify the reliability of DFT in describing such systems with complex electronic structures and competing spin states,[46–51] we performed a benchmark calculation using a quantum embedding approach that performs correlated electronic structure calculations on embedded fragments,[52,53] including the $NiN_3C_1H_1$ active site and its graphitic surroundings (**Figure S19**). More details can be found in the supporting information. The DFT-computed spin states are consistent with results obtained from high-level wavefunction-based methods such as CASPT2 and CCSD(T), which supports the reliability of DFT for describing the ground state of this system and further validating the accuracy of our computational results.

Conclusions

This work brings attention to the need for co-design of catalysts, sorbents, and operating conditions to achieve optimal RCC activity. We found that by using a catalyst that can suppress HER, RCC is possible at low overpotentials. Carbon-based products are obtained through generating CO_2 adsorbates at operating potentials where RCC is kinetically viable. Computational analysis initially predicted RCC through both direct (carbamate reduction) and indirect (C-N bond breaking followed by reduction of adsorbed-CO_2) pathways. We mainly experimentally observed RCC selectivity at potentials where indirect RCC should be dominant, and experimental evidence also

suggests a role of free CO_2 in equilibrium with the sorbent. To demonstrate this, we experimentally studied different concentrations of CO_2 constantly fed into the system. Although there is not strong experimental evidence for the direct electroreduction of carbamates (i.e. without an initial C-N bond breaking step) on Ni-N-C catalysts, the presence of a sorbent (DEA) can nonetheless enhance the rate of CO production (compared to a solution only containing sodium bicarbonate) when a dilute CO_2 source is present. This enhancement is especially pronounced without an external source of CO_2, where bicarbonate solutions are ineffective as a CO_2 source to the catalyst, and results in a 19-fold enhancement (evidenced by the partial current density) in the rate of CO production in solutions of 0.5 M DEA. There is also a 3-fold enhancement in the rate at 10 and 25% concentrations of CO_2, which are most relevant for implementation of RCC from industrial sources. These rates are achievable at lower overpotentials than observed for Ag based catalysts, which have been observed to have a significantly RCC onset for CO at potentials, as well as significantly lower selectivity for CO. Mechanistically, these enhancements are also significant, as they point to the unique ability of Ni-N-C catalysts to proceed through an RCC mechanism, rather than just proceeding through CO_2R in the presence of amines. While open circuit corrosion of metal catalysts for RCC was previously documented, previous works on Ni-N-C catalysts for RCC have not documented the deactivation of the catalyst resulting from restructuring and leaching. These insights will be important for further developing stable single atom active sites for RCC. To enable enhancements from RCC, the potential must be such that the Ni-N-C sites do not restructure and the supply of carbamates/CO_2 near the interface is not depleted too rapidly. Our insights into the importance of the RCC microenvironment as well as the corresponding catalyst stability highlight the importance of co-designing catalysts and sorbents, as well as tailoring concentrations of sorbent to the available stream of CO_2.

Experimental Section

Computational Methods. All plane-wave density functional theory (DFT) calculations were performed using the Vienna Ab Initio Simulation Package (VASP),[54,55] employing the Perdew–Burke–Ernzerhof (PBE) functional within the generalized gradient approximation (GGA) framework.[56] Projector-augmented-wave pseudopotentials(PAW) were employed with a plane-wave energy cutoff of 400 eV. The model systems were constructed using a p(5 × 5) unit cell with three atomic layers. The bottom two layers of the slab were fixed to mimic the bulk, while the top layer and all adsorbates were fully relaxed to represent the interfacial region. A vacuum space of 20 Å was added along the z-direction to eliminate interactions between periodic images. For solvation and surface charging calculations, all structures were symmetrized and the simulation cell was extended to 60 Å in the z-direction to accommodate the implicit solvation region. Geometry optimizations were considered converged when reaching a gradient smaller than 0.05 eV/Å, with a threshold of 1×10^{-5} eV for wave-function calculation. Γ-point (1 × 1 × 1) K-point mesh was used for all geometry optimizations. Gibbs free energies for adsorbates are obtained from the DFT energies with ZPE and entropy corrections determined from frequency calculations performed for all the considered structures using the Harmonic Oscillator approximation. The grand canonical free energy was evaluated by the grand canonical density functional theory (GCDFT) calculations, which is a surface charging technique. Details can be found in the supporting information and our previous article.[15,57,58] Details of high-level embedding ab initio calculations are given in the SI.

Catalyst Synthesis. The catalyst synthesis was adapted from literature.[28] Briefly, 2.5 g of amorphous silica nanoparticles (Thermo Scientific, 99.9%) were suspended in nanopure water, sonicated, and then heated at 1000 °C in a crucible for one hour. Then, 50 mg of nickel chloride

hexahydrate was dissolved in 2.5 mL 1-ethyl-3-methylimidazolium (EMIM-DCA) and added to the crucible with the annealed silica. The mixture was then placed back in a furnace and heated at 900-1000 °C for three hours. After cooling, the silica templates were etched away by etching three times with 2 M NaOH at 80 °C for three hours, and then a final etch with 1 M HCl in ethanol. The final product was collected by centrifugation.

Electrolyte Preparation. Electrolyte solutions for RCC were prepared by 1:1 molar amounts of sodium perchlorate (Sigma-Aldrich, ≥98.0%) and diethanolamine (Sigma-Aldrich, ≥99.0%). All solutions were treated by stirring with Chelex (Sigma-Aldrich, 50-100 mesh) for at least one hour prior to use. Electrolytes were purged with vigorous CO_2 bubbling for at least 15 minutes to achieve a stable pH/outlet flow rate of CO_2 from solution before use, then subsequently purged with the working gas.

Electrode Preparation. For RDE measurements, 20 µL of the catalyst suspension (10 mg/mL, 0.3 Nafion/catalyst mass ratio in ethanol) was dropcast onto a glassy carbon disk electrode (Pine Research Instrumentation, 5 mm diameter) and allowed to dry naturally in air. For flow cell measurements, pieces of AvCarb MGL370 (Fuel Cell Store) were cut into 4 cm x 4 cm squares and 200 µL of catalyst dispersion (6 mg/mL, 0.3 Nafion/catalyst mass ratio in ethanol) was dropcast onto the squares and allowed to dry naturally. Nafion was added from a corresponding amount of 5 wt% solution (Sigma-Aldrich).

Electrochemical Measurements. All electrochemical measurements were conducted on a VSP-300 poteniostat. RDE measurements were conducted in a sealed rotating cell, as described previously. Flow cell measurements were conducted in custom 3D printed flow cells (Formlabs, Clear v4 resin). The two-compartment cell was separated using an anion exchange membrane

(Fumasep FAS-50, Fuel Cell Store). All measurements used a leakless Ag/AgCl electrode (Innovative Instruments Inc.) and typically used an iridium oxide on carbon paper anode (Dioxide Materials). The anolyte was either a 0.1 M or 1 M $NaHCO_3$ solution (to correspond to the same catholyte composition for CO_2R) or 1 M $NaClO_4$ (for RCC). The anolyte compartment was static and contained ~9 mL of electrolyte. For most tests, a pH probe (H1001, Hanna Instruments) was placed in-line in the catholyte flow loop by screwing into a 3D printed holder.

Gaseous products were detected with an on-line gas chromatogram (SRI 8610C MG#5) equipped with a 12 ft MolSieve 5A column (for H_2 separation), 6 ft HayeSep D column (for CO/CO_2 separation), flame ionization detector (FID) for CO/CO_2 quantification and a thermal conductivity detector (TCD) for H_2 quantification. RDE measurements were conducted at 800 rpm unless otherwise noted and flow cell measurements were conducted at a liquid flow rate of 40 mL/min with 75 mL of recirculating electrolyte unless otherwise noted.

X-ray Absorption Spectroscopy. X-ray absorption spectroscopy (XAS) measurements were conducted in fluorescence mode at beamline 4-1 of the Stanford Synchrotron Radiation Lightsource (SSRL). *In situ* XAS measurements were conducted in 3D printed flow cells similar to those used for performance benchmarking, except with a beveled opening on the front faceplate. The catalyst electrodes were sealed in on the front of the working chamber using Kapton tape. Data was processed using Larix/Larch or Athena. Fittings were processed in Artemis To obtain an estimate of the amplitude reduction factor, S_0^2, we fitted the measure spectra of Ni(cyclam), a molecular complex assumed to have a first shell Ni-N coordination of 4. By fixing the coordination number at a value of 4, we obtained $S_0^2 = 0.8 \pm 0.2$, so we carried forward a fixed value of $S_0^2 = 0.85$ for the fitting of the Ni-N-C EXAFS. For the Ni-N-C fitting we also fixed the Ni-N/C distance as 1.87 Å (from the optimized $Ni-N_4$ structure), the Ni-C

coordination number to be the four minus the Ni-N coordination number, and guessed all other parameters.

ICP-MS. ICP-MS standards were prepared from nickel nitrate hexahydrate and prepared in a matrix of 0.5 M DEA/0.5 $NaClO_4$. Aliquots from the electrolyte were diluted 100-fold in a matrix of 0.5 M DEA/0.5 M $NaClO_4$.

Supporting Information Available: Additional computational details, additional data related to the flow cell testing of the Ni-N-C catalyst, VLE modeling of DEA, photo of assembled cell for XAS, and quantification of Ni leaching from flow cell testing.

Corresponding Authors

*Anastassia N. Alexandrova** – Department of Chemical and Biomolecular Engineering, University of California, Los Angeles, Los Angeles, CA 90095, United States

Email: alexandrova@g.ucla.edu

*Christopher Hahn** – Materials Science Division, Lawrence Livermore National Laboratory, 7000 East Avenue, Livermore, CA 94550, United States

Email: hahn31@llnl.gov

Acknowledgements

This work was primarily supported as part of the Center for Closing the Carbon Cycle, an Energy Frontier Research Center funded by the U.S. Department of Energy, Office of Science, Basic Energy Sciences under Award Number DE-SC0023427. Work by R.D.R., H.J., A.P. and C.H. was performed under the auspices of the U.S. Department of Energy by Lawrence Livermore National Laboratory (LLNL) under Contract DE-AC52-07NA27344. LLNL release

number: LLNL-JRNL-2004640. Use of the Stanford Synchrotron Radiation Lightsource, SLAC National Accelerator Laboratory, is supported by the U.S. Department of Energy, Office of Science, Office of Basic Energy Sciences under Contract No. DE-AC02-76SF00515. The authors acknowledge the use of ChatGPT for minor language and grammar editing.

Competing Interests

The authors declare no competing interests.

References

(1) El Hadri, N.; Quang, D. V.; Goetheer, E. L. V.; Abu Zahra, M. R. M. Aqueous Amine Solution Characterization for Post-Combustion CO2 Capture Process. *Appl. Energy* **2017**, *185*, 1433–1449. https://doi.org/10.1016/j.apenergy.2016.03.043.

(2) Rochelle, G. T. Amine Scrubbing for CO2 Capture. *Science* **2009**, *325* (5948), 1652–1654. https://doi.org/10.1126/science.1176731.

(3) Gao, W.; Liang, S.; Wang, R.; Jiang, Q.; Zhang, Y.; Zheng, Q.; Xie, B.; Ying Toe, C.; Zhu, X.; Wang, J.; Huang, L.; Gao, Y.; Wang, Z.; Jo, C.; Wang, Q.; Wang, L.; Liu, Y.; Louis, B.; Scott, J.; Roger, A.-C.; Amal, R.; He, H.; Park, S.-E. Industrial Carbon Dioxide Capture and Utilization: State of the Art and Future Challenges. *Chem. Soc. Rev.* **2020**, *49* (23), 8584–8686. https://doi.org/10.1039/D0CS00025F.

(4) Dongare, S.; Zeeshan, M.; Aydogdu, A. S.; Dikki, R.; Kurtoğlu-Öztulum, S. F.; Coskun, O. K.; Muñoz, M.; Banerjee, A.; Gautam, M.; Ross, R. D.; Stanley, J. S.; Brower, R. S.; Muchharla, B.; Sacci, R. L.; Velázquez, J. M.; Kumar, B.; Yang, J. Y.; Hahn, C.; Keskin, S.; Morales-Guio, C. G.; Uzun, A.; Spurgeon, J. M.; Gurkan, B. Reactive Capture and Electrochemical Conversion of CO2 with Ionic Liquids and Deep Eutectic Solvents. *Chem. Soc. Rev.* **2024**, *53* (17), 8563–8631. https://doi.org/10.1039/D4CS00390J.

(5) Freyman, M. C.; Huang, Z.; Ravikumar, D.; Duoss, E. B.; Li, Y.; Baker, S. E.; Pang, S. H.; Schaidle, J. A. Reactive CO2 Capture: A Path Forward for Process Integration in Carbon Management. *Joule* **2023**, *7* (4), 631–651. https://doi.org/10.1016/j.joule.2023.03.013.

(6) Langie, K.; Bak, G.; Lee, U.; Ki Lee, D.; Woo Lee, C.; Jeong Hwang, Y.; Hye Won, D. Advances in the Direct Electro-Conversion of Captured CO 2 into Valuable Products. *J. Mater. Chem. A* **2024**, *12* (18), 10597–10613. https://doi.org/10.1039/D4TA01178C.

(7) Li, M.; Irtem, E.; Iglesias Van Montfort, H.-P.; Abdinejad, M.; Burdyny, T. Energy Comparison of Sequential and Integrated CO2 Capture and Electrochemical Conversion. *Nat. Commun.* **2022**, *13* (1), 5398. https://doi.org/10.1038/s41467-022-33145-8.

(8) Xia, Q.; Zhang, K.; Zheng, T.; An, L.; Xia, C.; Zhang, X. Integration of CO_2 Capture and Electrochemical Conversion: Focus Review. *ACS Energy Lett.* **2023**, *8* (6), 2840–2857. https://doi.org/10.1021/acsenergylett.3c00738.

(9) Kazemifar, F. A Review of Technologies for Carbon Capture, Sequestration, and Utilization: Cost, Capacity, and Technology Readiness. *Greenh. Gases Sci. Technol.* **2022**, *12* (1), 200–230. https://doi.org/10.1002/ghg.2131.

(10) Legrand, U.; Apfel, U.-P.; Boffito, D. C.; Tavares, J. R. The Effect of Flue Gas Contaminants on the CO2 Electroreduction to Formic Acid. *J. CO2 Util.* **2020**, *42*, 101315. https://doi.org/10.1016/j.jcou.2020.101315.
(11) Gautam, M.; Hofsommer, D. T.; Uttarwar, S. S.; Theaker, N.; Paxton, W. F.; Grapperhaus, C. A.; Spurgeon, J. M. The Effect of Flue Gas Contaminants on Electrochemical Reduction of CO2 to Methyl Formate in a Dual Methanol/Water Electrolysis System. *Chem Catal.* **2022**, *2* (9), 2364–2378. https://doi.org/10.1016/j.checat.2022.08.001.
(12) Ko, B. H.; Hasa, B.; Shin, H.; Jeng, E.; Overa, S.; Chen, W.; Jiao, F. The Impact of Nitrogen Oxides on Electrochemical Carbon Dioxide Reduction. *Nat. Commun.* **2020**, *11* (1), 5856. https://doi.org/10.1038/s41467-020-19731-8.
(13) Kowalski, R. M.; Banerjee, A.; Yue, C.; Gracia, S. G.; Cheng, D.; Morales-Guio, C. G.; Sautet, P. Electroreduction of Captured CO2 on Silver Catalysts: Influence of the Capture Agent and Proton Source. *J. Am. Chem. Soc.* **2024**, *146*, 20728–20741. https://doi.org/10.1021/jacs.4c03915.
(14) Shen, K.; Cheng, D.; Reyes-Lopez, E.; Jang, J.; Sautet, P.; Morales-Guio, C. G. On the Origin of Carbon Sources in the Electrochemical Upgrade of CO2 from Carbon Capture Solutions. *Joule* **2023**, *7* (6), 1260–1276. https://doi.org/10.1016/j.joule.2023.05.010.
(15) Choi, J.; Chiu, S.; Banerjee, A.; Sacci, R. L.; Veith, G. M.; Stieber, C.; Hahn, C.; Alexandrova, A. N.; Morales-Guio, C. G. Corrosion and Enhanced Hydrogen Evolution in Electrochemical Reduction of Ammonium Carbamate on Transition Metal Surfaces. *J. Phys. Chem. Lett.* **2024**, *15*, 8007–8017. https://doi.org/10.1021/acs.jpclett.4c01638.
(16) Safipour, J.; Weber, A. Z.; Bell, A. T. Detrimental Effects of Monoethanolamine and Other Amine-Based Capture Agents on the Electrochemical Reduction of CO2. *ACS Energy Lett.* **2023**, *8*, 5012–5017. https://doi.org/10.1021/acsenergylett.3c01953.
(17) Chen, L.; Li, F.; Zhang, Y.; Bentley, C. L.; Horne, M.; Bond, A. M.; Zhang, J. Electrochemical Reduction of Carbon Dioxide in a Monoethanolamine Capture Medium. *ChemSusChem* **2017**, *10* (20), 4109–4118. https://doi.org/10.1002/cssc.201701075.
(18) Lee, G.; Li, Y. C.; Kim, J.-Y.; Peng, T.; Nam, D.-H.; Sedighian Rasouli, A.; Li, F.; Luo, M.; Ip, A. H.; Joo, Y.-C.; Sargent, E. H. Electrochemical Upgrade of CO2 from Amine Capture Solution. *Nat. Energy* **2020**, *6* (1), 46–53. https://doi.org/10.1038/s41560-020-00735-z.
(19) Leverick, G.; Bernhardt, E. M.; Ismail, A. I.; Law, J. H.; Arifutzzaman, A.; Aroua, M. K.; Gallant, B. M. Uncovering the Active Species in Amine-Mediated CO2 Reduction to CO on Ag. *ACS Catal.* **2023**, *13* (18), 12322–12337. https://doi.org/10.1021/acscatal.3c02500.
(20) Guan, Y.; Kümper, J.; Mürtz, S. D.; Kumari, S.; Hausoul, P. J. C.; Palkovits, R.; Sautet, P. Origin of Copper Dissolution under Electrocatalytic Reduction Conditions Involving Amines. *Chem. Sci.* **2024**, *15* (35), 14485–14496. https://doi.org/10.1039/D4SC01944J.
(21) Chiu, S.; Alexandrova, A. N. Cation Effects on CO2 Delivery to Cu Electrode in Reactive Capture of CO2. *J. Phys. Chem. Lett.* **2025**, *16*, 6032–6039. https://doi.org/10.1021/acs.jpclett.5c01022.
(22) Khurram, A.; Yan, L.; Yin, Y.; Zhao, L.; Gallant, B. M. Promoting Amine-Activated Electrochemical CO2 Conversion with Alkali Salts. *J. Phys. Chem. C* **2019**, *123* (30), 18222–18231. https://doi.org/10.1021/acs.jpcc.9b04258.
(23) Pérez-Gallent, E.; Vankani, C.; Sánchez-Martínez, C.; Anastasopol, A.; Goetheer, E. Integrating CO2 Capture with Electrochemical Conversion Using Amine-Based Capture Solvents as Electrolytes. *Ind. Eng. Chem. Res.* **2021**, *60* (11), 4269–4278. https://doi.org/10.1021/acs.iecr.0c05848.

(24) Bruggeman, D. F.; Rothenberg, G.; Garcia, A. C. Investigating Proton Shuttling and Electrochemical Mechanisms of Amines in Integrated CO2 Capture and Utilization. *Nat. Commun.* **2024**, *15* (1), 9207. https://doi.org/10.1038/s41467-024-53543-4.
(25) Kumar Verma, P.; L. McCrory, C. C. The Influence of Exogenous Amines on the Electrochemical CO 2 Reduction Activity of a Cobalt–Pyridyldiimine Catalyst. *Chem. Commun.* **2024**, *60* (62), 8039–8042. https://doi.org/10.1039/D4CC02709D.
(26) Choi, J.; Banerjee, A.; Ross, R. D.; Zhang, Z.; Chiu, S.; Sacci, R. L.; Veith, G. M.; Hahn, C.; Alexandrova, A. N.; Morales-Guio, C. G. Amine Structure Governs Corrosion Rates of Copper Catalysts in Electrochemical Reactive Capture of CO2. *J. Phys. Chem. C* **2025**, *129* (36), 16009–16019. https://doi.org/10.1021/acs.jpcc.5c03178.
(27) Li, P.; Mao, Y.; Shin, H.; Yang, Q.; Cheng, X.; Li, Y.; Li, K.; Yu, H.; Mulder, R.; Pang, W. K.; Jin, H.; Zhao, Y.; Zheng, Z.; Finch, E.; Hearn, K.; Jia, B.; Waterhouse, G. I. N.; Wang, Z.; Ma, T. Tandem Amine Scrubbing and CO2 Electrolysis via Direct Piperazine Carbamate Reduction. *Nat. Energy* **2025**, 1–12. https://doi.org/10.1038/s41560-025-01869-8.
(28) Jeong, H.-Y.; Balamurugan, M.; Choutipalli, V. S. K.; Jeong, E.; Subramanian, V.; Sim, U.; Nam, K. T. Achieving Highly Efficient CO2 to CO Electroreduction Exceeding 300 mA Cm−2 with Single-Atom Nickel Electrocatalysts. *J. Mater. Chem. A* **2019**, *7* (17), 10651–10661. https://doi.org/10.1039/C9TA02405K.
(29) Jiang, K.; Siahrostami, S.; Zheng, T.; Hu, Y.; Hwang, S.; Stavitski, E.; Peng, Y.; Dynes, J.; Gangisetty, M.; Su, D.; Attenkofer, K.; Wang, H. Isolated Ni Single Atoms in Graphene Nanosheets for High-Performance CO2 Reduction. *Energy Environ. Sci.* **2018**, *11* (4), 893–903. https://doi.org/10.1039/c7ee03245e.
(30) Möller, T.; Ju, W.; Bagger, A.; Wang, X.; Luo, F.; Thanh, T. N.; Sofia Varela, A.; Rossmeisl, J.; Strasser, P. Efficient CO 2 to CO Electrolysis on Solid Ni–N–C Catalysts at Industrial Current Densities. *Energy Environ. Sci.* **2019**, *12* (2), 640–647. https://doi.org/10.1039/C8EE02662A.
(31) Liang, S.; Huang, L.; Gao, Y.; Wang, Q.; Liu, B. Electrochemical Reduction of CO2 to CO over Transition Metal/N-Doped Carbon Catalysts: The Active Sites and Reaction Mechanism. *Adv. Sci.* **2021**, *8* (24), 2102886. https://doi.org/10.1002/advs.202102886.
(32) Hyung Kim, J.; Jang, H.; Bak, G.; Choi, W.; Yun, H.; Lee, E.; Kim, D.; Kim, J.; Young Lee, S.; Jeong Hwang, Y. The Insensitive Cation Effect on a Single Atom Ni Catalyst Allows Selective Electrochemical Conversion of Captured CO 2 in Universal Media. *Energy Environ. Sci.* **2022**, *15* (10), 4301–4312. https://doi.org/10.1039/D2EE01825J.
(33) Neves-Garcia, T.; Hasan, M.; Zhu, Q.; Li, J.; Jiang, Z.; Liang, Y.; Wang, H.; Rossi, L. M.; Warburton, R. E.; Baker, L. R. Integrated Carbon Dioxide Capture by Amines and Conversion to Methane on Single-Atom Nickel Catalysts. *J. Am. Chem. Soc.* **2024**, *146* (46), 31633–31646. https://doi.org/10.1021/jacs.4c09744.
(34) Xiao, Y. C.; Sun, S. S.; Zhao, Y.; Miao, R. K.; Fan, M.; Lee, G.; Chen, Y.; Gabardo, C. M.; Yu, Y.; Qiu, C.; Guo, Z.; Wang, X.; Papangelakis, P.; Huang, J. E.; Li, F.; O'Brien, C. P.; Kim, J.; Han, K.; Corbett, P. J.; Howe, J. Y.; Sargent, E. H.; Sinton, D. Reactive Capture of CO2 via Amino Acid. *Nat. Commun.* **2024**, *15* (1), 7849. https://doi.org/10.1038/s41467-024-51908-3.
(35) Levell, Z.; Yu, S.; Wang, R.; Liu, Y. What Is the "Other" Site in M–N–C? *J. Am. Chem. Soc.* **2024**, *147*, 603–609. https://doi.org/10.1021/jacs.4c12479.
(36) Gong, Y.-N.; Jiao, L.; Qian, Y.; Pan, C.-Y.; Zheng, L.; Cai, X.; Liu, B.; Yu, S.-H.; Jiang, H.-L. Regulating the Coordination Environment of MOF-Templated Single-Atom Nickel Electrocatalysts for Boosting CO2 Reduction. *Angew. Chem. Int. Ed.* **2020**, *59* (7), 2705–2709. https://doi.org/10.1002/anie.201914977.

(37) Li, T.; Lees, E. W.; Goldman, M.; Salvatore, D. A.; Weekes, D. M.; Berlinguette, C. P. Electrolytic Conversion of Bicarbonate into CO in a Flow Cell. *Joule* **2019**, *3* (6), 1487–1497. https://doi.org/10.1016/j.joule.2019.05.021.
(38) Pimlott, D. J. D.; Kim, Y.; Berlinguette, C. P. Reactive Carbon Capture Enables CO2 Electrolysis with Liquid Feedstocks. *Acc. Chem. Res.* **2024**, *57* (7), 1007–1018. https://doi.org/10.1021/acs.accounts.3c00571.
(39) Kozuch, S.; Shaik, S. How to Conceptualize Catalytic Cycles? The Energetic Span Model. *Acc. Chem. Res.* **2011**, *44* (2), 101–110. https://doi.org/10.1021/ar1000956.
(40) Koshy, D. M.; Chen, S.; Lee, D. U.; Stevens, M. B.; Abdellah, A. M.; Dull, S. M.; Chen, G.; Nordlund, D.; Gallo, A.; Hahn, C.; Higgins, D. C.; Bao, Z.; Jaramillo, T. F. Understanding the Origin of Highly Selective CO2 Electroreduction to CO on Ni,N-Doped Carbon Catalysts. *Angew. Chem. - Int. Ed.* **2020**, *59* (10), 4043–4050. https://doi.org/10.1002/anie.201912857.
(41) Jang, J.; Rüscher, M.; Winzely, M.; Morales-Guio, C. G. Gastight Rotating Cylinder Electrode: Toward Decoupling Mass Transport and Intrinsic Kinetics in Electrocatalysis. *AIChE J.* **2022**, *68* (5), e17605. https://doi.org/10.1002/aic.17605.
(42) Hursán, D.; Timoshenko, J.; Ortega, E.; Jeon, H. S.; Rüscher, M.; Herzog, A.; Rettenmaier, C.; Chee, S. W.; Martini, A.; Koshy, D.; Roldán Cuenya, B. Reversible Structural Evolution of Metal-Nitrogen-Doped Carbon Catalysts During CO2 Electroreduction: An Operando X-Ray Absorption Spectroscopy Study. *Adv. Mater.* **2024**, *36* (4), 2307809. https://doi.org/10.1002/adma.202307809.
(43) Martini, A.; Timoshenko, J.; Grosse, P.; Rettenmaier, C.; Hursán, D.; Deplano, G.; Jeon, H. S.; Bergmann, A.; Roldan Cuenya, B. Adsorbate Configurations in Ni Single-Atom Catalysts during ${\mathrm{CO}}_{2}$ Electrocatalytic Reduction Unveiled by Operando XAS, XES, and Machine Learning. *Phys. Rev. Lett.* **2024**, *133* (22), 228001. https://doi.org/10.1103/PhysRevLett.133.228001.
(44) Martini, A.; Hursán, D.; Timoshenko, J.; Rüscher, M.; Haase, F.; Rettenmaier, C.; Ortega, E.; Etxebarria, A.; Roldan Cuenya, B. Tracking the Evolution of Single-Atom Catalysts for the CO2 Electrocatalytic Reduction Using Operando X-Ray Absorption Spectroscopy and Machine Learning. *J. Am. Chem. Soc.* **2023**, *145* (31), 17351–17366. https://doi.org/10.1021/jacs.3c04826.
(45) Yang, H. B.; Hung, S.-F.; Liu, S.; Yuan, K.; Miao, S.; Zhang, L.; Huang, X.; Wang, H.-Y.; Cai, W.; Chen, R.; Gao, J.; Yang, X.; Chen, W.; Huang, Y.; Chen, H. M.; Li, C. M.; Zhang, T.; Liu, B. Atomically Dispersed Ni(I) as the Active Site for Electrochemical CO2 Reduction. *Nat. Energy* **2018**, *3* (2), 140–147. https://doi.org/10.1038/s41560-017-0078-8.
(46) Weser, O.; Freitag, L.; Guther, K.; Alavi, A.; Li Manni, G. Chemical Insights into the Electronic Structure of Fe(II) Porphyrin Using FCIQMC, DMRG, and Generalized Active Spaces. *Int. J. Quantum Chem.* **2021**, *121* (3), e26454. https://doi.org/10.1002/qua.26454.
(47) Abraham, V.; Mayhall, N. J. Selected Configuration Interaction in a Basis of Cluster State Tensor Products. *J. Chem. Theory Comput.* **2020**, *16* (10), 6098–6113. https://doi.org/10.1021/acs.jctc.0c00141.
(48) Rask, A. E.; Zimmerman, P. M. The Many-Body Electronic Interactions of Fe(II)–Porphyrin. *J. Chem. Phys.* **2022**, *156* (9), 094110. https://doi.org/10.1063/5.0079310.
(49) Vitale, E.; Li Manni, G.; Alavi, A.; Kats, D. FCIQMC-Tailored Distinguishable Cluster Approach: Open-Shell Systems. *J. Chem. Theory Comput.* **2022**, *18* (6), 3427–3437. https://doi.org/10.1021/acs.jctc.2c00059.

(50) Zhou, C.; Gagliardi, L.; Truhlar, D. G. Multiconfiguration Pair-Density Functional Theory for Iron Porphyrin with CAS, RAS, and DMRG Active Spaces. *J. Phys. Chem. A* **2019**, *123* (15), 3389–3394. https://doi.org/10.1021/acs.jpca.8b12479.
(51) Lei, J.; Zhu, T. Impact of Potential and Active-Site Environment on Single-Iron-Atom-Catalyzed Electrochemical CO2 Reduction from Accurate Quantum Many-Body Simulations. *ACS Catal.* **2024**, *14* (6), 3933–3942. https://doi.org/10.1021/acscatal.3c05999.
(52) Lavroff, R. H.; Kats, D.; Maschio, L.; Bogdanov, N. A.; Alavi, A.; Alexandrova, A. N.; Usvyat, D. Aperiodic Defects in Periodic Solids. *J. Chem. Phys.* **2025**, *163* (8), 084105. https://doi.org/10.1063/5.0270254.
(53) Christlmaier, E. M. C.; Kats, D.; Alavi, A.; Usvyat, D. Full Configuration Interaction Quantum Monte Carlo Treatment of Fragments Embedded in a Periodic Mean Field. *J. Chem. Phys.* **2022**, *156* (15), 154107. https://doi.org/10.1063/5.0084040.
(54) Kresse, G.; Furthmüller, J. Efficient Iterative Schemes for Ab Initio Total-Energy Calculations Using a Plane-Wave Basis Set. *Phys. Rev. B - Condens. Matter Mater. Phys.* **1996**, *54* (16), 11169–11186. https://doi.org/10.1103/PhysRevB.54.11169.
(55) Kresse, G.; Furthmüller, J. Efficiency of Ab-Initio Total Energy Calculations for Metals and Semiconductors Using a Plane-Wave Basis Set. *Comput. Mater. Sci.* **1996**, *6* (1), 15–50. https://doi.org/10.1016/0927-0256(96)00008-0.
(56) Perdew, J. P.; Burke, K.; Ernzerhof, M. Generalized Gradient Approximation Made Simple. *Phys. Rev. Lett.* **1996**, *77* (18), 3865–3868. https://doi.org/10.1103/PhysRevLett.77.3865.
(57) Zhang, Z.; Gee, W.; Sautet, P.; Alexandrova, A. N. H and CO Co-Induced Roughening of Cu Surface in CO_2 Electroreduction Conditions. *J. Am. Chem. Soc.* **2024**, *146* (23), 16119–16127. https://doi.org/10.1021/jacs.4c03515.
(58) Steinmann, S. N.; Michel, C.; Schwiedernoch, R.; Sautet, P. Impacts of Electrode Potentials and Solvents on the Electroreduction of CO_2 : A Comparison of Theoretical Approaches. *Phys. Chem. Chem. Phys.* **2015**, *17* (21), 13949–13963. https://doi.org/10.1039/C5CP00946D.

For Table of Contents Only

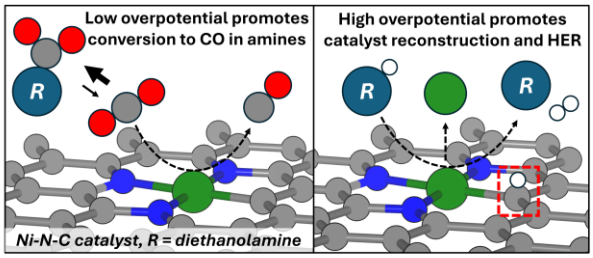

LLNL-JRNL-2004639

Lawrence Livermore National Laboratory

Supporting Information for: Solution and Active Site Speciation Drive Selectivity for Electrocatalytic Reactive Carbon Capture in

D Ross, A Alexandrova, C Hahn, Y Han, H Jeong, J Ynzunza, R Lavroff, A Banerjee, A Prajapati, C Morales-Guio, J Velazquez

January 2026

Journal of the American Chemical Society

Disclaimer

This document was prepared as an account of work sponsored by an agency of the United States government. Neither the United States government nor Lawrence Livermore National Security, LLC, nor any of their employees makes any warranty, expressed or implied, or assumes any legal liability or responsibility for the accuracy, completeness, or usefulness of any information, apparatus, product, or process disclosed, or represents that its use would not infringe privately owned rights. Reference herein to any specific commercial product, process, or service by trade name, trademark, manufacturer, or otherwise does not necessarily constitute or imply its endorsement, recommendation, or favoring by the United States government or Lawrence Livermore National Security, LLC. The views and opinions of authors expressed herein do not necessarily state or reflect those of the United States government or Lawrence Livermore National Security, LLC, and shall not be used for advertising or product endorsement purposes.

This work performed under the auspices of the U.S. Department of Energy by Lawrence Livermore National Laboratory under Contract DE-AC52-07NA27344.

Supporting Information for:

Solution and Active Site Speciation Drive Selectivity for Electrocatalytic Reactive Carbon Capture in Diethanolamine over Ni-N-C Catalysts

R. Dominic Ross,[1,2,‡] Yulan Han,[3,‡] Hui-Yun Jeong,[1,2] Jenna M. Ynzunza,[4] Robert H. Lavroff,[3] Avishek Banerjee,[5] Aditya Prajapati,[1, 2] Carlos G. Morales-Guio,[5] Jesús M. Velázquez,[4] Anastassia N. Alexandrova,[3] Christopher Hahn[1,2*]*

[1]Materials Science Division, Lawrence Livermore National Laboratory, Livermore, CA 94550

[2]Laboratory for Energy Applications for the Future (LEAF), Lawrence Livermore National Laboratory, Livermore, CA 94550

[3]Department of Chemistry and Biochemistry, University of California, Los Angeles, Los Angeles, CA 90095

[4]Department of Chemistry, University of California, Davis, Davis, CA 95616

[5]Department of Chemical and Biomolecular Engineering, University of California, Los Angeles, Los Angeles, CA 90095

[‡]These authors contributed equally.

[*]Corresponding author emails: alexandrova@g.ucla.edu, hahn31@llnl.gov

Supporting Methods

Computational details

Grand canonical density functional theory (GCDFT) calculations

The chemical potential of a coupled proton and electron is determined by the equilibrium with H_2 gas at the hydrogen electrode, expressed as:

$$\mu_{H^+/e^-} = \frac{1}{2}\mu_{H_2} - eU - \ln(10)k_B TpH \qquad (1)$$

Here, U is the applied potential vs SHE, and the last term accounts for pH correction at finite temperature.

The grand canonical free energy was evaluated by grand canonical density functional theory (GCDFT) calculations, which is a surface charging technique. Details can be found in our previous work[1–5], and here we summarize the key points.

The net charge of the electrons n_{surface} is obtained as:

$$n_{\mathrm{surface}} = N_{\mathrm{surface}} - N_{\mathrm{surface,neutral}} \qquad (2)$$

Where N_{surface} is the total number of electrons in the charged system and $N_{\mathrm{surface,neutral}}$ corresponds to the neutral reference.

The total DFT energy of the charged system is given by:

$$E_{\mathrm{surface}} = E_{\mathrm{surface,raw}} + \epsilon_{\mathrm{fermishift}} n_{\mathrm{surface}} \qquad (3)$$

Where $E_{\mathrm{surface,raw}}$ is the raw electronic energy of the surface and $\epsilon_{\mathrm{fermishift}} n_{\mathrm{surface}}$ is the term accounting for the difference($\epsilon_{\mathrm{fermishift}}$) is the reference energy of the electron between the

"internal" reference level and vacuum. Then, the grand canonical electronic energy of a surface model, $\Omega_{(U)}$, is obtained as:

$$\Omega_{(U)} = E_{\text{surface}} - n_{\text{surface}}\mu_{\text{electron}} \qquad (4)$$

Where μ_{electron} is the chemical potential of an electron, which is defined as:

$$\mu_{\text{electron}} = qU_{vac} = -eU_{\text{vac}} \qquad (5)$$

Where U_{vac} is the potential of the system with reference to the vacuum level and q is the charge of an electron. The potential of the system with reference to the vacuum can be determined by two components, the Fermi level (ϵ_{F}) with reference to the "internal" zero energy references and Fermi shift which is the difference between the "internal" energy reference and the vacuum level:

$$-eU_{\text{vac}} = \epsilon_{\text{F}} + \epsilon_{\text{fermi shift}} \qquad (6)$$

For the metallic systems, the potential-dependent grand canonical energy, $\Omega_{(U)}$, exhibits a quadratic behavior around the potential of zero charge (U_0) in the vacuum scale:

$$\Omega_{(U)} = \Omega_{(U_0)} = \frac{1}{2}C(U - U_0)^2 \qquad (7)$$

Where C is the capacitance of the surface. The potential of the system with respect to the standard hydrogen electrode (SHE) can be converted from U_{vac} as:

$$U_{\text{SHE}} = U_{\text{vac}} - 4.44 \qquad (8)$$

The linearized Poisson Boltzmann implicit solvation model implemented in VASPsol is used to represent the polarizable electrolyte region.[6] The dielectric constant of water, 78.4, and the Debye screening length corresponding to 1 M concentration of electrolytes, 3.0 Å, were used. The surface

slab is symmetrized along the z axis to avoid asymmetric potential in the implicit solvation region. Here the implicit solvent thickness is set to 60 Å for the symmetrized slab.

Quantum embedding approach

Hartree Fock (HF) calculations on the full unit cell were performed with a pob-TZVP-rev2 Gaussian basis[7] and 25 k-points (5 in each lattice vector direction of the slab), using the Crystal code.[8] Crystal was then also used to obtain Boys-localized Wannier functions (WFs) to serve as the basis for the occupied fragment orbitals. Formation of projected atomic orbitals (PAOs) and the embedded fragment density-fitted HF procedure (including projection to make the WFs and PAOs orthogonal in this partially delocalized system) was done in Cryscor[9], with a fitting basis optimized for MP2/cc-pVTZ calculations[10], resulting in FCIDUMP[11] interface files used to treat the active site with post-HF correlated calculations. Only valence WFs were obtained, meaning all post-HF calculations were performed with the frozen-core approximation.

Two embedded fragment sizes were tested, 19-atoms and 25-atoms, shown in **Figure S19,** with the remainder of the periodic, graphitic surroundings frozen in the Hartree-Fock mean field. Restricted MP2 and CCSD orbital-unrelaxed 1-particle density matrices were obtained using pySCF[12] and diagonalized to obtain natural orbital occupation numbers. The highest three "occupied" NOs and lowest three "virtual" NOs are highly fractionally occupied, leading to selection of a (6 electron,6 orbital) active space. CASSCF and CASPT2[13] calculations were subsequently and separately (i.e. state-specifically) performed in the Molpro[14] package for the lowest singlet, triplet, and quintet state. Examination of the CASSCF natural orbital occupations shows the active site ground-state to decisively be a closed-shell singlet, which is consistent with the ligand-field theory prediction of Ni^{2+} in a square planar environment ($3d_{xy}$ being the HOMO and $3d_{x2-y2}$ the LUMO), as well as our unrestricted, plane-wave DFT calculations.

Since closed-shell singlet states tend not to be multiconfigurational, and there is also some precedent for accurate CCSD(T) spin ordering from the porphyrin literature[15], we performed CCSD(T) calculations on this state and restricted-open-shell-CCSD(T) on the triplet and quintet states. These predicted a 1.30 eV singlet-triplet gap for the 19-atom fragment (versus 3.60 eV predicted by CASPT2(6,6) and 2.75 eV by CCSD), while the quintet state did not converge after hundreds of CCSD iterations but was stably hovering at ~13.2 eV above the singlet (8.2 eV for converged CASPT2) and thus deemed irrelevant. For the 25-atom fragment, CCSD(T) predicted a 2.26 eV singlet-triplet gap (versus 2.84 eV predicted by CASPT2(6,6) and 2.60 eV for CCSD). The T1 diagnostic for CCSD predicts that the ground-state may have some multiconfigurational character, with both fragment sizes giving values of ~0.037 for the singlet and ~0.128 for the triplet. An unofficial guideline is that less than 0.02 is considered decisively single-reference for closed-shell (or less than 0.03 for open-shell), and anything above 0.06 is not trustworthy to treat with a single-reference method.[16,17] For an excited-state study of this system, a multireference approach (including active space benchmarking) would certainly be required; however, we deem DFT to be trustworthy for the ground state given its agreement in terms of spin with CASPT2 and CCSD(T). There is some precedent for this from the porphyrin literature as well.[18]

Energy Span (ES) method

The span is defined by Kozuch et al.[19,20] In the Energy Span(ES) model, the reactivity of a given pathway can be approximated by the largest energy difference between a transition state on the pathway in question and an intermediate on this pathway in our work. Transitions states/free energy barriers are required to determine the ES and explicit determination of all potential dependent free energy barriers would be a huge endeavor. All elementary reaction steps are PCET

or proton transfer and hence present a strong similarity. For simplicity, we will assume that all the free energy barriers are equal, and a value of 0.4 eV has been assumed.[5]

XANES simulation

XANES spectra of the relevant structures were calculated using the finite difference method (FDM) and the Hedin–Lundqvist exchange-correlation potential as implemented in the FDMNES ab initio package.[21,22] FDMNES operates in real space and constructs a cluster of a specified radius around the absorbing atom; in our calculations, a cluster radius of 7.0 Å was used. The Ni K-edge (Z = 28) was computed with both dipole and quadrupole transitions included.

Supporting Tables

Table S1. EXAFS fitting parameters of Ni(cyclam) and Ni-N-C.

Ni(cyclam)	S_0^2	N	E_0	R (Å)	σ^2
Ni-N	0.8 ± 0.2	4	2 ± 2	2.08 ± 0.04	± 0.004
Ni-Cl		2		2.52 ± 0.04	

Table S2. EXAFS fitting parameters of Ni-N-C.

Ni-N-C	S_0^2	N	E_0	R (Å)	σ^2
Ni-N	0.85	3.3 ± 1	-7 ± 2	1.87	0.007 ± 0.002
Ni-C		0.7 ± 1			

Supporting Figures

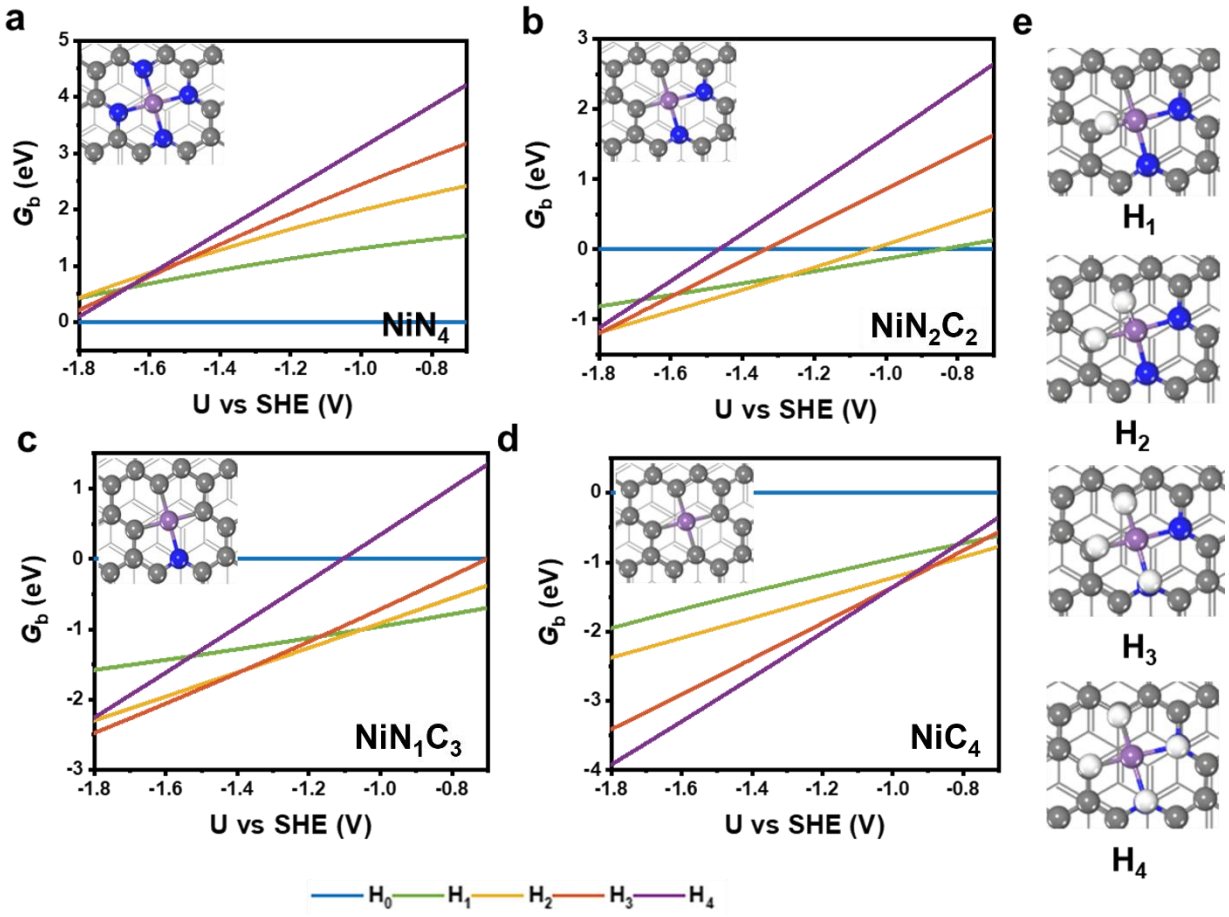

Figure S1. (a-d) Thermodynamic stability of NiN_xC_{4-x} catalyst surfaces under varying hydrogen coverages. Insets display optimized structures. (e) Representative structures illustrating different hydrogen coverages on NiC_2N_2 as an example. Color code of atoms: Ni (purple), N (blue), C (gray), and H (white).

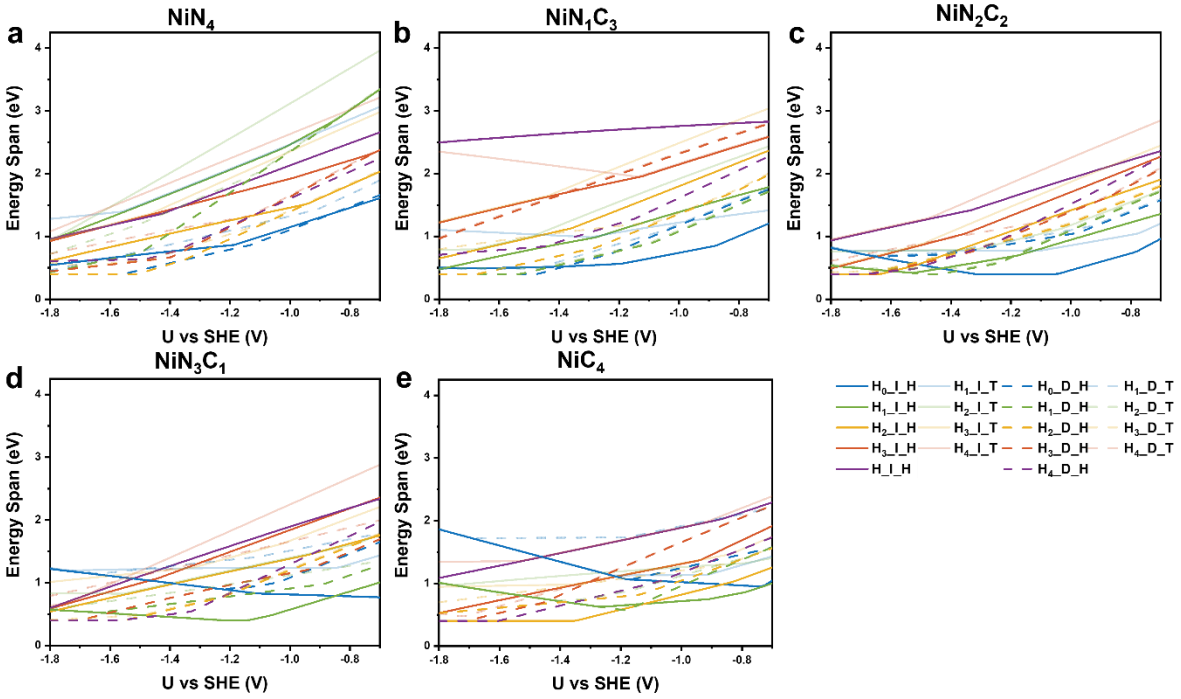

Figure S2. Calculated ES for the RCC on different NiC_xN_γ as a function of the applied potential. Hn_I_H represents the I_H reaction pathway of the catalyst with n hydrogen atoms.

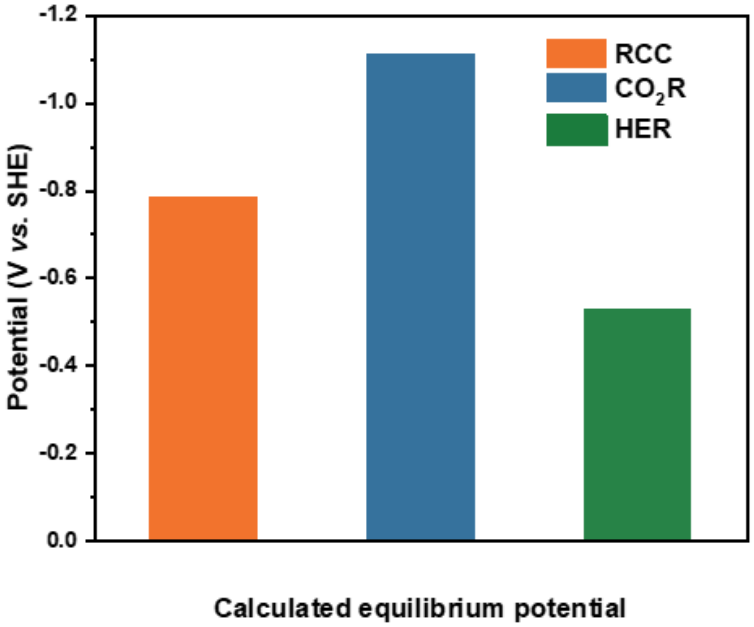

Figure S3. Calculated equilibrium potentials for RCC, CO_2R, and HER for $NaDEACO_2$ complex in DEA solvent.

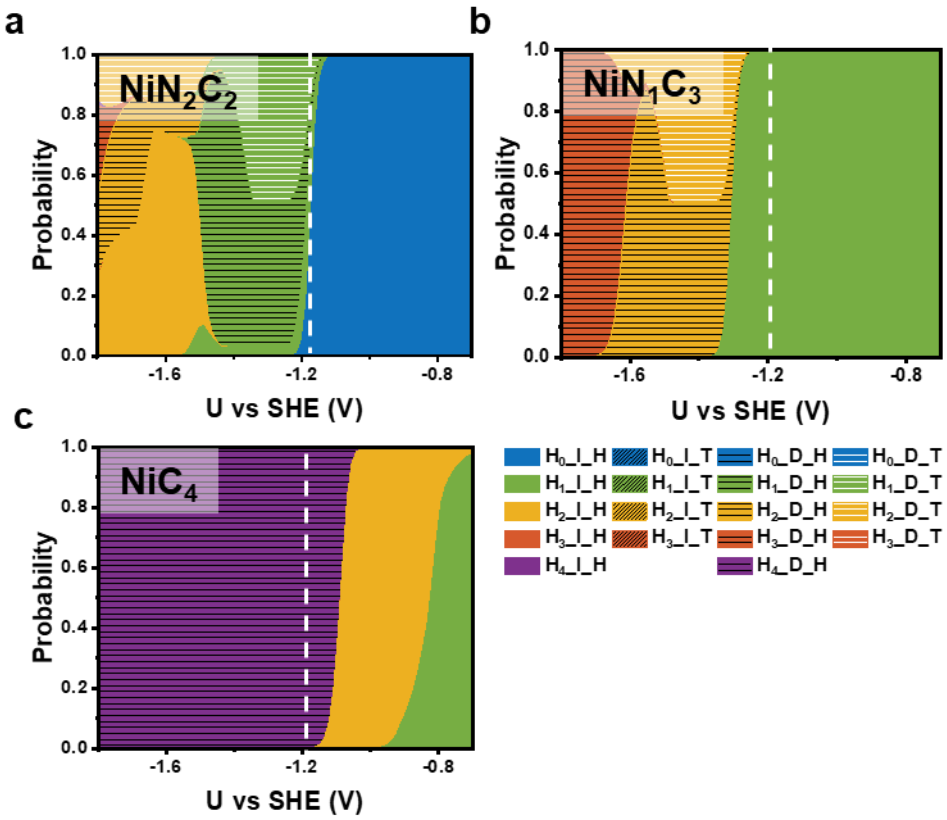

Figure S4. Probability distribution of different RCC reaction pathways for catalysts with varying hydrogen coverages, highlighting their contributions to the reaction rate.

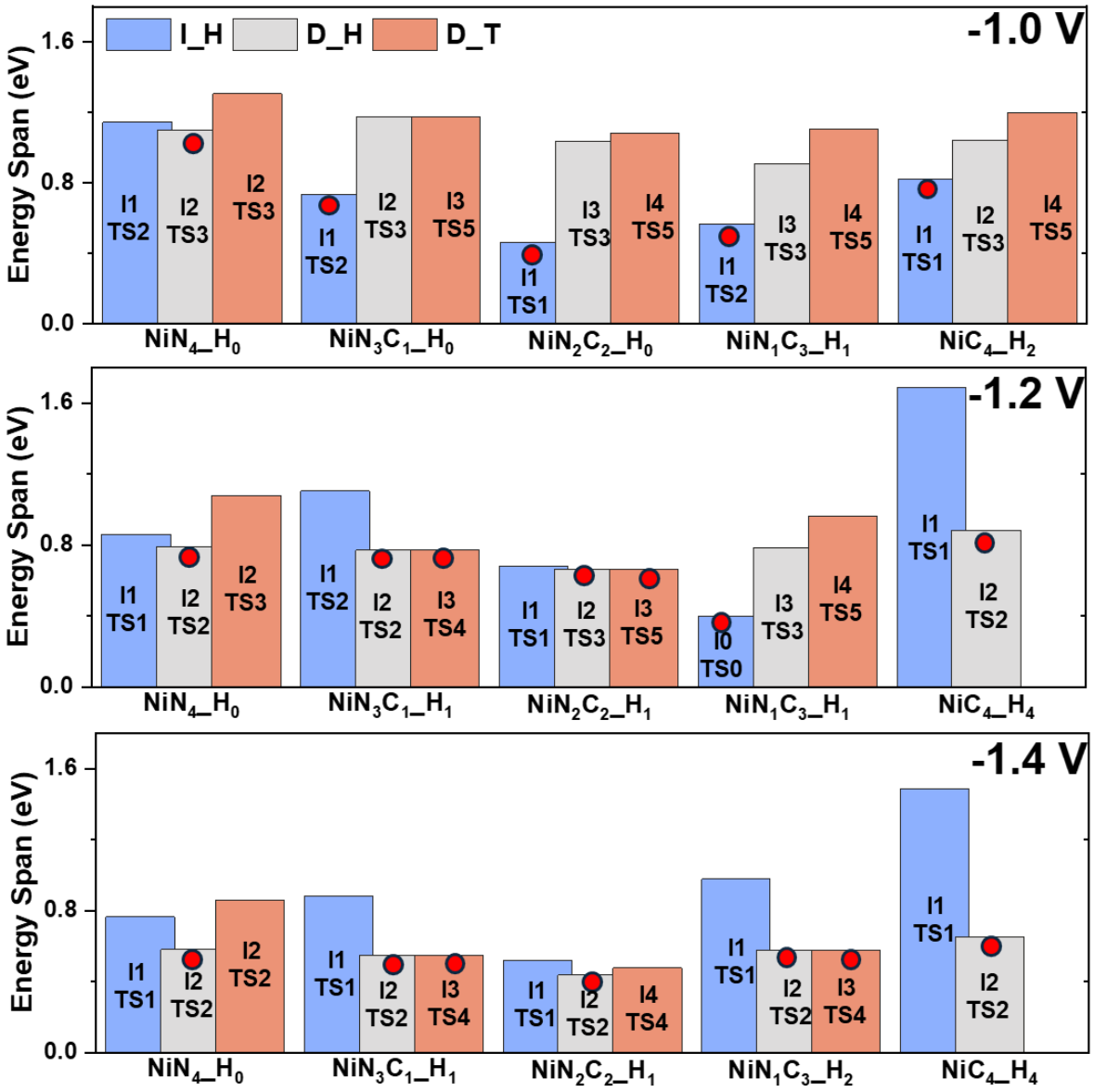

Figure S5. The rate-determining process of different reaction pathways for NiN_xC_{4-x} under varying applied voltages: -1.0 V, -1.2 V, and -1.4 V. The energy span of each reaction pathway is shown with different colored bars: I_H (blue), D_H (gray), and D_T (red). The red dots indicate the reaction progress with the highest energy contribution for each catalytic surface and voltage condition.

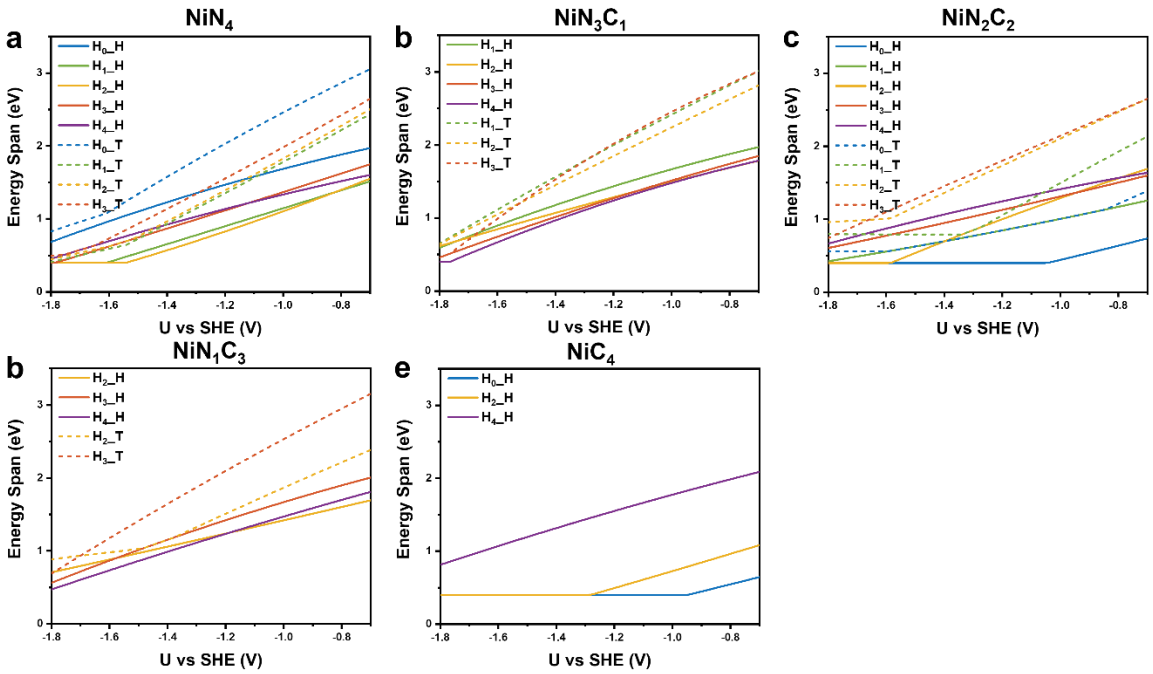

Figure S6. Calculated ES for the HER on different NiC_xN_γ as a function of the applied potential.

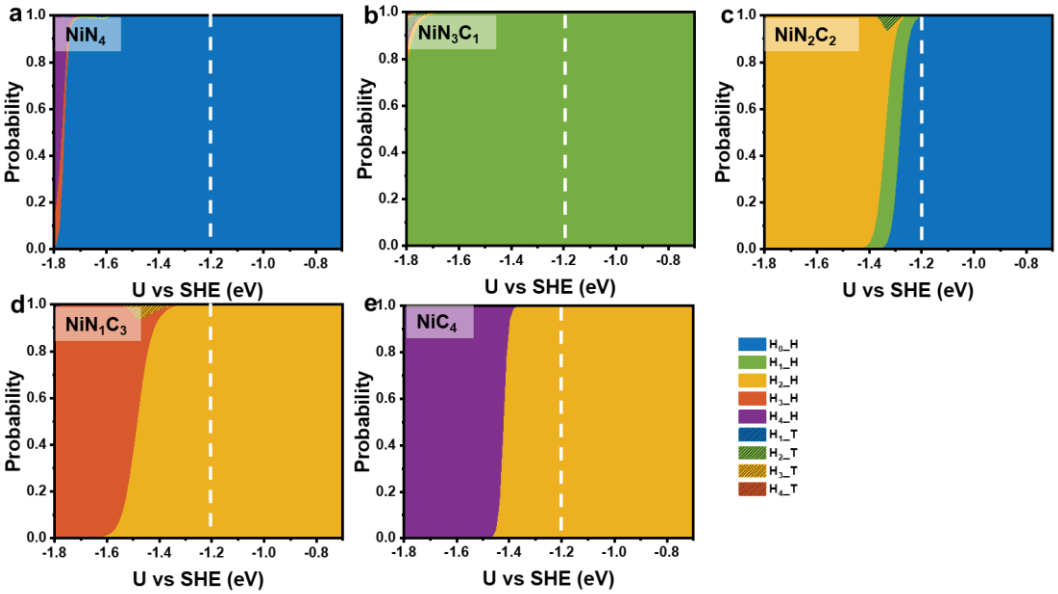

Figure S7. Probability distribution of different HER reaction pathways for catalysts with varying hydrogen coverages, highlighting their contributions to the reaction rate.

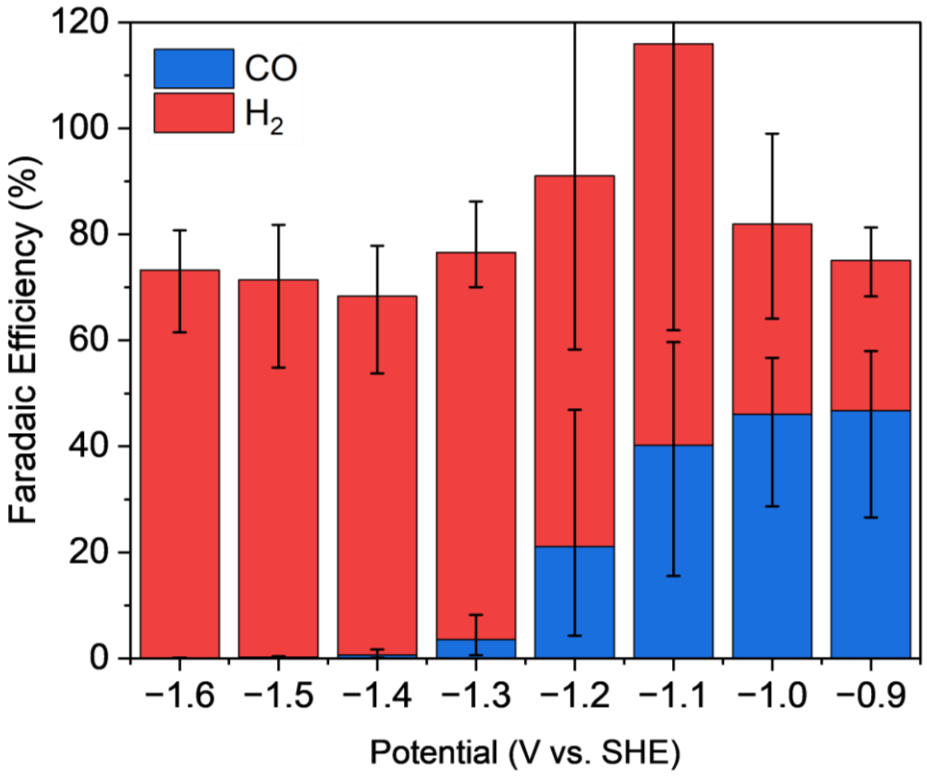

Figure S8. Faradaic efficiencies of Ni-N-C on a glassy carbon RDE measured at various potentials.

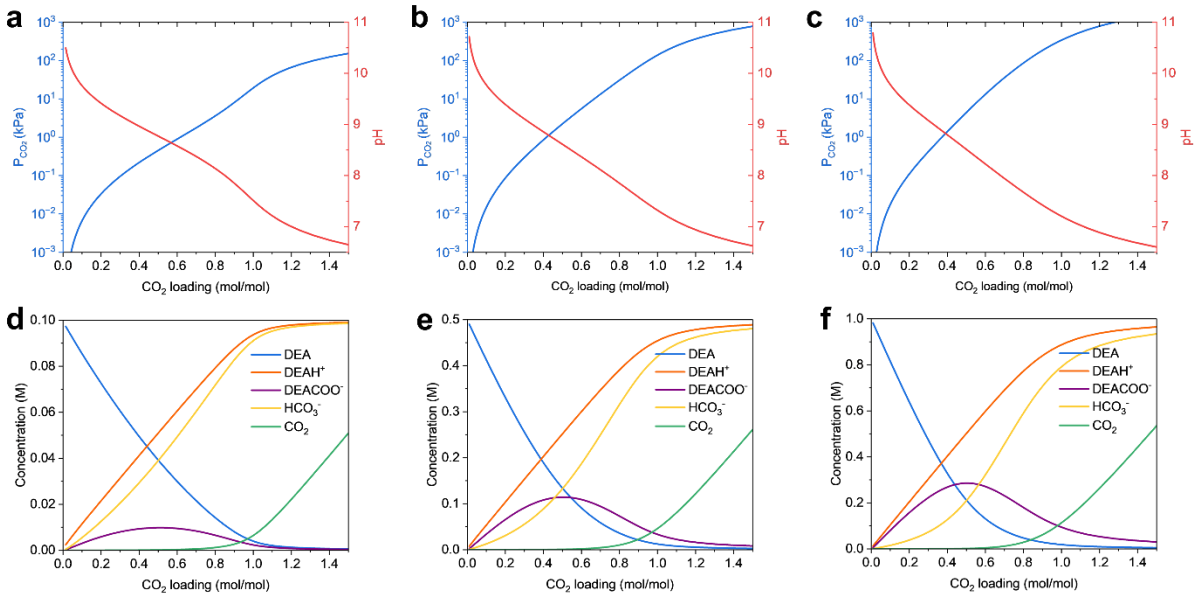

Figure S9. Vapor-liquid equilibrium models of a,d) 0.1 M DEA, b,e) 0.5 M DEA, and c,f) 1 M DEA. Details on the development of the VLE model for DEA are reported in Banerjee et al.[23]

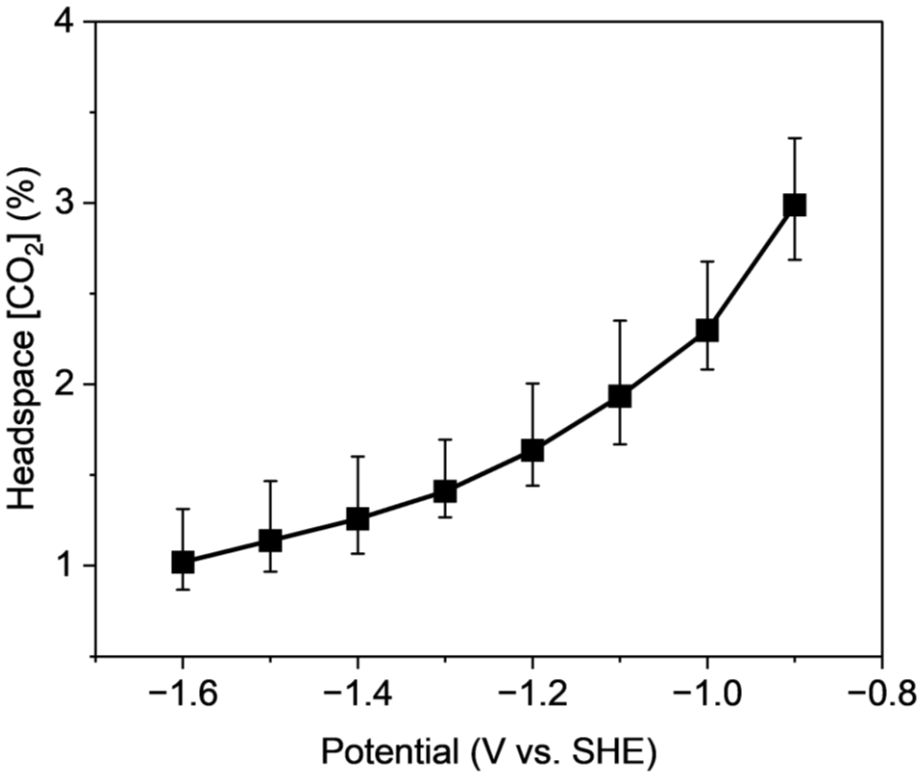

Figure S10. Headspace CO_2 concentration during potential dependent RDE tests, in which each potential was measured sequentially (for three separate parallel tests).

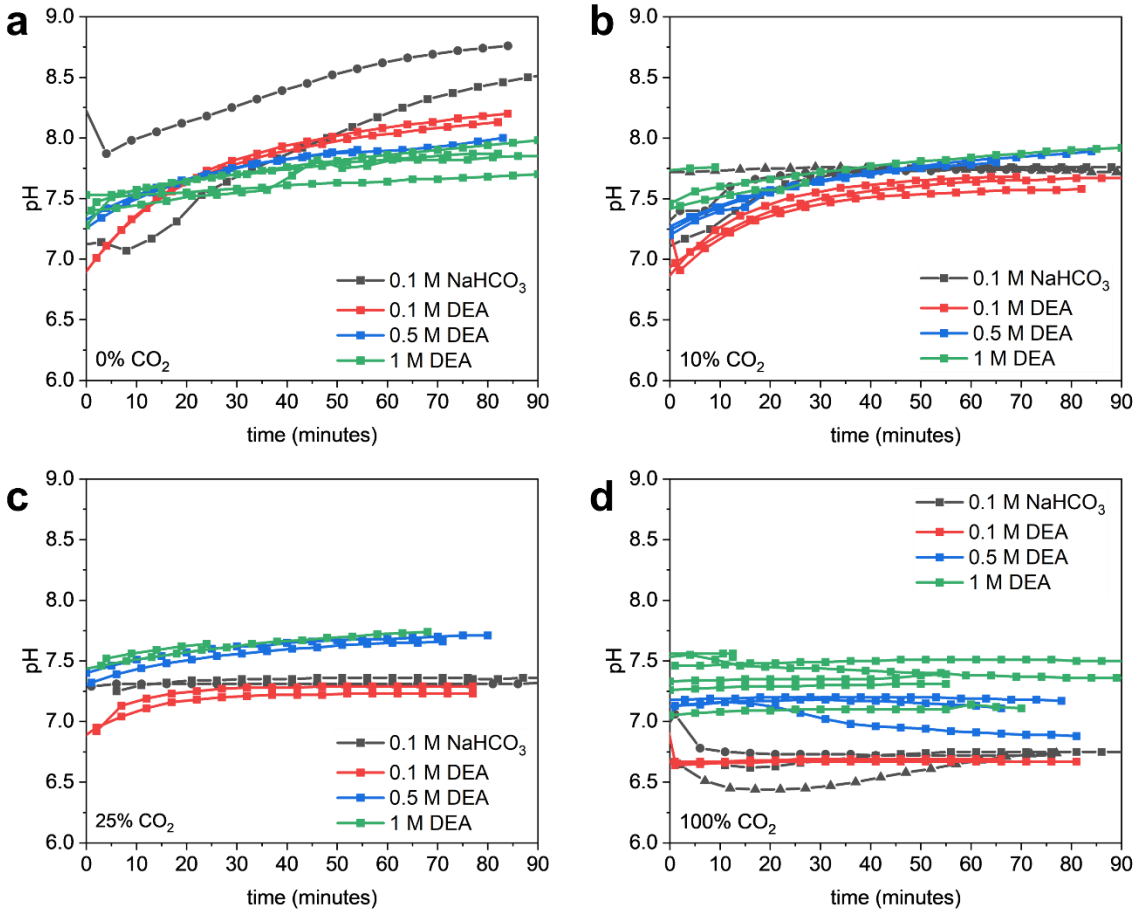

Figure S11. pH monitoring of tests (each individual line represents a separate test) from Figure 4 with a) 0% CO_2 (pure Ar), b) 10% CO_2 in Ar, c) 25% CO_2 in Ar, and d) 100% CO_2.

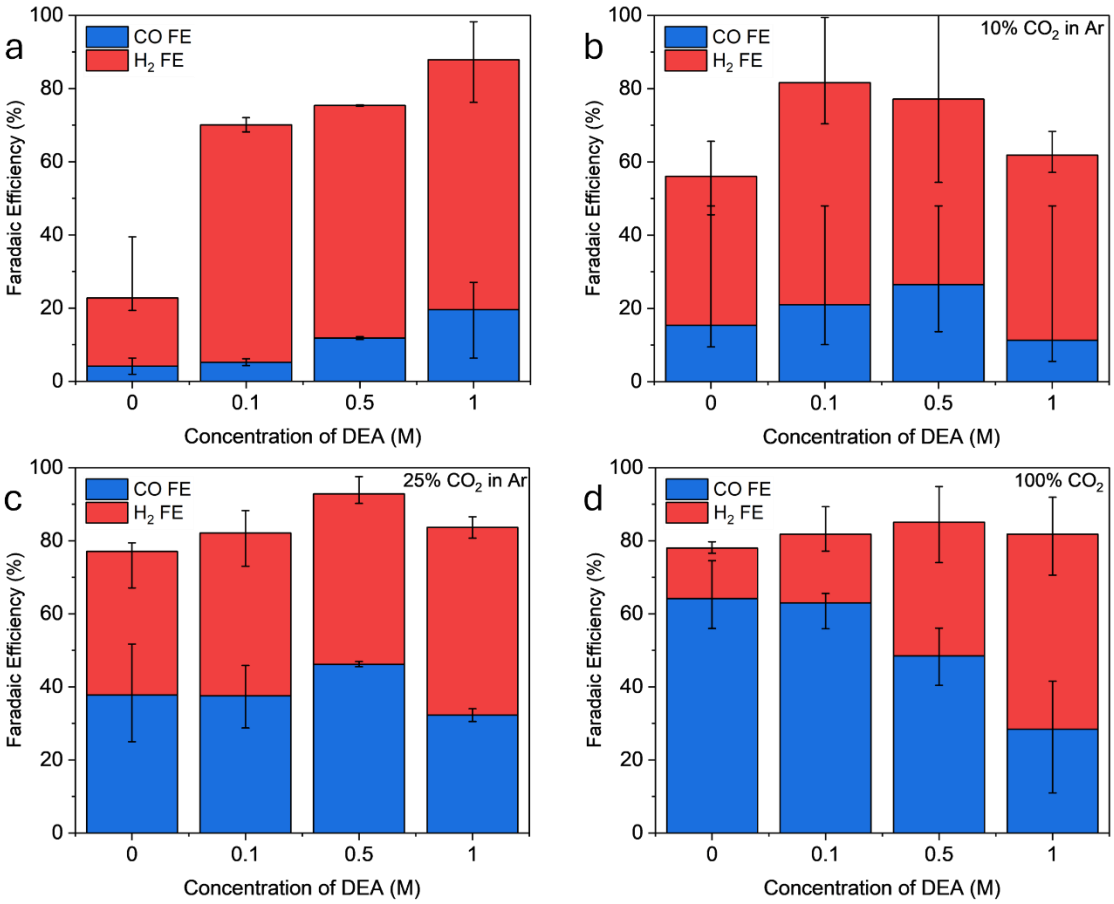

Figure S12. Faradaic efficiencies of Ni-N-C/carbon paper in a flow cell with a) pure Ar gas, b) 10% CO_2 in Ar, c) 25% CO_2 in Ar, and d) pure CO_2 gas.

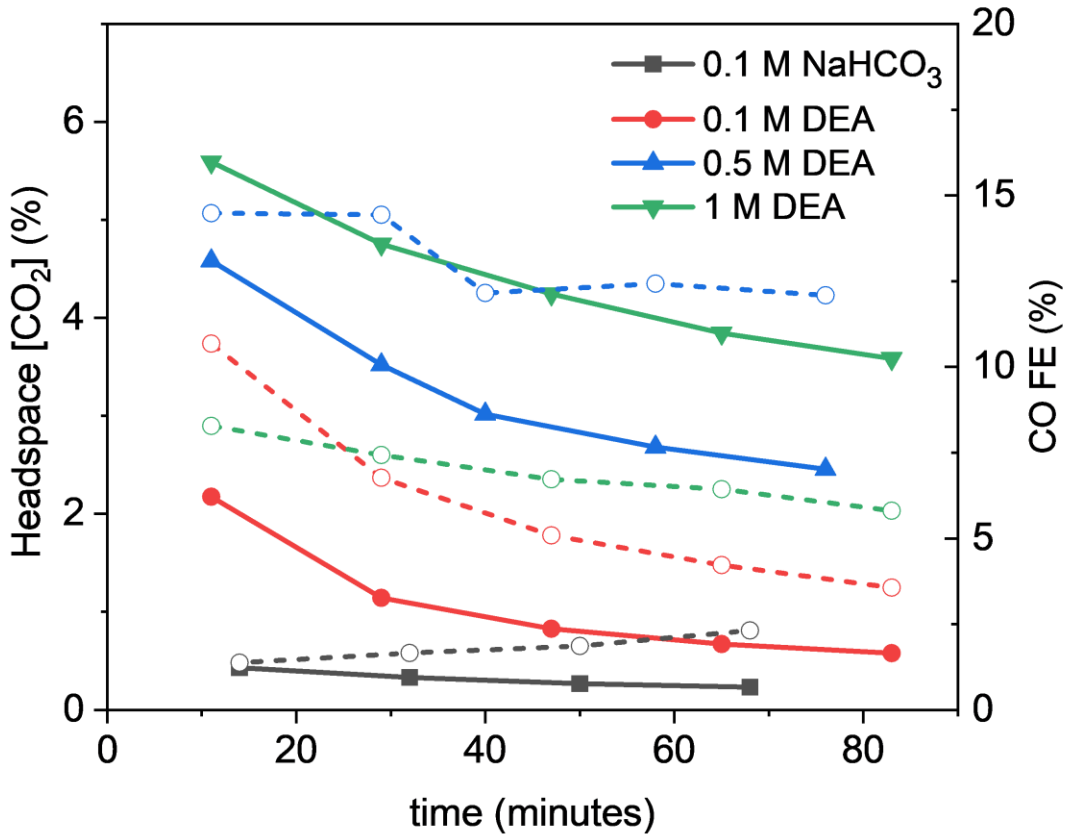

Figure S13. Representative changes in headspace CO_2 concentrations (closed shapes, left-axis) and corresponding drops in CO Faradaic efficiency (open circles, right-axis) for tests under Ar flow with different electrolytes in the flow cell.

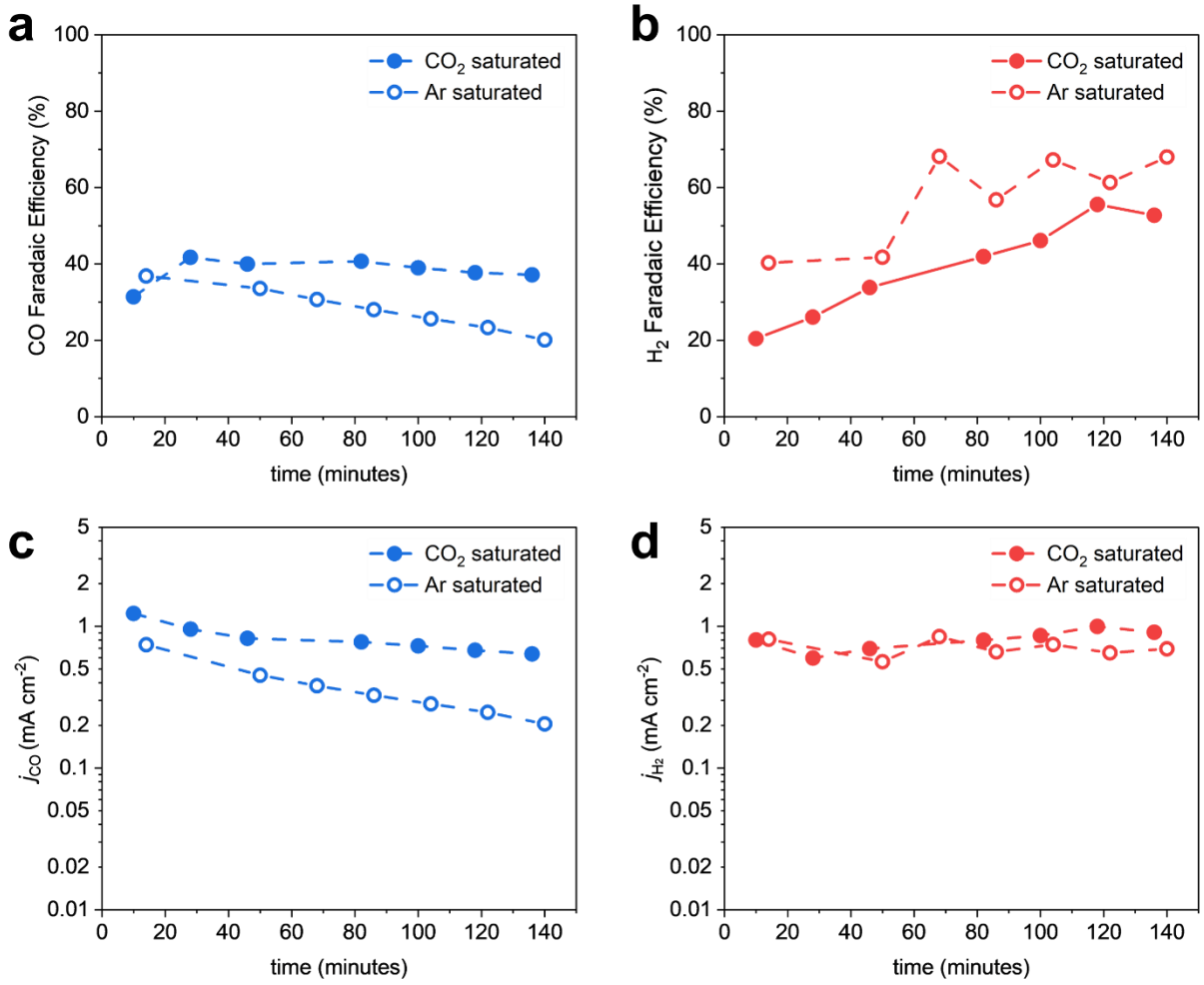

Figure S14. Representative example of time dependence of detected CO and H_2 over a >2 hour test (Ni-N-C/carbon paper, -1.1 V vs. SHE, 1 M DEA/1 M $NaClO_4$) in the flow cell under pure CO_2 or Ar flow, showing Faradaic efficiencies of a) CO, and b) H_2, and corresponding partial current densities of c) CO and d) H_2. In this test, the pH shifted from ~7.3 to ~7.8 and the CO_2 concentration in the headspace shifted from ~5% to ~3% under Ar flow.

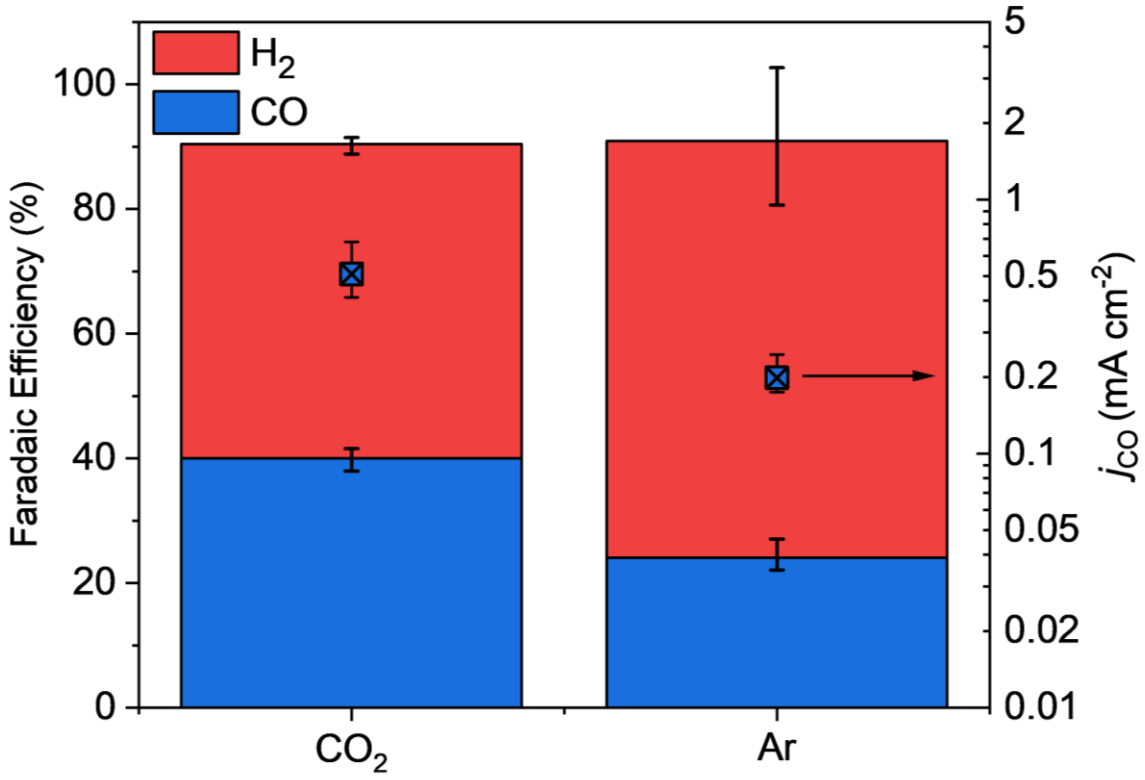

Figure S15. Average Faradaic efficiencies (bars, left-axis) and average partial current densities (squares, right-axis) of three additional parallel tests with Ni-N-C/carbon paper in a flow cell with pure CO_2 and pure Ar gas in 1 M DEA/1 M $NaClO_4$ electrolyte. All tests were held at a constant potential of -1.1 V vs. SHE and the Ar saturated tests were held for at least 2 hours. The same electrode was first measured under the pure CO_2 before switching to pure Ar.

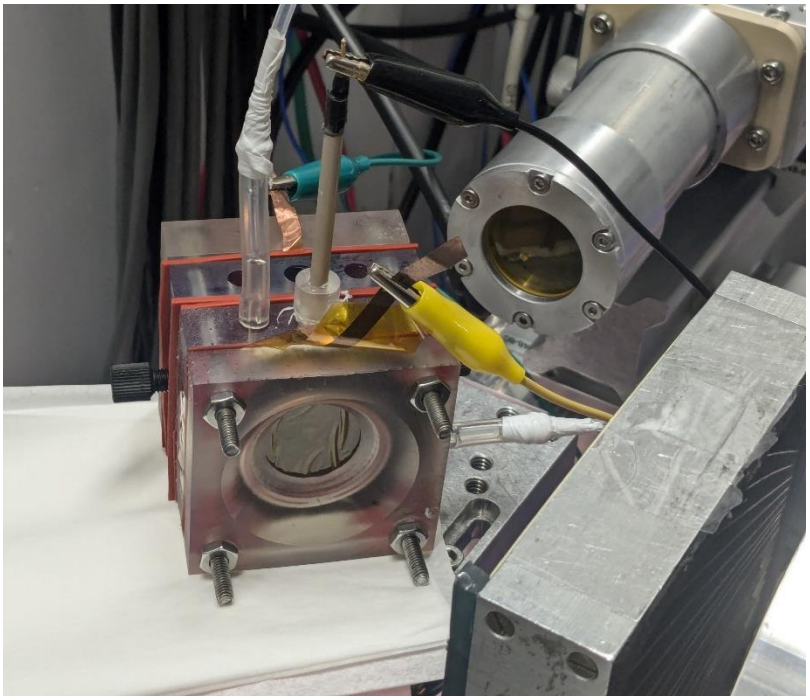

Figure S16. Photo of assembled *in situ* XAS cell at SSRL.

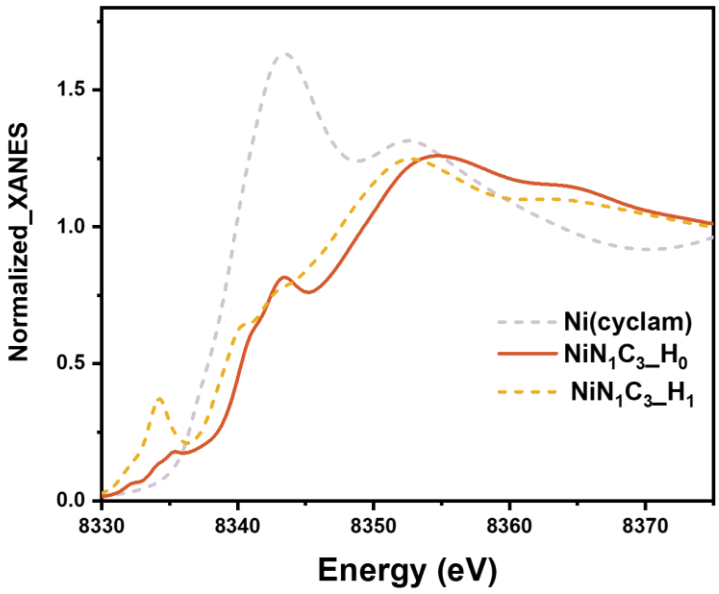

Figure S17. Simulated XANES spectra of NiN_1C_3 with (NiN_1C_3_H_1) and without (NiN_1C_3_H_0) absorbed hydrogen on the coordinating carbon, with the simulated spectrum of Ni(cyclam) shown for comparison.

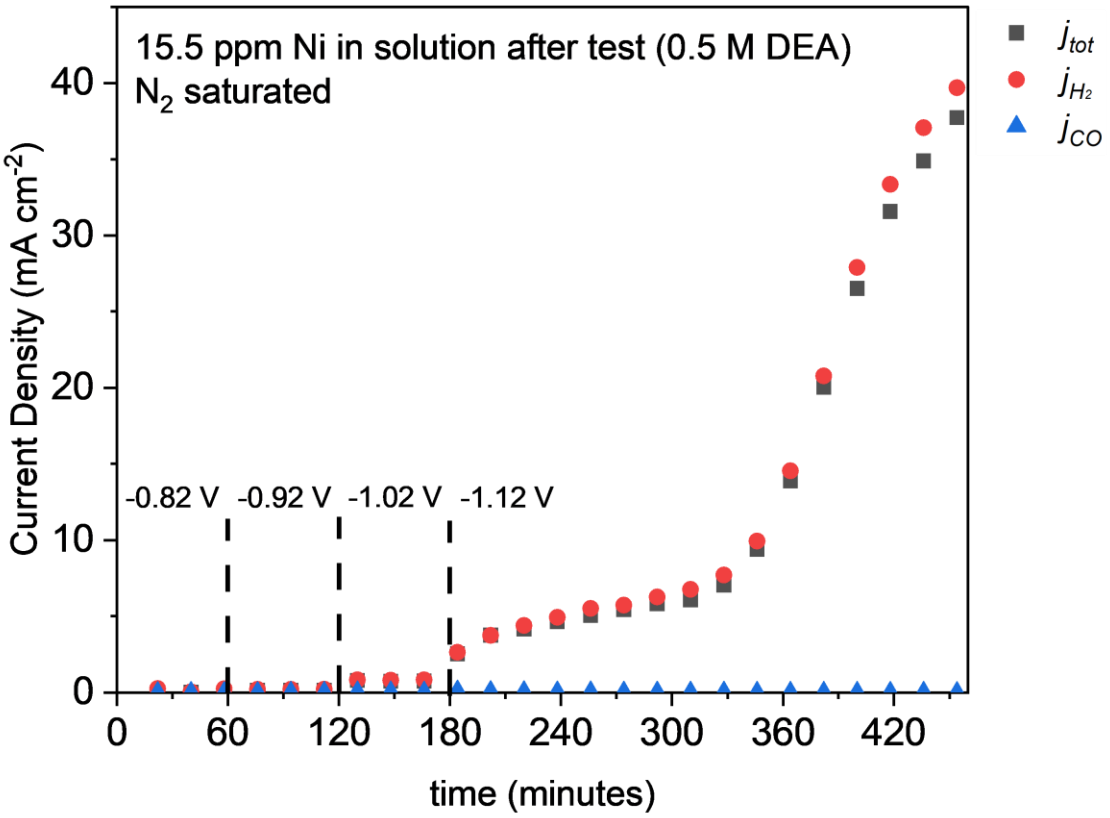

Figure S18. Representative long-term test of Ni-N-C catalyst in 0.5 M DEA/0.5 $NaClO_4$ under inert-gas saturation with resulting Ni leaching measured by ICP-MS (15.5 ppm).

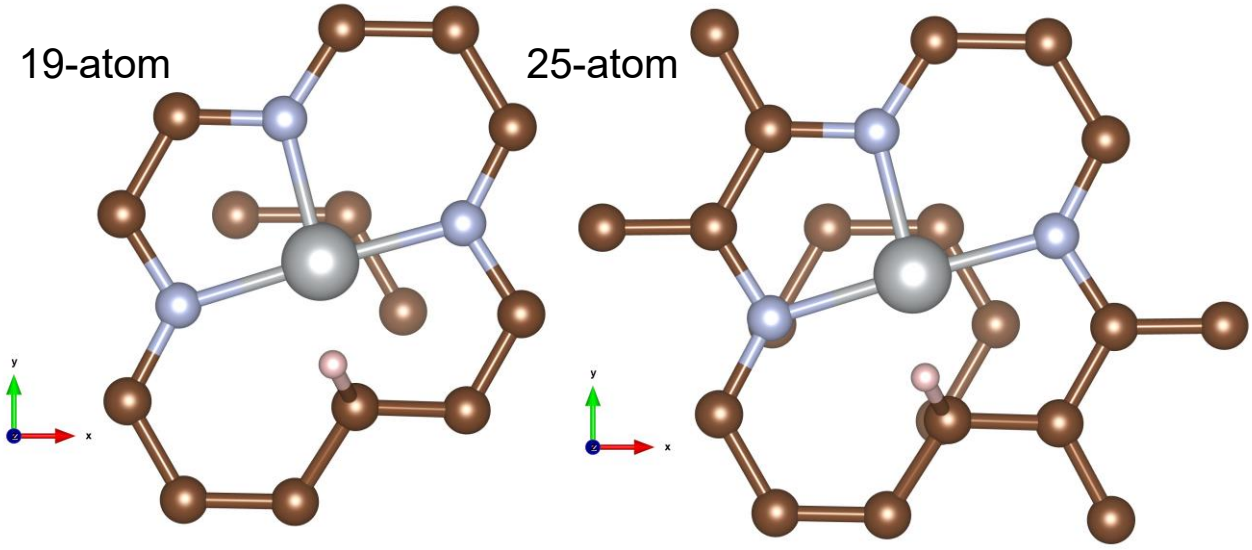

Figure S19. The two fragment sizes used for quantum embedding calculations on spin gaps to test the validity of DFT. All electrons for the 19-atom (left) and 25-atom (right) fragments were treated at the correlated post-HF levels of CASPT2(6,6) and CCSD(T), while their periodic surroundings were frozen at the mean-field level (HF). Carbon atoms are shown in brown, nitrogen in light blue, nickel in silver, and hydrogen in light pink.

Optimized POSCAR for NiN_3C_1

CNNi

1.0

12.3386201859 0.0000000000 0.0000000000

-6.1693115158 10.6855577071 0.0000000000

0.0000000000 0.0000000000 26.0551109314

C N Ni

145 3 1

Direct

0.000000000 0.000000000 0.083329998

0.533330023 0.066670001 0.083329998

0.733330011 0.066670001 0.083329998

0.933329999 0.066670001 0.083329998

0.333330005 0.066670001 0.083329998

0.133330002 0.066670001 0.083329998

0.600000024 0.200000003 0.083329998

0.800000012 0.200000003 0.083329998

0.200000003 0.200000003 0.083329998

0.400000006 0.200000003 0.083329998

0.000000000 0.200000003 0.083329998

0.133330002 0.266669989 0.083329998

0.733330011 0.266669989 0.083329998

0.933329999 0.266669989 0.083329998

0.333330005 0.266669989 0.083329998

0.533330023 0.266669989 0.083329998

0.000000000 0.400000006 0.083329998

0.600000024 0.400000006 0.083329998

0.800000012 0.400000006 0.083329998

0.200000003 0.400000006 0.083329998

0.400000006	0.400000006	0.083329998
0.133330002	0.466670007	0.083329998
0.733330011	0.466670007	0.083329998
0.933329999	0.466670007	0.083329998
0.333330005	0.466670007	0.083329998
0.533330023	0.466670007	0.083329998
0.000000000	0.600000024	0.083329998
0.400000006	0.600000024	0.083329998
0.800000012	0.600000024	0.083329998
0.600000024	0.600000024	0.083329998
0.200000003	0.600000024	0.083329998
0.133330002	0.666670024	0.083329998
0.933329999	0.666670024	0.083329998
0.533330023	0.666670024	0.083329998
0.733330011	0.666670024	0.083329998
0.333330005	0.666670024	0.083329998
0.400000006	0.800000012	0.083329998
0.600000024	0.800000012	0.083329998
0.000000000	0.800000012	0.083329998
0.800000012	0.800000012	0.083329998
0.200000003	0.800000012	0.083329998
0.133330002	0.866670012	0.083329998
0.933329999	0.866670012	0.083329998
0.533330023	0.866670012	0.083329998
0.733330011	0.866670012	0.083329998
0.333330005	0.866670012	0.083329998
0.200000003	0.000000000	0.083329998
0.400000006	0.000000000	0.083329998
0.600000024	0.000000000	0.083329998
0.800000012	0.000000000	0.083329998

0.000000000	0.000000000	0.250000000
0.200000003	0.000000000	0.250000000
0.066670001	0.133330002	0.250000000
0.266669989	0.133330002	0.250000000
0.466670007	0.133330002	0.250000000
0.666670024	0.133330002	0.250000000
0.866670012	0.133330002	0.250000000
0.600000024	0.200000003	0.250000000
0.800000012	0.200000003	0.250000000
0.200000003	0.200000003	0.250000000
0.400000006	0.200000003	0.250000000
0.000000000	0.200000003	0.250000000
0.666670024	0.333330005	0.250000000
0.866670012	0.333330005	0.250000000
0.266669989	0.333330005	0.250000000
0.466670007	0.333330005	0.250000000
0.066670001	0.333330005	0.250000000
0.000000000	0.400000006	0.250000000
0.600000024	0.400000006	0.250000000
0.800000012	0.400000006	0.250000000
0.200000003	0.400000006	0.250000000
0.400000006	0.400000006	0.250000000
0.066670001	0.533330023	0.250000000
0.666670024	0.533330023	0.250000000
0.866670012	0.533330023	0.250000000
0.266669989	0.533330023	0.250000000
0.466670007	0.533330023	0.250000000
0.400000006	0.600000024	0.250000000
0.000000000	0.600000024	0.250000000
0.600000024	0.600000024	0.250000000

0.800000012	0.600000024	0.250000000
0.200000003	0.600000024	0.250000000
0.066670001	0.733330011	0.250000000
0.866670012	0.733330011	0.250000000
0.466670007	0.733330011	0.250000000
0.666670024	0.733330011	0.250000000
0.266669989	0.733330011	0.250000000
0.400000006	0.800000012	0.250000000
0.600000024	0.800000012	0.250000000
0.000000000	0.800000012	0.250000000
0.800000012	0.800000012	0.250000000
0.200000003	0.800000012	0.250000000
0.266669989	0.933329999	0.250000000
0.066670001	0.933329999	0.250000000
0.466670007	0.933329999	0.250000000
0.666670024	0.933329999	0.250000000
0.866670012	0.933329999	0.250000000
0.400000006	0.000000000	0.250000000
0.600000024	0.000000000	0.250000000
0.800000012	0.000000000	0.250000000
0.732029974	0.852779984	0.385329992
0.205840006	0.999949992	0.384640008
0.404949993	0.000260000	0.384420007
0.735819995	0.058820002	0.385690004
0.934010029	0.058580000	0.384849995
0.137679994	0.064570002	0.384440005
0.537859976	0.064549997	0.385039985
0.339859992	0.069810003	0.384440005
0.605229974	0.198880002	0.385529995
0.204559997	0.199120000	0.383529991

0.407160014	0.204339996	0.384330004
0.339560002	0.271739990	0.383659989
0.542020023	0.270960003	0.385100007
0.612519979	0.404060006	0.385320008
0.801190019	0.786660016	0.385490000
0.596650004	0.787249982	0.384820014
0.936399996	0.860260010	0.385529995
0.534950018	0.860520005	0.384559989
0.799759984	0.988319993	0.385439992
0.602859974	0.994660020	0.385280013
0.002620000	0.994740009	0.384889990
0.001100000	0.192939997	0.383899987
0.802860022	0.193090007	0.385459989
0.935790002	0.260349989	0.384119987
0.134519994	0.261869997	0.382889986
0.738229990	0.262010008	0.385829985
0.743579984	0.464260012	0.385890007
0.332729995	0.462280005	0.382200003
0.811429977	0.598919988	0.385850012
0.399710000	0.597710013	0.382569999
0.006950000	0.798129976	0.385560006
0.402200013	0.797439992	0.383340001
0.139630005	0.866209984	0.384869993
0.337720007	0.866190016	0.383700013
0.003460000	0.394389987	0.383219987
0.807160020	0.395779997	0.385780007
0.200949997	0.395579994	0.381940007
0.135590002	0.462740004	0.381929994
0.939639986	0.462700009	0.384550005
0.006380000	0.596369982	0.384519994

0.202010006 0.596130013 0.381980002
0.942229986 0.665030003 0.385710001
0.334320009 0.663709998 0.382259995
0.138150007 0.664279997 0.383249998
0.204740003 0.798590004 0.383890003
0.400840014 0.401930004 0.383280009
0.527279973 0.658429980 0.384070009
0.742020011 0.657140017 0.385600001
0.569509983 0.527899981 0.384330004

Optimized POSCAR of $NaRCO_2$ adsorbed on NiN_3C_1

HCNONaNi
1.0
12.3386201859 0.0000000000 0.0000000000
-6.1693115158 10.6855577071 0.0000000000
0.0000000000 0.0000000000 26.0551109314
H C N O Na Ni
10 150 4 4 1 1
Direct
0.608449996 0.372880012 0.537760019
0.800379992 0.724520028 0.548399985
0.429949999 0.369029999 0.583790004
0.645959973 0.736109972 0.609179974
0.869960010 0.884230018 0.609239995
0.703270018 0.430559993 0.593879998
0.827759981 0.637000024 0.596010029
0.522899985 0.426660001 0.640810013
0.659720004 0.628189981 0.650520027
0.563210011 0.245220006 0.633270025
0.000000000 0.000000000 0.083329998

0.133330002	0.066670001	0.083329998
0.533330023	0.066670001	0.083329998
0.733330011	0.066670001	0.083329998
0.933329999	0.066670001	0.083329998
0.333330005	0.066670001	0.083329998
0.800000012	0.200000003	0.083329998
0.200000003	0.200000003	0.083329998
0.400000006	0.200000003	0.083329998
0.000000000	0.200000003	0.083329998
0.600000024	0.200000003	0.083329998
0.133330002	0.266669989	0.083329998
0.733330011	0.266669989	0.083329998
0.933329999	0.266669989	0.083329998
0.333330005	0.266669989	0.083329998
0.533330023	0.266669989	0.083329998
0.000000000	0.400000006	0.083329998
0.600000024	0.400000006	0.083329998
0.800000012	0.400000006	0.083329998
0.200000003	0.400000006	0.083329998
0.400000006	0.400000006	0.083329998
0.133330002	0.466670007	0.083329998
0.733330011	0.466670007	0.083329998
0.933329999	0.466670007	0.083329998
0.333330005	0.466670007	0.083329998
0.533330023	0.466670007	0.083329998
0.000000000	0.600000024	0.083329998
0.400000006	0.600000024	0.083329998
0.800000012	0.600000024	0.083329998
0.600000024	0.600000024	0.083329998
0.200000003	0.600000024	0.083329998

0.133330002	0.666670024	0.083329998
0.933329999	0.666670024	0.083329998
0.533330023	0.666670024	0.083329998
0.733330011	0.666670024	0.083329998
0.333330005	0.666670024	0.083329998
0.400000006	0.800000012	0.083329998
0.600000024	0.800000012	0.083329998
0.000000000	0.800000012	0.083329998
0.800000012	0.800000012	0.083329998
0.200000003	0.800000012	0.083329998
0.133330002	0.866670012	0.083329998
0.933329999	0.866670012	0.083329998
0.533330023	0.866670012	0.083329998
0.733330011	0.866670012	0.083329998
0.333330005	0.866670012	0.083329998
0.200000003	0.000000000	0.083329998
0.400000006	0.000000000	0.083329998
0.600000024	0.000000000	0.083329998
0.800000012	0.000000000	0.083329998
0.000000000	0.000000000	0.250000000
0.066670001	0.133330002	0.250000000
0.266669989	0.133330002	0.250000000
0.466670007	0.133330002	0.250000000
0.666670024	0.133330002	0.250000000
0.866670012	0.133330002	0.250000000
0.600000024	0.200000003	0.250000000
0.800000012	0.200000003	0.250000000
0.200000003	0.200000003	0.250000000
0.400000006	0.200000003	0.250000000
0.000000000	0.200000003	0.250000000

0.666670024	0.333330005	0.250000000
0.866670012	0.333330005	0.250000000
0.266669989	0.333330005	0.250000000
0.466670007	0.333330005	0.250000000
0.066670001	0.333330005	0.250000000
0.000000000	0.400000006	0.250000000
0.600000024	0.400000006	0.250000000
0.800000012	0.400000006	0.250000000
0.200000003	0.400000006	0.250000000
0.400000006	0.400000006	0.250000000
0.066670001	0.533330023	0.250000000
0.666670024	0.533330023	0.250000000
0.866670012	0.533330023	0.250000000
0.266669989	0.533330023	0.250000000
0.466670007	0.533330023	0.250000000
0.400000006	0.600000024	0.250000000
0.000000000	0.600000024	0.250000000
0.600000024	0.600000024	0.250000000
0.800000012	0.600000024	0.250000000
0.200000003	0.600000024	0.250000000
0.066670001	0.733330011	0.250000000
0.866670012	0.733330011	0.250000000
0.466670007	0.733330011	0.250000000
0.666670024	0.733330011	0.250000000
0.266669989	0.733330011	0.250000000
0.400000006	0.800000012	0.250000000
0.600000024	0.800000012	0.250000000
0.000000000	0.800000012	0.250000000
0.800000012	0.800000012	0.250000000
0.200000003	0.800000012	0.250000000

0.266669989	0.933329999	0.250000000
0.066670001	0.933329999	0.250000000
0.466670007	0.933329999	0.250000000
0.666670024	0.933329999	0.250000000
0.866670012	0.933329999	0.250000000
0.600000024	0.000000000	0.250000000
0.200000003	0.000000000	0.250000000
0.800000012	0.000000000	0.250000000
0.400000006	0.000000000	0.250000000
0.329950005	0.670620024	0.381320000
0.999090016	0.401470006	0.381839991
0.802670002	0.402590007	0.383089989
0.131270006	0.469639987	0.381289989
0.935140014	0.469650000	0.382239997
0.395200014	0.604449987	0.381199986
0.197630003	0.603079975	0.381179988
0.001840000	0.603200018	0.381810009
0.133690000	0.671159983	0.381309986
0.397890002	0.804270029	0.381790012
0.798510015	0.199890003	0.382860005
0.931460023	0.267329991	0.382360011
0.733919978	0.268900007	0.383150011
0.196360007	0.402170002	0.381440014
0.739030004	0.470840007	0.383469999
0.200450003	0.805390000	0.381419986
0.530610025	0.867190003	0.382319987
0.333429992	0.873000026	0.381859988
0.598389983	0.001400000	0.382889986
0.400530010	0.007030000	0.382470012
0.731329978	0.065569997	0.382979989

0.533500016	0.071390003	0.382959992
0.600870013	0.205880001	0.383219987
0.328099996	0.468840003	0.381320000
0.937590003	0.671729982	0.382279992
0.201389998	0.006840000	0.382180005
0.335390002	0.076640002	0.382470012
0.996609986	0.199699998	0.382400006
0.129960001	0.268500000	0.381999999
0.537400007	0.277830005	0.383150011
0.607940018	0.410840005	0.383329988
0.806879997	0.605449975	0.383069992
0.591989994	0.793720007	0.382099986
0.002310000	0.804840028	0.382099986
0.135220006	0.873059988	0.381770015
0.795210004	0.994960010	0.382900000
0.998049974	0.001270000	0.382569999
0.929600000	0.065300003	0.382750005
0.133100003	0.071220003	0.382330000
0.199959993	0.205789998	0.382120013
0.402469993	0.211109996	0.382600009
0.727320015	0.859239995	0.382719994
0.931590021	0.866770029	0.382649988
0.334870011	0.278499991	0.382050008
0.796400011	0.793079972	0.382889986
0.499300003	0.579140007	0.542569995
0.606029987	0.373389989	0.579990029
0.525510013	0.428570002	0.598280013
0.798330009	0.706889987	0.590049982
0.664919972	0.657989979	0.610140026
0.522669971	0.665130019	0.381370008

0.396160007 0.408699989 0.381630003
0.737429976 0.663619995 0.383139998
0.568809986 0.555180013 0.580380023
0.406480014 0.484499991 0.522180021
0.537150025 0.693889976 0.532750010
0.555100024 0.245490000 0.596029997
0.888360023 0.817610025 0.616840005
0.099720001 0.773850024 0.520039976
0.564809978 0.534650028 0.382209986

Optimized POSCAR of NaRCOOH adsorbed on NiN_3C_1

NaRCOOH
1.0
12.3386001587 0.0000000000 0.0000000000
-6.1693000793 10.6855411846 0.0000000000
0.0000000000 0.0000000000 26.0550994873
H C N O Na Ni
11 150 4 4 1 1
Direct
0.616800010 0.509819984 0.460189998
0.843890011 0.742500007 0.549300015
0.535700023 0.746510029 0.552070022
0.730790019 0.520129979 0.579460025
0.353390008 0.692049980 0.594860017
0.414000005 0.529590011 0.594860017
0.804989994 0.790989995 0.607630014
0.615040004 0.803759992 0.611790001
0.691619992 0.566929996 0.637769997
0.526719987 0.589829981 0.645250022
0.925360024 0.722660005 0.649349988
0.000000000 0.000000000 0.083329998

0.333330005	0.066670001	0.083329998
0.133330002	0.066670001	0.083329998
0.533330023	0.066670001	0.083329998
0.733330011	0.066670001	0.083329998
0.933329999	0.066670001	0.083329998
0.800000012	0.200000003	0.083329998
0.200000003	0.200000003	0.083329998
0.400000006	0.200000003	0.083329998
0.000000000	0.200000003	0.083329998
0.600000024	0.200000003	0.083329998
0.133330002	0.266669989	0.083329998
0.733330011	0.266669989	0.083329998
0.933329999	0.266669989	0.083329998
0.333330005	0.266669989	0.083329998
0.533330023	0.266669989	0.083329998
0.000000000	0.400000006	0.083329998
0.600000024	0.400000006	0.083329998
0.800000012	0.400000006	0.083329998
0.200000003	0.400000006	0.083329998
0.400000006	0.400000006	0.083329998
0.133330002	0.466670007	0.083329998
0.733330011	0.466670007	0.083329998
0.933329999	0.466670007	0.083329998
0.333330005	0.466670007	0.083329998
0.533330023	0.466670007	0.083329998
0.000000000	0.600000024	0.083329998
0.400000006	0.600000024	0.083329998
0.800000012	0.600000024	0.083329998
0.600000024	0.600000024	0.083329998
0.200000003	0.600000024	0.083329998

0.133330002	0.666670024	0.083329998
0.933329999	0.666670024	0.083329998
0.533330023	0.666670024	0.083329998
0.733330011	0.666670024	0.083329998
0.333330005	0.666670024	0.083329998
0.400000006	0.800000012	0.083329998
0.600000024	0.800000012	0.083329998
0.000000000	0.800000012	0.083329998
0.800000012	0.800000012	0.083329998
0.200000003	0.800000012	0.083329998
0.133330002	0.866670012	0.083329998
0.933329999	0.866670012	0.083329998
0.533330023	0.866670012	0.083329998
0.733330011	0.866670012	0.083329998
0.333330005	0.866670012	0.083329998
0.200000003	0.000000000	0.083329998
0.400000006	0.000000000	0.083329998
0.600000024	0.000000000	0.083329998
0.800000012	0.000000000	0.083329998
0.000000000	0.000000000	0.250000000
0.200000003	0.000000000	0.250000000
0.066670001	0.133330002	0.250000000
0.266669989	0.133330002	0.250000000
0.466670007	0.133330002	0.250000000
0.666670024	0.133330002	0.250000000
0.866670012	0.133330002	0.250000000
0.600000024	0.200000003	0.250000000
0.800000012	0.200000003	0.250000000
0.200000003	0.200000003	0.250000000
0.400000006	0.200000003	0.250000000

0.000000000	0.200000003	0.250000000
0.666670024	0.333330005	0.250000000
0.866670012	0.333330005	0.250000000
0.266669989	0.333330005	0.250000000
0.466670007	0.333330005	0.250000000
0.066670001	0.333330005	0.250000000
0.000000000	0.400000006	0.250000000
0.600000024	0.400000006	0.250000000
0.800000012	0.400000006	0.250000000
0.200000003	0.400000006	0.250000000
0.400000006	0.400000006	0.250000000
0.066670001	0.533330023	0.250000000
0.666670024	0.533330023	0.250000000
0.866670012	0.533330023	0.250000000
0.266669989	0.533330023	0.250000000
0.466670007	0.533330023	0.250000000
0.400000006	0.600000024	0.250000000
0.000000000	0.600000024	0.250000000
0.600000024	0.600000024	0.250000000
0.800000012	0.600000024	0.250000000
0.200000003	0.600000024	0.250000000
0.066670001	0.733330011	0.250000000
0.866670012	0.733330011	0.250000000
0.466670007	0.733330011	0.250000000
0.666670024	0.733330011	0.250000000
0.266669989	0.733330011	0.250000000
0.400000006	0.800000012	0.250000000
0.600000024	0.800000012	0.250000000
0.000000000	0.800000012	0.250000000
0.800000012	0.800000012	0.250000000

0.200000003	0.800000012	0.250000000
0.866670012	0.933329999	0.250000000
0.266669989	0.933329999	0.250000000
0.066670001	0.933329999	0.250000000
0.466670007	0.933329999	0.250000000
0.666670024	0.933329999	0.250000000
0.600000024	0.000000000	0.250000000
0.800000012	0.000000000	0.250000000
0.400000006	0.000000000	0.250000000
0.611679971	0.415080011	0.381460011
0.743619978	0.475569993	0.380980015
0.811029971	0.609250009	0.380620003
0.604709983	0.210109994	0.381229997
0.737909973	0.273299992	0.381119996
0.541329980	0.282339990	0.381639987
0.806940019	0.407180011	0.381170005
0.941330016	0.675620019	0.381269991
0.404130012	0.010780000	0.381520003
0.537490010	0.075460002	0.380899996
0.339170009	0.080389999	0.381870002
0.939599991	0.474159986	0.381350011
0.005980000	0.607240021	0.381559998
0.800149977	0.797290027	0.380400002
0.006160000	0.808979988	0.381370008
0.204050004	0.809080005	0.381909996
0.935540020	0.870869994	0.381000012
0.139060006	0.876789987	0.381850004
0.002200000	0.005570000	0.381179988
0.602249980	0.005590000	0.380380005
0.205270007	0.010510000	0.381870002

0.735849977	0.070370004	0.380569994
0.802760005	0.204429999	0.380939990
0.406049997	0.214949995	0.381660014
0.935949981	0.272119999	0.380970001
0.003230000	0.405490011	0.381139994
0.137989998	0.675790012	0.381650001
0.337339997	0.876929998	0.381599993
0.799589992	0.999899983	0.380580008
0.934029996	0.069969997	0.380939990
0.137170002	0.075240001	0.381520003
0.001270000	0.204410002	0.380989999
0.135590002	0.474159986	0.380899996
0.201670006	0.607270002	0.381060004
0.401849985	0.808359981	0.380879998
0.731580019	0.863839984	0.380290002
0.134509996	0.272940010	0.380910009
0.334120005	0.674470007	0.380560011
0.534759998	0.871439993	0.380329996
0.204380006	0.209979996	0.381159991
0.339459985	0.282499999	0.380939990
0.201110005	0.406899989	0.380549997
0.596289992	0.797800004	0.379909992
0.332670003	0.473839998	0.379949987
0.398730010	0.607819974	0.379790008
0.562359989	0.543020010	0.523840010
0.824169993	0.720510006	0.590340018
0.528330028	0.730589986	0.593930006
0.709999979	0.589020014	0.596639991
0.510930002	0.600319982	0.604510009
0.740849972	0.667680025	0.380149990

0.401369989 0.413109988 0.379949987
0.527620018 0.669160008 0.379660010
0.595499992 0.575510025 0.573870003
0.647239983 0.526459992 0.496760011
0.464170009 0.529120028 0.504760027
0.934490025 0.728089988 0.612070024
0.428460002 0.744029999 0.615100026
0.613420010 0.038600001 0.518710017
0.569350004 0.539409995 0.380180001

Optimized POSCAR of NaRCO adsorbed on NiN_3C_1

NaRCO
1.0
12.3386201859 0.0000000000 0.0000000000
-6.1693115158 10.6855577071 0.0000000000
0.0000000000 0.0000000000 26.0551109314
H C N O Na Ni
10 150 4 3 1 1
Direct
0.738629997 0.502860010 0.470340014
0.905470014 0.724120021 0.477310002
0.632099986 0.785279989 0.518980026
0.737089992 0.484840006 0.538030028
0.894590020 0.719070017 0.545499980
0.780210018 0.833440006 0.547890007
0.967750013 0.581170022 0.544219971
0.544030011 0.583859980 0.573029995
0.701860011 0.628260016 0.588320017
0.557969987 0.783379972 0.600549996
0.000000000 0.000000000 0.083329998
0.333330005 0.066670001 0.083329998

0.133330002	0.066670001	0.083329998
0.533330023	0.066670001	0.083329998
0.733330011	0.066670001	0.083329998
0.933329999	0.066670001	0.083329998
0.000000000	0.200000003	0.083329998
0.600000024	0.200000003	0.083329998
0.800000012	0.200000003	0.083329998
0.200000003	0.200000003	0.083329998
0.400000006	0.200000003	0.083329998
0.133330002	0.266669989	0.083329998
0.733330011	0.266669989	0.083329998
0.933329999	0.266669989	0.083329998
0.333330005	0.266669989	0.083329998
0.533330023	0.266669989	0.083329998
0.000000000	0.400000006	0.083329998
0.600000024	0.400000006	0.083329998
0.800000012	0.400000006	0.083329998
0.200000003	0.400000006	0.083329998
0.400000006	0.400000006	0.083329998
0.133330002	0.466670007	0.083329998
0.733330011	0.466670007	0.083329998
0.933329999	0.466670007	0.083329998
0.333330005	0.466670007	0.083329998
0.533330023	0.466670007	0.083329998
0.000000000	0.600000024	0.083329998
0.400000006	0.600000024	0.083329998
0.800000012	0.600000024	0.083329998
0.600000024	0.600000024	0.083329998
0.200000003	0.600000024	0.083329998
0.133330002	0.666670024	0.083329998

0.933329999	0.666670024	0.083329998
0.533330023	0.666670024	0.083329998
0.733330011	0.666670024	0.083329998
0.333330005	0.666670024	0.083329998
0.400000006	0.800000012	0.083329998
0.600000024	0.800000012	0.083329998
0.000000000	0.800000012	0.083329998
0.800000012	0.800000012	0.083329998
0.200000003	0.800000012	0.083329998
0.133330002	0.866670012	0.083329998
0.933329999	0.866670012	0.083329998
0.533330023	0.866670012	0.083329998
0.733330011	0.866670012	0.083329998
0.333330005	0.866670012	0.083329998
0.200000003	0.000000000	0.083329998
0.400000006	0.000000000	0.083329998
0.600000024	0.000000000	0.083329998
0.800000012	0.000000000	0.083329998
0.000000000	0.000000000	0.250000000
0.200000003	0.000000000	0.250000000
0.066670001	0.133330002	0.250000000
0.266669989	0.133330002	0.250000000
0.466670007	0.133330002	0.250000000
0.666670024	0.133330002	0.250000000
0.866670012	0.133330002	0.250000000
0.600000024	0.200000003	0.250000000
0.800000012	0.200000003	0.250000000
0.200000003	0.200000003	0.250000000
0.400000006	0.200000003	0.250000000
0.000000000	0.200000003	0.250000000

0.666670024	0.333330005	0.250000000
0.866670012	0.333330005	0.250000000
0.266669989	0.333330005	0.250000000
0.466670007	0.333330005	0.250000000
0.066670001	0.333330005	0.250000000
0.000000000	0.400000006	0.250000000
0.600000024	0.400000006	0.250000000
0.800000012	0.400000006	0.250000000
0.200000003	0.400000006	0.250000000
0.400000006	0.400000006	0.250000000
0.066670001	0.533330023	0.250000000
0.666670024	0.533330023	0.250000000
0.866670012	0.533330023	0.250000000
0.266669989	0.533330023	0.250000000
0.466670007	0.533330023	0.250000000
0.400000006	0.600000024	0.250000000
0.000000000	0.600000024	0.250000000
0.600000024	0.600000024	0.250000000
0.800000012	0.600000024	0.250000000
0.200000003	0.600000024	0.250000000
0.066670001	0.733330011	0.250000000
0.866670012	0.733330011	0.250000000
0.466670007	0.733330011	0.250000000
0.666670024	0.733330011	0.250000000
0.266669989	0.733330011	0.250000000
0.400000006	0.800000012	0.250000000
0.600000024	0.800000012	0.250000000
0.000000000	0.800000012	0.250000000
0.800000012	0.800000012	0.250000000
0.200000003	0.800000012	0.250000000

0.866670012	0.933329999	0.250000000
0.266669989	0.933329999	0.250000000
0.066670001	0.933329999	0.250000000
0.466670007	0.933329999	0.250000000
0.666670024	0.933329999	0.250000000
0.400000006	0.000000000	0.250000000
0.600000024	0.000000000	0.250000000
0.800000012	0.000000000	0.250000000
0.750119984	0.471120000	0.380129993
0.813600004	0.402539998	0.378390014
0.946340024	0.469509989	0.377119988
0.012970000	0.602639973	0.376870006
0.817879975	0.605009973	0.379110008
0.010160000	0.400920004	0.377539992
0.145060003	0.670949996	0.377290010
0.948599994	0.671060026	0.377499998
0.942889988	0.267520010	0.378560007
0.744960010	0.268759996	0.379610002
0.618879974	0.410039991	0.385749996
0.142719999	0.469440013	0.377629995
0.209030002	0.602569997	0.377490014
0.013360000	0.804109991	0.378589988
0.809809983	0.199910000	0.379119992
0.611790001	0.205540001	0.381249994
0.211180001	0.804270029	0.378410012
0.146249995	0.871940017	0.379009992
0.008280000	0.199729994	0.379509985
0.208360001	0.402229995	0.378520012
0.943050027	0.866400003	0.380140007
0.344529986	0.872030020	0.379469991

0.009480000	0.001050000	0.380409986
0.411390007	0.005950000	0.380789995
0.941200018	0.065420002	0.380499989
0.544659972	0.070809998	0.380780011
0.141570002	0.268249989	0.379530013
0.548219979	0.277240008	0.383980006
0.341569990	0.669730008	0.378399998
0.609480023	0.001060000	0.380320013
0.212329999	0.005650000	0.380430013
0.742919981	0.065729998	0.380070001
0.144229993	0.070469998	0.380530000
0.346179992	0.075360000	0.381700009
0.808109999	0.793179989	0.381819993
0.409099996	0.803489983	0.379379988
0.806750000	0.995369971	0.381020010
0.211160004	0.204929993	0.380710006
0.412900001	0.209810004	0.383619994
0.340229988	0.468870014	0.379559994
0.739009976	0.859549999	0.382450014
0.541999996	0.866850019	0.380389988
0.406760007	0.603340030	0.379689991
0.345950007	0.277200013	0.382299989
0.603690028	0.793420017	0.381900012
0.560249984	0.551400006	0.474539995
0.750599980	0.551580012	0.506879985
0.884150028	0.662800014	0.510909975
0.678409994	0.775370002	0.553449988
0.641669989	0.637619972	0.559629977
0.749170005	0.664040029	0.382380009
0.407350004	0.407029986	0.382250011

0.535030007 0.665199995 0.382640004
0.653680027 0.585590005 0.510580003
0.464899987 0.556190014 0.486860007
0.974420011 0.621940017 0.511349976
0.648940027 0.823989987 0.598089993
0.797510028 0.136260003 0.516369998
0.576479971 0.534300029 0.393049985

Optimized POSCAR of $NaCO_2$ adsorbed on NiN_3C_1

NaCO2
1.0
12.3386201859 0.0000000000 0.0000000000
-6.1693115158 10.6855577071 0.0000000000
0.0000000000 0.0000000000 26.0551109314
C N O Na Ni
146 3 2 1 1
Direct
0.000000000 0.000000000 0.083329998
0.533330023 0.066670001 0.083329998
0.733330011 0.066670001 0.083329998
0.933329999 0.066670001 0.083329998
0.333330005 0.066670001 0.083329998
0.133330002 0.066670001 0.083329998
0.800000012 0.200000003 0.083329998
0.200000003 0.200000003 0.083329998
0.400000006 0.200000003 0.083329998
0.000000000 0.200000003 0.083329998
0.600000024 0.200000003 0.083329998
0.133330002 0.266669989 0.083329998
0.733330011 0.266669989 0.083329998
0.933329999 0.266669989 0.083329998

0.333330005	0.266669989	0.083329998
0.533330023	0.266669989	0.083329998
0.000000000	0.400000006	0.083329998
0.600000024	0.400000006	0.083329998
0.800000012	0.400000006	0.083329998
0.200000003	0.400000006	0.083329998
0.400000006	0.400000006	0.083329998
0.133330002	0.466670007	0.083329998
0.733330011	0.466670007	0.083329998
0.933329999	0.466670007	0.083329998
0.333330005	0.466670007	0.083329998
0.533330023	0.466670007	0.083329998
0.000000000	0.600000024	0.083329998
0.400000006	0.600000024	0.083329998
0.800000012	0.600000024	0.083329998
0.600000024	0.600000024	0.083329998
0.200000003	0.600000024	0.083329998
0.133330002	0.666670024	0.083329998
0.933329999	0.666670024	0.083329998
0.533330023	0.666670024	0.083329998
0.733330011	0.666670024	0.083329998
0.333330005	0.666670024	0.083329998
0.400000006	0.800000012	0.083329998
0.600000024	0.800000012	0.083329998
0.000000000	0.800000012	0.083329998
0.800000012	0.800000012	0.083329998
0.200000003	0.800000012	0.083329998
0.133330002	0.866670012	0.083329998
0.933329999	0.866670012	0.083329998
0.533330023	0.866670012	0.083329998

0.733330011	0.866670012	0.083329998
0.333330005	0.866670012	0.083329998
0.200000003	0.000000000	0.083329998
0.400000006	0.000000000	0.083329998
0.600000024	0.000000000	0.083329998
0.800000012	0.000000000	0.083329998
0.000000000	0.000000000	0.250000000
0.066670001	0.133330002	0.250000000
0.266669989	0.133330002	0.250000000
0.466670007	0.133330002	0.250000000
0.666670024	0.133330002	0.250000000
0.866670012	0.133330002	0.250000000
0.600000024	0.200000003	0.250000000
0.800000012	0.200000003	0.250000000
0.200000003	0.200000003	0.250000000
0.400000006	0.200000003	0.250000000
0.000000000	0.200000003	0.250000000
0.666670024	0.333330005	0.250000000
0.866670012	0.333330005	0.250000000
0.266669989	0.333330005	0.250000000
0.466670007	0.333330005	0.250000000
0.066670001	0.333330005	0.250000000
0.000000000	0.400000006	0.250000000
0.600000024	0.400000006	0.250000000
0.800000012	0.400000006	0.250000000
0.200000003	0.400000006	0.250000000
0.400000006	0.400000006	0.250000000
0.066670001	0.533330023	0.250000000
0.666670024	0.533330023	0.250000000
0.866670012	0.533330023	0.250000000

0.266669989	0.533330023	0.250000000
0.466670007	0.533330023	0.250000000
0.400000006	0.600000024	0.250000000
0.000000000	0.600000024	0.250000000
0.600000024	0.600000024	0.250000000
0.800000012	0.600000024	0.250000000
0.200000003	0.600000024	0.250000000
0.066670001	0.733330011	0.250000000
0.866670012	0.733330011	0.250000000
0.466670007	0.733330011	0.250000000
0.666670024	0.733330011	0.250000000
0.266669989	0.733330011	0.250000000
0.400000006	0.800000012	0.250000000
0.600000024	0.800000012	0.250000000
0.000000000	0.800000012	0.250000000
0.800000012	0.800000012	0.250000000
0.200000003	0.800000012	0.250000000
0.266669989	0.933329999	0.250000000
0.066670001	0.933329999	0.250000000
0.466670007	0.933329999	0.250000000
0.666670024	0.933329999	0.250000000
0.866670012	0.933329999	0.250000000
0.600000024	0.000000000	0.250000000
0.800000012	0.000000000	0.250000000
0.200000003	0.000000000	0.250000000
0.400000006	0.000000000	0.250000000
0.796559989	0.790759981	0.381330013
0.592559993	0.791410029	0.381709993
0.727599978	0.856859982	0.381099999
0.795480013	0.992699981	0.381080002

0.929880023	0.062710002	0.381399989
0.731549978	0.063000001	0.381440014
0.133039996	0.068039998	0.382420003
0.533479989	0.068269998	0.382429987
0.199800000	0.202439994	0.382050008
0.600719988	0.202559993	0.382640004
0.401789993	0.207420006	0.383320004
0.536729991	0.274520010	0.383839995
0.335070014	0.274780005	0.382279992
0.607429981	0.406769991	0.384869993
0.328669995	0.466399997	0.380970001
0.739080012	0.468320012	0.382499993
0.395080000	0.600549996	0.381249994
0.806280017	0.601939976	0.381870002
0.931289971	0.863650024	0.381850004
0.530910015	0.864180028	0.381790012
0.998170018	0.998390019	0.381920010
0.598249972	0.998499990	0.381830007
0.201240003	0.003330000	0.382800013
0.400160015	0.003650000	0.382829994
0.334950000	0.072760001	0.383060008
0.996980011	0.197070003	0.381410003
0.798550010	0.197090000	0.381619990
0.931599975	0.264620006	0.381410003
0.130280003	0.265540004	0.381500006
0.733609974	0.265870005	0.382120013
0.998830020	0.398039997	0.381619990
0.196789995	0.399379998	0.381280005
0.802489996	0.399740010	0.381900012
0.934939981	0.466399997	0.381879985

0.131229997 0.466360003 0.381610006
0.329869986 0.667060018 0.381489992
0.937039971 0.668089986 0.382250011
0.397619992 0.800939977 0.382030010
0.002100000 0.801509976 0.382319987
0.199919999 0.801649988 0.382609993
0.134729996 0.869300008 0.382679999
0.333249986 0.869390011 0.382569999
0.001460000 0.599860013 0.382290006
0.197640002 0.599829972 0.381790012
0.133680001 0.668210030 0.382290006
0.569989979 0.535019994 0.469909996
0.736940026 0.660579979 0.381130010
0.396730006 0.404960006 0.381029993
0.523350000 0.661939979 0.382409990
0.470290005 0.521889985 0.486440003
0.669589996 0.552280009 0.488319993
0.763759971 0.878459990 0.517239988
0.564890027 0.531520009 0.388650000

Optimized POSCAR of NaCOOH adsorbed on NiN_3C_1

HCNONaNi

1.0

12.3386201859 0.0000000000 0.0000000000
-6.1693115158 10.6855577071 0.0000000000
0.0000000000 0.0000000000 26.0551109314

H C N O Na Ni

1 146 3 2 1 1

Direct

0.636600018 0.511219978 0.532720029
0.000000000 0.000000000 0.083329998

0.533330023	0.066670001	0.083329998
0.733330011	0.066670001	0.083329998
0.933329999	0.066670001	0.083329998
0.333330005	0.066670001	0.083329998
0.133330002	0.066670001	0.083329998
0.400000006	0.200000003	0.083329998
0.000000000	0.200000003	0.083329998
0.600000024	0.200000003	0.083329998
0.800000012	0.200000003	0.083329998
0.200000003	0.200000003	0.083329998
0.133330002	0.266669989	0.083329998
0.733330011	0.266669989	0.083329998
0.933329999	0.266669989	0.083329998
0.333330005	0.266669989	0.083329998
0.533330023	0.266669989	0.083329998
0.000000000	0.400000006	0.083329998
0.600000024	0.400000006	0.083329998
0.800000012	0.400000006	0.083329998
0.200000003	0.400000006	0.083329998
0.400000006	0.400000006	0.083329998
0.133330002	0.466670007	0.083329998
0.733330011	0.466670007	0.083329998
0.933329999	0.466670007	0.083329998
0.333330005	0.466670007	0.083329998
0.533330023	0.466670007	0.083329998
0.000000000	0.600000024	0.083329998
0.400000006	0.600000024	0.083329998
0.800000012	0.600000024	0.083329998
0.600000024	0.600000024	0.083329998
0.200000003	0.600000024	0.083329998

0.133330002	0.666670024	0.083329998
0.933329999	0.666670024	0.083329998
0.533330023	0.666670024	0.083329998
0.733330011	0.666670024	0.083329998
0.333330005	0.666670024	0.083329998
0.400000006	0.800000012	0.083329998
0.600000024	0.800000012	0.083329998
0.000000000	0.800000012	0.083329998
0.800000012	0.800000012	0.083329998
0.200000003	0.800000012	0.083329998
0.133330002	0.866670012	0.083329998
0.933329999	0.866670012	0.083329998
0.533330023	0.866670012	0.083329998
0.733330011	0.866670012	0.083329998
0.333330005	0.866670012	0.083329998
0.200000003	0.000000000	0.083329998
0.400000006	0.000000000	0.083329998
0.600000024	0.000000000	0.083329998
0.800000012	0.000000000	0.083329998
0.000000000	0.000000000	0.250000000
0.066670001	0.133330002	0.250000000
0.266669989	0.133330002	0.250000000
0.466670007	0.133330002	0.250000000
0.666670024	0.133330002	0.250000000
0.866670012	0.133330002	0.250000000
0.600000024	0.200000003	0.250000000
0.800000012	0.200000003	0.250000000
0.200000003	0.200000003	0.250000000
0.400000006	0.200000003	0.250000000
0.000000000	0.200000003	0.250000000

0.666670024	0.333330005	0.250000000
0.866670012	0.333330005	0.250000000
0.266669989	0.333330005	0.250000000
0.466670007	0.333330005	0.250000000
0.066670001	0.333330005	0.250000000
0.000000000	0.400000006	0.250000000
0.600000024	0.400000006	0.250000000
0.800000012	0.400000006	0.250000000
0.200000003	0.400000006	0.250000000
0.400000006	0.400000006	0.250000000
0.066670001	0.533330023	0.250000000
0.666670024	0.533330023	0.250000000
0.866670012	0.533330023	0.250000000
0.266669989	0.533330023	0.250000000
0.466670007	0.533330023	0.250000000
0.400000006	0.600000024	0.250000000
0.000000000	0.600000024	0.250000000
0.600000024	0.600000024	0.250000000
0.800000012	0.600000024	0.250000000
0.200000003	0.600000024	0.250000000
0.066670001	0.733330011	0.250000000
0.866670012	0.733330011	0.250000000
0.466670007	0.733330011	0.250000000
0.666670024	0.733330011	0.250000000
0.266669989	0.733330011	0.250000000
0.400000006	0.800000012	0.250000000
0.600000024	0.800000012	0.250000000
0.000000000	0.800000012	0.250000000
0.800000012	0.800000012	0.250000000
0.200000003	0.800000012	0.250000000

0.266669989	0.933329999	0.250000000
0.066670001	0.933329999	0.250000000
0.466670007	0.933329999	0.250000000
0.666670024	0.933329999	0.250000000
0.866670012	0.933329999	0.250000000
0.800000012	0.000000000	0.250000000
0.200000003	0.000000000	0.250000000
0.400000006	0.000000000	0.250000000
0.600000024	0.000000000	0.250000000
0.201550007	0.002890000	0.383300006
0.400579989	0.003270000	0.383679986
0.930180013	0.062470000	0.381960005
0.732140005	0.062909998	0.382330000
0.133300006	0.067649998	0.382869989
0.533800006	0.068080001	0.383350015
0.335379988	0.072650000	0.384030014
0.601000011	0.202779993	0.383390009
0.199900001	0.201940000	0.382459998
0.401980013	0.207039997	0.384660006
0.537240028	0.274349988	0.384860009
0.334639996	0.274190009	0.383139998
0.608120024	0.407000005	0.385749996
0.797540009	0.790579975	0.382169992
0.592809975	0.790579975	0.383089989
0.728089988	0.856660008	0.382510006
0.932330012	0.863730013	0.382160008
0.531189978	0.864080012	0.382669985
0.795840025	0.992420018	0.382090002
0.598659992	0.998189986	0.382779986
0.998589993	0.998279989	0.382340014

0.997200012	0.196830004	0.381669998
0.798900008	0.197060004	0.382169992
0.931879997	0.264620006	0.381669998
0.130349994	0.265269995	0.381599993
0.734179974	0.266030014	0.382569999
0.328759998	0.465869993	0.381480008
0.739499986	0.468450010	0.382589996
0.395339996	0.600210011	0.382349998
0.807309985	0.602330029	0.381599993
0.398240000	0.800710022	0.382710010
0.002680000	0.801400006	0.382070005
0.333790004	0.869279981	0.383120000
0.135560006	0.869300008	0.382679999
0.999180019	0.398030013	0.381570011
0.196980000	0.399170011	0.381220013
0.802850008	0.399710000	0.381909996
0.935509980	0.466690004	0.381550014
0.131630003	0.466529995	0.381460011
0.002250000	0.599839985	0.381729990
0.198029995	0.599680007	0.381770015
0.330469996	0.666880012	0.382050008
0.134279996	0.668190002	0.382099986
0.938059986	0.668410003	0.381619990
0.200430006	0.801549971	0.382699996
0.559390008	0.524030030	0.470479995
0.395680010	0.403659999	0.382230014
0.738709986	0.661589980	0.382140011
0.523880005	0.662180007	0.384299994
0.653219998	0.514630020	0.495469987
0.476819992	0.525349975	0.496850014

0.756609976 0.855459988 0.519699991

0.565439999 0.530960023 0.392589986

Optimized POSCAR of NaCO adsorbed on NiN_3C_1

CNONaNi

1.0

12.3386201859 0.0000000000 0.0000000000

-6.1693115158 10.6855577071 0.0000000000

0.0000000000 0.0000000000 26.0551109314

C N O Na Ni

146 3 1 1 1

Direct

0.000000000 0.000000000 0.083329998

0.533330023 0.066670001 0.083329998

0.733330011 0.066670001 0.083329998

0.933329999 0.066670001 0.083329998

0.333330005 0.066670001 0.083329998

0.133330002 0.066670001 0.083329998

0.400000006 0.200000003 0.083329998

0.000000000 0.200000003 0.083329998

0.600000024 0.200000003 0.083329998

0.800000012 0.200000003 0.083329998

0.200000003 0.200000003 0.083329998

0.133330002 0.266669989 0.083329998

0.733330011 0.266669989 0.083329998

0.933329999 0.266669989 0.083329998

0.333330005 0.266669989 0.083329998

0.533330023 0.266669989 0.083329998

0.000000000 0.400000006 0.083329998

0.600000024 0.400000006 0.083329998

0.800000012 0.400000006 0.083329998

0.200000003	0.400000006	0.083329998
0.400000006	0.400000006	0.083329998
0.133330002	0.466670007	0.083329998
0.733330011	0.466670007	0.083329998
0.933329999	0.466670007	0.083329998
0.333330005	0.466670007	0.083329998
0.533330023	0.466670007	0.083329998
0.000000000	0.600000024	0.083329998
0.400000006	0.600000024	0.083329998
0.800000012	0.600000024	0.083329998
0.600000024	0.600000024	0.083329998
0.200000003	0.600000024	0.083329998
0.133330002	0.666670024	0.083329998
0.933329999	0.666670024	0.083329998
0.533330023	0.666670024	0.083329998
0.733330011	0.666670024	0.083329998
0.333330005	0.666670024	0.083329998
0.400000006	0.800000012	0.083329998
0.600000024	0.800000012	0.083329998
0.000000000	0.800000012	0.083329998
0.800000012	0.800000012	0.083329998
0.200000003	0.800000012	0.083329998
0.133330002	0.866670012	0.083329998
0.933329999	0.866670012	0.083329998
0.533330023	0.866670012	0.083329998
0.733330011	0.866670012	0.083329998
0.333330005	0.866670012	0.083329998
0.200000003	0.000000000	0.083329998
0.400000006	0.000000000	0.083329998
0.600000024	0.000000000	0.083329998

0.800000012	0.000000000	0.083329998
0.000000000	0.000000000	0.250000000
0.200000003	0.000000000	0.250000000
0.066670001	0.133330002	0.250000000
0.266669989	0.133330002	0.250000000
0.466670007	0.133330002	0.250000000
0.666670024	0.133330002	0.250000000
0.866670012	0.133330002	0.250000000
0.600000024	0.200000003	0.250000000
0.800000012	0.200000003	0.250000000
0.200000003	0.200000003	0.250000000
0.400000006	0.200000003	0.250000000
0.000000000	0.200000003	0.250000000
0.666670024	0.333330005	0.250000000
0.866670012	0.333330005	0.250000000
0.266669989	0.333330005	0.250000000
0.466670007	0.333330005	0.250000000
0.066670001	0.333330005	0.250000000
0.000000000	0.400000006	0.250000000
0.600000024	0.400000006	0.250000000
0.800000012	0.400000006	0.250000000
0.200000003	0.400000006	0.250000000
0.400000006	0.400000006	0.250000000
0.066670001	0.533330023	0.250000000
0.666670024	0.533330023	0.250000000
0.866670012	0.533330023	0.250000000
0.266669989	0.533330023	0.250000000
0.466670007	0.533330023	0.250000000
0.400000006	0.600000024	0.250000000
0.000000000	0.600000024	0.250000000

0.600000024	0.600000024	0.250000000
0.800000012	0.600000024	0.250000000
0.200000003	0.600000024	0.250000000
0.066670001	0.733330011	0.250000000
0.866670012	0.733330011	0.250000000
0.466670007	0.733330011	0.250000000
0.666670024	0.733330011	0.250000000
0.266669989	0.733330011	0.250000000
0.400000006	0.800000012	0.250000000
0.600000024	0.800000012	0.250000000
0.000000000	0.800000012	0.250000000
0.800000012	0.800000012	0.250000000
0.200000003	0.800000012	0.250000000
0.266669989	0.933329999	0.250000000
0.066670001	0.933329999	0.250000000
0.466670007	0.933329999	0.250000000
0.666670024	0.933329999	0.250000000
0.866670012	0.933329999	0.250000000
0.800000012	0.000000000	0.250000000
0.400000006	0.000000000	0.250000000
0.600000024	0.000000000	0.250000000
0.201350003	0.003070000	0.382889986
0.400350004	0.003340000	0.382910013
0.930090010	0.062490001	0.381900012
0.732029974	0.062870003	0.382010013
0.133220002	0.067790002	0.382169992
0.533729970	0.068089999	0.382230014
0.335269988	0.072910003	0.382880002
0.600960016	0.202710003	0.382180005
0.200310007	0.202419996	0.381870002

0.402040005	0.207369998	0.382319987
0.537419975	0.274780005	0.382110000
0.335319996	0.274809986	0.381509990
0.607800007	0.407059997	0.381929994
0.796440005	0.789940000	0.380989999
0.592419982	0.790489972	0.380769998
0.727769971	0.856469989	0.380699992
0.931729972	0.863439977	0.381700009
0.530910015	0.864139974	0.381579995
0.795669973	0.992410004	0.381440014
0.598429978	0.998210013	0.381839991
0.998260021	0.998099983	0.381799996
0.997259974	0.196850002	0.382580012
0.798850000	0.196830004	0.382759988
0.932039976	0.264640003	0.383089989
0.130449995	0.265390009	0.382299989
0.734139979	0.265830010	0.382649988
0.328740001	0.466300011	0.381410003
0.739530027	0.468080014	0.381989986
0.394950002	0.600489974	0.381460011
0.807030022	0.601849973	0.381940007
0.398009986	0.800979972	0.382580012
0.002240000	0.801460028	0.382770002
0.200189993	0.801699996	0.383920014
0.333579987	0.869589984	0.383399993
0.135220006	0.869390011	0.383430004
0.999189973	0.397929996	0.383690000
0.197129995	0.399370015	0.382519990
0.802980006	0.399659991	0.382820010
0.935590029	0.466650009	0.383729994

0.131630003 0.466650009 0.383540004
0.197789997 0.599829972 0.383679986
0.001990000 0.599749982 0.383899987
0.330190003 0.667119980 0.382600009
0.134110004 0.668420017 0.384110004
0.937420011 0.668160021 0.382990003
0.561420023 0.527440012 0.475259990
0.396780014 0.405030012 0.380519986
0.737380028 0.660600007 0.381320000
0.523720026 0.662220001 0.380789995
0.647379994 0.533949971 0.496780008
0.762109995 0.862389982 0.518400013
0.565140009 0.531610012 0.383870006

Optimized POSCAR of CO adsorbed on NiN_3C_1

CNONi

1.0

12.3386201859 0.0000000000 0.0000000000
-6.1693115158 10.6855577071 0.0000000000
0.0000000000 0.0000000000 26.0551109314

C N O Ni

146 3 1 1

Direct

0.000000000 0.000000000 0.083329998
0.533330023 0.066670001 0.083329998
0.733330011 0.066670001 0.083329998
0.933329999 0.066670001 0.083329998
0.333330005 0.066670001 0.083329998
0.133330002 0.066670001 0.083329998
0.400000006 0.200000003 0.083329998
0.000000000 0.200000003 0.083329998

0.600000024	0.200000003	0.083329998
0.800000012	0.200000003	0.083329998
0.200000003	0.200000003	0.083329998
0.133330002	0.266669989	0.083329998
0.733330011	0.266669989	0.083329998
0.933329999	0.266669989	0.083329998
0.333330005	0.266669989	0.083329998
0.533330023	0.266669989	0.083329998
0.000000000	0.400000006	0.083329998
0.600000024	0.400000006	0.083329998
0.800000012	0.400000006	0.083329998
0.200000003	0.400000006	0.083329998
0.400000006	0.400000006	0.083329998
0.133330002	0.466670007	0.083329998
0.733330011	0.466670007	0.083329998
0.933329999	0.466670007	0.083329998
0.333330005	0.466670007	0.083329998
0.533330023	0.466670007	0.083329998
0.000000000	0.600000024	0.083329998
0.400000006	0.600000024	0.083329998
0.800000012	0.600000024	0.083329998
0.600000024	0.600000024	0.083329998
0.200000003	0.600000024	0.083329998
0.133330002	0.666670024	0.083329998
0.933329999	0.666670024	0.083329998
0.533330023	0.666670024	0.083329998
0.733330011	0.666670024	0.083329998
0.333330005	0.666670024	0.083329998
0.400000006	0.800000012	0.083329998
0.600000024	0.800000012	0.083329998

0.000000000	0.800000012	0.083329998
0.800000012	0.800000012	0.083329998
0.200000003	0.800000012	0.083329998
0.133330002	0.866670012	0.083329998
0.933329999	0.866670012	0.083329998
0.533330023	0.866670012	0.083329998
0.733330011	0.866670012	0.083329998
0.333330005	0.866670012	0.083329998
0.200000003	0.000000000	0.083329998
0.400000006	0.000000000	0.083329998
0.600000024	0.000000000	0.083329998
0.800000012	0.000000000	0.083329998
0.000000000	0.000000000	0.250000000
0.200000003	0.000000000	0.250000000
0.066670001	0.133330002	0.250000000
0.266669989	0.133330002	0.250000000
0.466670007	0.133330002	0.250000000
0.666670024	0.133330002	0.250000000
0.866670012	0.133330002	0.250000000
0.600000024	0.200000003	0.250000000
0.800000012	0.200000003	0.250000000
0.200000003	0.200000003	0.250000000
0.400000006	0.200000003	0.250000000
0.000000000	0.200000003	0.250000000
0.666670024	0.333330005	0.250000000
0.866670012	0.333330005	0.250000000
0.266669989	0.333330005	0.250000000
0.466670007	0.333330005	0.250000000
0.066670001	0.333330005	0.250000000
0.000000000	0.400000006	0.250000000

0.600000024	0.400000006	0.250000000
0.800000012	0.400000006	0.250000000
0.200000003	0.400000006	0.250000000
0.400000006	0.400000006	0.250000000
0.066670001	0.533330023	0.250000000
0.666670024	0.533330023	0.250000000
0.866670012	0.533330023	0.250000000
0.266669989	0.533330023	0.250000000
0.466670007	0.533330023	0.250000000
0.400000006	0.600000024	0.250000000
0.000000000	0.600000024	0.250000000
0.600000024	0.600000024	0.250000000
0.800000012	0.600000024	0.250000000
0.200000003	0.600000024	0.250000000
0.066670001	0.733330011	0.250000000
0.866670012	0.733330011	0.250000000
0.466670007	0.733330011	0.250000000
0.666670024	0.733330011	0.250000000
0.266669989	0.733330011	0.250000000
0.400000006	0.800000012	0.250000000
0.600000024	0.800000012	0.250000000
0.000000000	0.800000012	0.250000000
0.800000012	0.800000012	0.250000000
0.200000003	0.800000012	0.250000000
0.266669989	0.933329999	0.250000000
0.066670001	0.933329999	0.250000000
0.466670007	0.933329999	0.250000000
0.666670024	0.933329999	0.250000000
0.866670012	0.933329999	0.250000000
0.800000012	0.000000000	0.250000000

0.400000006	0.000000000	0.250000000
0.600000024	0.000000000	0.250000000
0.201399997	0.003570000	0.382640004
0.400440007	0.003810000	0.382669985
0.929759979	0.062369999	0.382490009
0.731459975	0.062689997	0.382369995
0.133029997	0.067979999	0.382380009
0.533500016	0.068379998	0.382360011
0.335299999	0.073229998	0.383069992
0.600839972	0.202790007	0.382510006
0.199560001	0.202260002	0.382110000
0.402150005	0.207650006	0.383509994
0.537079990	0.274549991	0.383579999
0.334390014	0.274599999	0.382640004
0.608319998	0.407070011	0.384409994
0.796809971	0.790489972	0.382900000
0.592220008	0.791100025	0.382340014
0.727569997	0.856509984	0.383040011
0.931909978	0.863849998	0.382360011
0.530579984	0.864390016	0.381790012
0.795440018	0.992200017	0.382730007
0.598309994	0.998459995	0.382090002
0.998199999	0.998260021	0.382360011
0.996710002	0.196710005	0.382220000
0.798539996	0.196899995	0.382279992
0.931519985	0.264349997	0.382200003
0.130030006	0.265410006	0.381909996
0.733870029	0.265929997	0.382290006
0.328339994	0.465860009	0.381229997
0.739359975	0.468309999	0.382290006

0.395300001	0.601109982	0.381209999
0.807089984	0.602460027	0.382120013
0.397870004	0.801110029	0.381850004
0.002440000	0.801739991	0.382340014
0.200420007	0.802200019	0.382490009
0.333400011	0.869830012	0.382400006
0.135350004	0.869899988	0.382519990
0.999029994	0.398240000	0.382039994
0.196400002	0.399120003	0.381469995
0.802730024	0.399569988	0.381940007
0.935209990	0.466600001	0.381960005
0.131300002	0.466580003	0.381729990
0.197740003	0.599990010	0.381740004
0.001960000	0.600120008	0.382070005
0.329990000	0.667490005	0.381399989
0.133870006	0.668240011	0.382239997
0.937940001	0.668760002	0.382079989
0.577329993	0.533370018	0.468989998
0.395110011	0.404150009	0.382169992
0.738430023	0.661289990	0.383139998
0.522930026	0.662880003	0.382470012
0.642920017	0.527050018	0.499410003
0.564979970	0.531470001	0.391799986

References Cited in the Supporting Information

(1) Zhang, Z.; Gee, W.; Sautet, P.; Alexandrova, A. N. H and CO Co-Induced Roughening of Cu Surface in CO $_2$ Electroreduction Conditions. *J. Am. Chem. Soc.* **2024**, *146* (23), 16119–16127. https://doi.org/10.1021/jacs.4c03515.

(2) Choi, J.; Chiu, S.; Banerjee, A.; Sacci, R. L.; Veith, G. M.; Stieber, C.; Hahn, C.; Alexandrova, A. N.; Morales-Guio, C. G. Corrosion and Enhanced Hydrogen Evolution in Electrochemical Reduction of Ammonium Carbamate on Transition Metal Surfaces. *J. Phys. Chem. Lett.* **2024**, 8007–8017. https://doi.org/10.1021/acs.jpclett.4c01638.

(3) Zhang, Z.; Hermans, I.; Alexandrova, A. N. Off-Stoichiometric Restructuring and Sliding Dynamics of Hexagonal Boron Nitride Edges in Conditions of Oxidative Dehydrogenation of Propane. *J. Am. Chem. Soc.* **2023**, *145* (31), 17265–17273. https://doi.org/10.1021/jacs.3c04613.

(4) Steinmann, S. N.; Michel, C.; Schwiedernoch, R.; Sautet, P. Impacts of Electrode Potentials and Solvents on the Electroreduction of CO $_2$: A Comparison of Theoretical Approaches. *Phys. Chem. Chem. Phys.* **2015**, *17* (21), 13949–13963. https://doi.org/10.1039/C5CP00946D.

(5) Kowalski, R. M.; Banerjee, A.; Yue, C.; Gracia, S. G.; Cheng, D.; Morales-Guio, C. G.; Sautet, P. Electroreduction of Captured CO $_2$ on Silver Catalysts: Influence of the Capture Agent and Proton Source. *J. Am. Chem. Soc.* **2024**, *146* (30), 20728–20741. https://doi.org/10.1021/jacs.4c03915.

(6) Mathew, K.; Kolluru, V. S. C.; Mula, S.; Steinmann, S. N.; Hennig, R. G. Implicit Self-Consistent Electrolyte Model in Plane-Wave Density-Functional Theory. *The Journal of Chemical Physics* **2019**, *151* (23), 234101. https://doi.org/10.1063/1.5132354.

(7) Vilela Oliveira, D.; Laun, J.; Peintinger, M. F.; Bredow, T. BSSE-Correction Scheme for Consistent Gaussian Basis Sets of Double- and Triple-Zeta Valence with Polarization Quality for Solid-State Calculations. *Journal of Computational Chemistry* **2019**, *40* (27), 2364–2376. https://doi.org/10.1002/jcc.26013.

(8) Erba, A.; Desmarais, J. K.; Casassa, S.; Civalleri, B.; Donà, L.; Bush, I. J.; Searle, B.; Maschio, L.; Edith-Daga, L.; Cossard, A.; Ribaldone, C.; Ascrizzi, E.; Marana, N. L.; Flament, J.-P.; Kirtman, B. CRYSTAL23: A Program for Computational Solid State Physics and Chemistry. *J. Chem. Theory Comput.* **2023**, *19* (20), 6891–6932. https://doi.org/10.1021/acs.jctc.2c00958.

(9) Pisani, C.; Schütz, M.; Casassa, S.; Usvyat, D.; Maschio, L.; Lorenz, M.; Erba, A. CRYSCOR: A Program for the Post-Hartree–Fock Treatment of Periodic Systems. *Phys. Chem. Chem. Phys.* **2012**, *14* (21), 7615–7628. https://doi.org/10.1039/C2CP23927B.

(10) Weigend, F.; Köhn, A.; Hättig, C. Efficient Use of the Correlation Consistent Basis Sets in Resolution of the Identity MP2 Calculations. *The Journal of Chemical Physics* **2002**, *116* (8), 3175–3183. https://doi.org/10.1063/1.1445115.

(11) Knowles, P. J.; Handy, N. C. A Determinant Based Full Configuration Interaction Program. *Computer Physics Communications* **1989**, *54* (1), 75–83. https://doi.org/10.1016/0010-4655(89)90033-7.

(12) Sun, Q.; Zhang, X.; Banerjee, S.; Bao, P.; Barbry, M.; Blunt, N. S.; Bogdanov, N. A.; Booth, G. H.; Chen, J.; Cui, Z.-H.; Eriksen, J. J.; Gao, Y.; Guo, S.; Hermann, J.; Hermes, M. R.; Koh, K.; Koval, P.; Lehtola, S.; Li, Z.; Liu, J.; Mardirossian, N.; McClain, J. D.; Motta, M.; Mussard, B.; Pham, H. Q.; Pulkin, A.; Purwanto, W.; Robinson, P. J.; Ronca, E.;

Sayfutyarova, E. R.; Scheurer, M.; Schurkus, H. F.; Smith, J. E. T.; Sun, C.; Sun, S.-N.; Upadhyay, S.; Wagner, L. K.; Wang, X.; White, A.; Whitfield, J. D.; Williamson, M. J.; Wouters, S.; Yang, J.; Yu, J. M.; Zhu, T.; Berkelbach, T. C.; Sharma, S.; Sokolov, A. Yu.; Chan, G. K.-L. Recent Developments in the PySCF Program Package. *The Journal of Chemical Physics* **2020**, *153* (2), 024109. https://doi.org/10.1063/5.0006074.

(13) Celani, P.; Werner, H.-J. Multireference Perturbation Theory for Large Restricted and Selected Active Space Reference Wave Functions. *The Journal of Chemical Physics* **2000**, *112* (13), 5546–5557. https://doi.org/10.1063/1.481132.

(14) Werner, H.-J.; Knowles, P. J.; Manby, F. R.; Black, J. A.; Doll, K.; Heßelmann, A.; Kats, D.; Köhn, A.; Korona, T.; Kreplin, D. A.; Ma, Q.; Miller, T. F., III; Mitrushchenkov, A.; Peterson, K. A.; Polyak, I.; Rauhut, G.; Sibaev, M. The Molpro Quantum Chemistry Package. *The Journal of Chemical Physics* **2020**, *152* (14), 144107. https://doi.org/10.1063/5.0005081.

(15) Radoń, M. Spin-State Energetics of Heme-Related Models from DFT and Coupled Cluster Calculations. *J. Chem. Theory Comput.* **2014**, *10* (6), 2306–2321. https://doi.org/10.1021/ct500103h.

(16) Lee, T. J.; Taylor, P. R. A Diagnostic for Determining the Quality of Single-Reference Electron Correlation Methods. *International Journal of Quantum Chemistry* **1989**, *36* (S23), 199–207. https://doi.org/10.1002/qua.560360824.

(17) Lee, T. J.; Rice, J. E.; Scuseria, G. E.; Schaefer, H. F. Theoretical Investigations of Molecules Composed Only of Fluorine, Oxygen and Nitrogen: Determination of the Equilibrium Structures of FOOF, (NO)2 and FNNF and the Transition State Structure for FNNF Cis-Trans Isomerization. *Theoret. Chim. Acta* **1989**, *75* (2), 81–98. https://doi.org/10.1007/BF00527711.

(18) Ali, Md. E.; Sanyal, B.; Oppeneer, P. M. Electronic Structure, Spin-States, and Spin-Crossover Reaction of Heme-Related Fe-Porphyrins: A Theoretical Perspective. *J. Phys. Chem. B* **2012**, *116* (20), 5849–5859. https://doi.org/10.1021/jp3021563.

(19) Kozuch, S.; Shaik, S. A Combined Kinetic−Quantum Mechanical Model for Assessment of Catalytic Cycles: Application to Cross-Coupling and Heck Reactions. *J. Am. Chem. Soc.* **2006**, *128* (10), 3355–3365. https://doi.org/10.1021/ja0559146.

(20) Kozuch, S.; Shaik, S. How to Conceptualize Catalytic Cycles? The Energetic Span Model. *Acc. Chem. Res.* **2011**, *44* (2), 101–110. https://doi.org/10.1021/ar1000956.

(21) Joly, Y. X-Ray Absorption near-Edge Structure Calculations beyond the Muffin-Tin Approximation. *Phys. Rev. B* **2001**, *63* (12), 125120. https://doi.org/10.1103/PhysRevB.63.125120.

(22) Joly, Y.; Bunău, O.; Lorenzo, J. E.; Galéra, R. M.; Grenier, S.; Thompson, B. Self-Consistency, Spin-Orbit and Other Advances in the FDMNES Code to Simulate XANES and RXD Experiments. *J. Phys.: Conf. Ser.* **2009**, *190*, 012007. https://doi.org/10.1088/1742-6596/190/1/012007.

(23) Banerjee, A.; Yue, C.; Choi, J.; Morales-Guio, C. G. Rotating Cylinder Electrode in Reactive CO2 Capture: Identifying Active C Species via Transport, VLE Models and Kinetics. *AIChE Journal 70*, e18560. https://doi.org/10.1002/aic.18560.

Acknowledgements

Work by R.D.R., H.J., A.P. and C.H. was performed under the auspices of the U.S. Department of Energy by Lawrence Livermore National Laboratory (LLNL) under Contract DE-AC52-07NA27344. LLNL release number: LLNL-JRNL-2004639.